Abstract

Measurement and analysis of the angular distribution of solar radiation is a key problem in Solar Resource Assessment. Existing high resolution, circumsolar and sky-mapping instruments are too expensive and labor intensive for long term or remote deployment. This thesis presents a novel instrument called the Sunshape Profiling Irradiometer (SPI) and an inverse model for the determination of the solar radiance profile and the circumsolar ratio (CSR) for a location. A prototype has been built from a stepping-motor-based Rotating Shadowband Irradiometer with mechanical modifications that are novel yet simple. An optical slit receiver is used to best resolve brightness change during progressive occultation of the circumsolar region by the shadow band. For the prototype a Licor's receiver is narrowed to a slit, cut on the axis line. A trough signal trajectory is obtained when the band crosses the sun and the amount of rounding of the corners of the trough is related to the CSR. A family of normalized simulated signals corresponding to different CSRs generated by integrating Buie's equations is used to find the best match of the normalized measured profile from the SPI to get a good estimate of the CSR. Results of the obtained CSRs are validated with the broadband CSRs given by the Sun and Aureole Measurement System (SAM). Buie's model is observed to work well only for clear sky conditions and the assumed angular extent of the sun aureole is small for regions that have large aerosol concentration, relative humidity and hazy skies like Abu Dhabi. Hence, a more complete and rigorous model based on direct inversion of the SPI signal is proposed to obtain the actual brightness profiles for any location. The instrument can be used for climate research (ARM.gov) as well as improved resource characterization for applications that need an accurate circumsolar and/or sky model such as concentrating solar power (CSP, CPV) and day lighting.

This research was supported by the Government of Abu Dhabi to help fulfill the vision of the late President Sheikh Zayed Bin Sultan Al Nayhan for sustainable development and empowerment of the UAE and humankind.

Acknowledgments

This thesis would not have been possible without the guidance and help of several individuals who have contributed and extended their valuable guidance, encouragement and support throughout the preparation time of this study.

First and foremost, I offer my sincere gratitude to my supervisor, Dr. Peter Armstrong, who has guided and walked me through this journey with immense knowledge and inspiration. Working with Dr. Armstrong has been a very good learning experience which has helped me at all times of my research and I am sure it will in future as well. Besides my advisor, I would like to thank the rest of my Research Supervisory Committee: Dr. Afshin Afshari and Dr. Matteo Chiesa for their encouragement. I sincerely thank Stefan Wilbert and Dennis Villanucci for the helping me with the SAM and providing their insightful comments and suggestions. I would like to acknowledge the support and assistance given by my lab mates Marwan Mokhtar, Karim Raafat Mahmoud, Muhammad Tauha Ali, Ahmed Zayan and Ali Al Masabai. I express my gratitude to Dr. Richard Meyers and Mr. Kaushal Chhatbar for encouraging the need for such instruments. I appreciate the encouragement and support provided by my dear friends Shailesh Chekurthi, Ruth Gabell, Nikhil Naik, Shwetha Namani, Rohit, Titly Farhana Faisal and Lakshmi Natarajan.

Most importantly, I would like to thank my parents, brother and my entire family for their unwavering support throughout my academic and educational pursuits. Without it, I could not have achieved what I have today. Last but not the least; I thank the omnipresent God, for answering my prayers and giving me the strength to deal with all the challenges.

Ragini Kalapatapu,

Masdar City, May 15 2012

Contents

List of Tables

List of Figures

CHAPTER 1

Introduction

1.1 Problem Statement

Harnessing the sun’s radiant energy incident on our planet stands forth as a grand challenge for mankind in this century. The two primary forms of solar power generation solar are Photovoltaics (PV) and Concentrating Solar Power (CSP). High Concentration of sunlight is proving to be less expensive and more efficient method for generating solar power in both CSP and CPV industries. Large scale concentrating systems require a substantial investment and hence accurate assessment of the quality and reliability of the solar resource is required before undertaking such projects. The life cycle value of a concentrating system depends upon the following three elements (Stoffel, et al., 2010):

- Selection of the site
- Prediction of the annual output of the plant
- Strategy of operation and temporal performance

Direct solar radiation is the most important factor for site selection and prediction of annual concentrating power plant output. To assess the performance and financial viability of CSP/CPV systems, high quality measurement of the Direct Normal Irradiance (DNI) is required. However, this is not straight forward. Maximum theoretical concentration (C_{max}) is a function of acceptance half angle (θ_c) shown in equation 1.1:

$$C_{max} = \begin{cases} \dfrac{1}{sin\theta_c}\ for\ line\ focus\ concentrators\ (parabolic\ troughs) \\ \dfrac{1}{sin^2\theta_c}\ for\ point\ focus\ concentrators\ (central\ towers, parabolic\ dishes) \end{cases} \quad (1.1)$$

Thus, a definition of DNI must reference the instruments' field of view and ideally characterize the angular distribution within its field of view. For over 100 years, the DNI measuring instruments have used a rather large field of view that is almost one hundred times larger than the solid angle of the solar disk at the mean solar distance.

The forward scattering of atmospheric particles, aerosols, water vapor, molecules of N_2, O_3 etc. results in the formation of a region around the solar disk called the circumsolar region or the sun aureole. So, the DNI measuring instruments capture a large portion of incoming radiation not only from the solar disk but also from the circumsolar region. Hence, the actual DNI that is incident on the collector is mostly overestimated based on the radiation coming from the circumsolar region.

The angular brightness distribution of the solar disk and the aureole around it is known as sunshape in solar energy applications (Neumann A. , Witzke, Scott, & Gregor, 2002). A complete and precise description of the varying sunshape profiles due to the angular radiation distribution of incoming solar radiation will prove to be useful in creating accurate optical models for solar concentrating systems that can take into account the specific site conditions for determining the optimum acceptance angle for the incoming direct radiation. The true power output and efficiency of a solar concentrating power plant can be more accurately predicted with precise information about the angular distribution of the solar radiation.

The impact of circumsolar radiation is expected to be high in regions having high concentrations of aerosols, dust and humidity, as in the case of UAE. This thesis describes the design and development of a novel instrument that is inexpensive but has reliable instrumentation, for the measurement of sunshapes along with a suitable model to obtain good predictions of spectral and broadband circumsolar irradiances. From the measured sunshape profiles with the instrument, the effect of the circumsolar radiation on a CSP plant in UAE has been studied and analyzed as part of this thesis.

1.2 Research Objectives

The main objective of this research is to develop a low cost field instrument for measuring the sunshapes from the trough like trajectories generated by the device.

For this purpose, the tasks described in this thesis follow logically as:

- A numerical analysis of flux maps on the receiver of the Sunshape Profiling Irradiometer with six different design cases- point receiver with band, half globe and full globe shading devices and circular receiver with band, half globe and full globe shading devices.
- Design and development of the Sunshape Profiling Irradiometer (SPI) for the measurement of sunshapes.
- Inverse model using Buie’s equations as basic functions to obtain the circumsolar ratios from the measured sunshape profiles.
- Validation of the estimated Circumsolar Ratio (CSR) with the inverse Buie model from measured trajectories with the Sunshape Profiling Irradiometer (SPI) with the predicted circumsolar ratios from the Sun and Aureole Measurement system (SAM).

- Analysis of the impact of the circumsolar irradiance on a CSP plant in UAE from the measured sunshape profiles.
- Formulation of a direct inversion model to obtain the actual brightness profiles for the whole sky region, independent of the location of the site, climatic conditions and time of the day.

CHAPTER 2

Literature Review

The literature is rich in many aspects related to the measurement of DNI, sunshapes, estimation and modeling of the circumsolar irradiance, small angle scattering of atmospheric particles, optical analysis to determine the flux at the receiver as a function of sunshape and the geometry of the concentrating system. A brief review of the essential contributions in each of these areas is discussed in this chapter.

2.1 Circumsolar Radiation

Circumsolar radiation refers to the radiation that appears to originate from the region around the sun. It is often described as the sun aureole. The brightness distribution of the solar and the circumsolar regions is known as sunshape (Neumann & Witzke, 1999). The intensity distribution of the radiation from this region is controlled by the optical depth of the atmosphere due to the presence of aerosol particles, thin cirrus clouds and other physic- chemical properties of the particles such as ice crystals etc. (Thomalla, Kopke, Muller, & Quenzel, 1982). Most of the radiation in this region is scattered forwards, which results in a strong decrease in radiation with increasing distance from the sun. The two most predominant scattering processes for radiation passing through the atmosphere are Rayleigh and Mie Scattering. Rayleigh scattering occurs when radiation interacts with particles smaller than the wavelength of the radiation, whereas Mie scattering occurs when the incoming radiation interacts with particles that are relatively larger than the wavelength of the propagating light (Buie, 2004). Hence, Mie scattering is essentially small angle forward scattering that transforms some of the incident solar radiation from within the confines of the solar disc, resulting in the formation of the solar aureole. The combination of both scattering processes creates a specific spatial and spectral energy distribution which depends on atmospheric conditions and solar zenith angle. The radiation coming from the solar aureole and its angular distribution is important for the following reasons:

- Overestimation of CSP yield occurs when the acceptance angle of solar concentrating system is lower than the acceptance angle of the DNI measuring instruments.
- The aureole profiles can be used to further investigate the forward scattering phenomenon and concentration of distribution of aerosols. The shape of the radiance curves and the absolute values of the radiances in different circumsolar angular bands vary with different aerosol types. Hence, the density and to some extent, even the dimensions of the atmospheric particles can be predicted from the radiance profiles.
- The area surrounding a receiver aperture may be irradiated by the circumsolar radiation (spillage) of sufficient intensity to damage the materials (Thomalla, Kopke, Muller, & Quenzel, 1982).
- The angular distribution of the circumsolar radiation is needed to optimize the receiver aperture of a concentrating solar system. Extension of the receiver aperture results on one hand in an increase in the incoming radiation onto the receiver, but on the other hand causes an increase in the receiver’s thermal losses (Thomalla, Kopke, Muller, & Quenzel, 1982).

Calculations and measurements of sunshapes have been carried out by several researchers in the past (Thomalla, Kopke, Muller, & Quenzel, 1982) based on the scattering function, wavelength dependence of radiation, absorption of radiation by atmospheric aerosols and gases with a combination of several parameters changing simultaneously. Nearly 180,000 sunshape profiles were collected at 11 different sites in the US between 1976 and 1981 (Grether, Evans, Hunt, & Wahlig, 1979) describing the dependence of the circumsolar radiation with geographic location, climate, season, time of the day, and observing wavelengths (at eight different wavelength bands and one open/clear), as later published in the Lawrence Berkeley Laboratories (LBL) reduced database (Noring, Grether, & Hunt, 1991). The sunshapes within the Reduced Data Base (RDB) were averaged and filtered into groups of solar profiles with a similar parameter called the Circumsolar Ratio (CSR).

2.2 Direct Normal Irradiance (DNI) Measurements

The World Meteorological Organization (WMO) defines the DNI as the amount of radiation coming from the sun and a narrow annulus of the sky as measured by the pyrheliometer designed with a full angle of about 5^o (Stoffel, et al., 2010). This means that pyrheliometers measure some circumsolar radiation together with the direct radiation from the solar disk whose diameter subtends a full angle of only 0.5^o field of view. Rotating Shadowband Irradiometer (RSI) is also used to measure the DNI with 8.1^o field of view (Keidron, Schlemmer, & Klassen, 2006). The error due to the circumsolar radiation among different DNI measuring instruments at different acceptance angles while measuring the global radiation as a sum of direct and diffuse radiation was demonstrated by (Major, 1992). Figure 2.1 shows the CM1 pyrheliometer installed on the radiometer platform at Masdar with a field of view of 5 ±0.2 °. The aperture angles of the pyrheliometer and absolute cavity radiometers for measuring DNI are given in Table 2.1.

Figure 2.1: CM1 Pyrheliometer at Masdar

Table 2.1: Aperture angles of the DNI measuring instruments

No	Type or Make of Radiometer	Acceptance Angle
1.	Eppley-Angstrom Pyrheliometer (Hulstrom, 1989)	5^o
2.	Eppley Normal Incidence Pyrheliometer (Hulstrom, 1989)	5.7^o
3.	Spectropyrheliometer (Zerlaut & Maybee, 1982)	6^o
4.	Kipp and Zonen/ Linke-Feussner Pyrheliometer (Actinometer) (Hulstrom, 1989)	9.6^o
5.	Kipp and Zonen CHP 1 Pyrheliometer (Kipp & Zonen, 2008)	5^o
6.	Absolute Cavity Radiometer (ASTM Standards, 2010)	5^o

It was concluded that the pyrheliometer measurement includes a large portion of the circumsolar radiation and this difference which should be taken into account for meteorological and solar energy investigations. Hence, the overestimation of the amount of direct sunlight collected by a concentrating system of given optical characteristics should be adjusted (e.g. by convolution as in Bendt et al 1979) by obtaining a detailed angular distribution of the solar radiation.

2.3 Circumsolar Brightness Models and Circumsolar Ratio (CSR)

The circumsolar ratio is defined as the radiant flux contained within the circumsolar region of (Φ_{cs}) over the incident radiant flux from solar disk and circumsolar region Φ_i (Buie, 2004):

$$CSR = \frac{\emptyset_{cs}}{\emptyset_{disk} + \emptyset_{cs}} \qquad (2.1)$$

An algorithm was developed by (Buie, 2004)for measuring the Circumsolar Ratio which is invariant to changes in location based on the slope and intercept of the sunshape curves. The CSR is usually obtained by integrating, under the assumption of circular symmetry, the radial distribution of the solar brightness. The integrals of interest are given by equations 2.2 and 2.3:

$$\phi_{disk} = 2\pi \int_{Sun} B(r)rdr \qquad (2.2)$$

$$\phi_{CS} = 2\pi \int_{Circumsolar} B(r)rdr \qquad (2.3)$$

where $B(r)$ is the radial distribution of the solar and circumsolar brightness at an angular distance r from the center of the solar disk. Thus, CSR is given by the expression shown in equation 2.4:

$$CSR = \frac{\int_{Circumsolar} B(r)rdr}{\int_{Disk} B(r)rdr + \int_{Circumsolar} B(r)rdr} \qquad (2.4)$$

The upper limit of integration of the circumsolar irradiance is traditionally taken as 2.5^o to 3.5^o. The lack of consensus is a problem.

Several attempts of sunshape measurements have been made previously using telescopes and cameras at different angular acceptance angles. LBL in 1970s used a circumsolar telescope for sunshape measurement; the data for which was interpreted within a half acceptance angle of 2.5^o with the center as the center of the solar disk. DLR had used a CCD camera for the measurement of brightness profiles at three different sites in Europe with a horizontal half acceptance angle of

2.922^{o} and vertical half angle of 1.94^{o}. Buie's empirical model considers a half acceptance angle of 2.5^{o} (similar to LBL) and Gueymard's SMARTS model extends further to a half angle of 10^{o}. The currently used instrument for the measurement of aureole profiles called Sun and Aureole Measurement System captures the aureole images with a half acceptance angle of 9.9^{o}. Although a half acceptance angle of 10^{o} is quite high, but the angular extent could be expected to high in regions like UAE with high humidity, aerosol content, and dust. Figure 2.2 shows the variation of the circumsolar region around the solar disk (black disk with constant diameter) on different days and time periods.

March 6, 2010, 11:03 EST
AOT at 505 and 625 nm: 0.043, 0.029

March 18, 2010, 13:32 EDT
AOT at 505 and 625 nm: 0.079, 0.056

March 19, 2010, 12:25 EDT
AOT at 505 and 625 nm: 0.361, 0.293

March 20, 2010, 12:25 EDT
AOT at 505 and 625 nm: 0.108, 0.075

Figure 2.2: Pictures of the Solar Aureole taken in New Jersey: (Brooks, 2010) http://instesre.org/Solar/AureolePhotography/AsianDust_March2010.htm & (Mims, 2003).

2.4 Sunshape Measurements

Many attempts have been made in the past to measure the solar aureole profiles with various measuring systems involving digital cameras, scanning photometers, and telescopes. Real profiles were acquired using a Charge Couple Device (CCD) camera and the resulting radiance distribution was digitized .These processes were both expensive and labor intensive.

2.4.1 LBL Sunshape Measurements

The first geographically extensive attempt of measuring the circumsolar radiation under many different sky conditions was made by the Lawrence Berkeley Laboratories in the mid 1970's with the help of circumsolar telescope mounted on a precision solar tracker as shown in Figure 2.3. As described by Noring et al. (1991), the telescope scanned through an arc of 6^o with the sun at the center in order to measure the solar and circumsolar brightness as a function of angle. The telescope used an off-axis mirror of 7.5 cm diameter and 1 m focal length as its basic optical element and a fused silica window was used to protect the mirror from the environment. An image of the sun and sky was formed by the mirror on a plate to the side of the telescope axis. The amount of light passing through the aperture into the detector assembly was taken as the fundamental measurement and the angular resolution was defined by the detector aperture and a small hole on the plate. In this way, a set of measurements comprised of one scan at each of 10 filter positions: eight optical filters, one clear and one opaque position respectively. Four telescopes were employed to collect the data from 11 different sites that were assembled into a single database. The different sites across the US include: Albuquerque_STTF, Albuquerque_TETF, Argonne, Atlanta, Barstow, Boardman, China Lake, Colstrip, Edwards AFB, Fort Hood Bunker, and Fort Hood TES. Of the entire collected data using these telescopes, about one tenth was cleaned and compressed into the Reduced Data Base (RDB) and is available in the public ftp site: http://rredc.nrel.gov/solar/old_data/circumsolar/

Figure 2.3: Don Grether and David Gumz with LBL circumsolar telescope (Buie, 2004)

Figure 2.4 shows an example of 20 solar profiles collected by the LBL using the circumsolar telescope plotted in log-log space. The solar and circumsolar regions are shown by a split of an angular displacement of 4.65 mrad. A string of status flags in the RDB indicates the quality of the data profiles. To ensure that poor data is removed from the RDB, it was required that the solar radiation comes from clear skies only. The data contains right position of the aperture; sun must be centered in the scans, closed rain flap, etc. It was found that only 15% of the original 180,000 solar profiles fitted these conditions and this clean, filtered data that met the above condition was referred to as the RDB by (Buie, 2004).

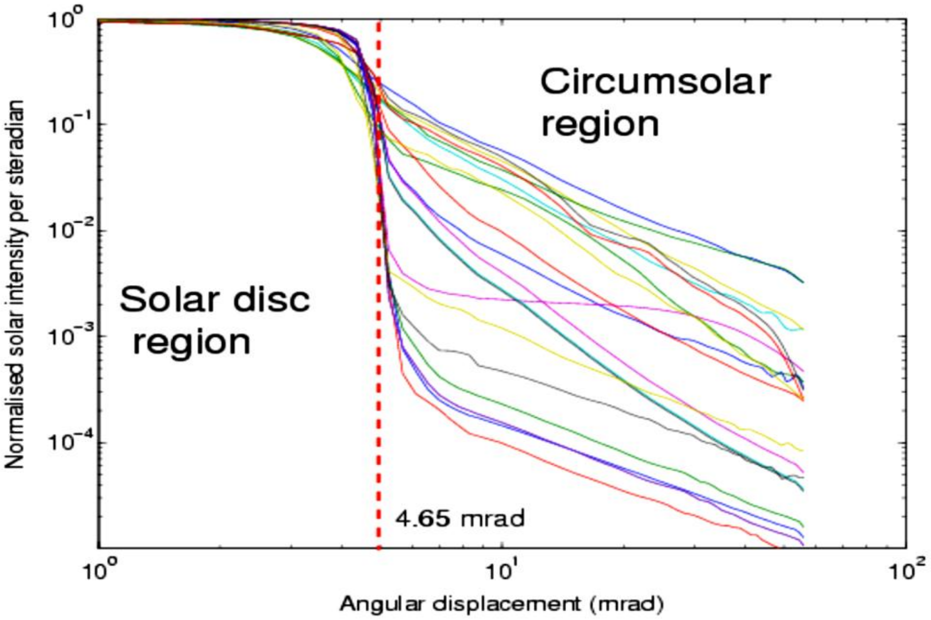

Figure 2.4: Solar Profiles from the LBL data (Buie, 2004)

Each solar profile was normalized against the central intensity measurement and the filtered profiles of the reduced data base were grouped according to their corresponding CSR from 0.01 to 0.8 in steps of 0.01 as shown in Figure 2.5.

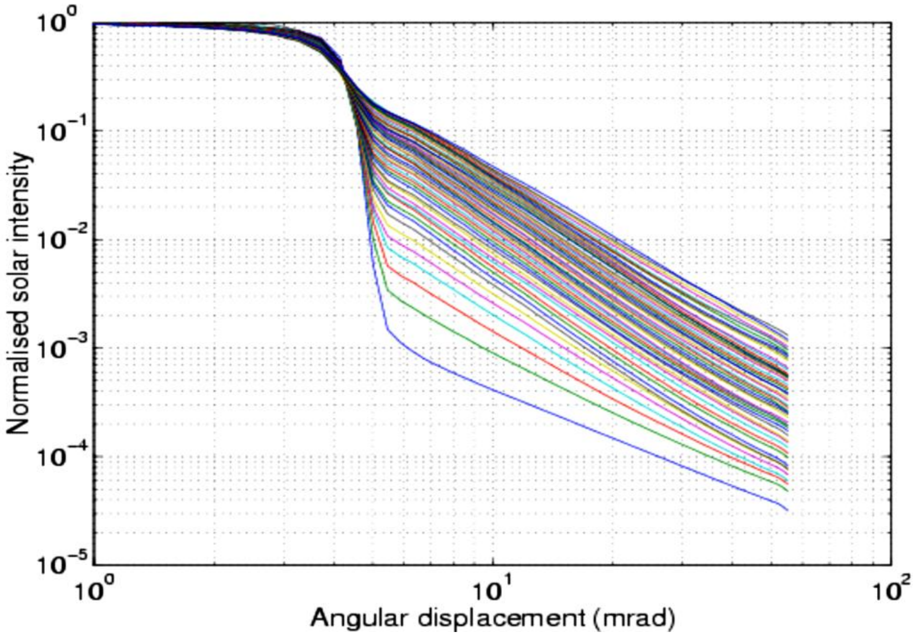

Figure 2.5: Filtered Solar Profiles from the RDB from CSR's 0.01 to 0.8 (Buie, 2004)

2.4.2 DLR Sunshape Measurements

The first sunshape measurements at DLR Cologne started in 1991 (Neumann & Witzke, 1999) using the sunshape measurement system shown schematically in Figure 2.6. The solar and circumsolar images were recorded by a digital camera of 12-bit resolution. The CCD chip was thermoelectrically cooled to +10^{o}C in order to reduce the thermal noise and stabilize the background image. Optical filters were incorporated in order to reduce the intensity of sunlight entering into the camera. 2300 solar profiles were acquired from three different sites across Europe: DLR Cologne (Germany), PSA (Spain) and CNRS Solar Furnace (France). These profiles were grouped and filtered in a similar manner as the Reduced Data Base; however larger ranges of CSRs were accepted for each sunshape bin (Buie, 2004). A pyrheliometer and a pyranometer were added to the measurement set up for performing the correlation analysis of the CSR with DNI and GHI (Neumann, von der Au, & Heller, 1998). The CSR was determined by recoding two- dimensional angular distributions of the incident solar radiation. The diameter of the solar disk on the CCD chip was determined by using a measured spatial calibration factor in mrad/pixel and the centroid in each image was also calculated. Due to the generation of some stray light on the CCD chip by the tele lens mounted on the camera, the outer circumsolar region was affected and hence, the minimum measurable CSR values were found to be not below 2.5%. However, the DLR measurements provided higher quality data at each imaging point as well as greater number of data points across the transition between the solar disk and aureole. The instantaneous capture of images with CCD camera was more advantageous as opposed to one minute time interval taken by the LBL telescope because shorter time span provides higher probability of acquiring self-consistent profiles. Figure 2.7 shows the averaged (filtered) DLR sunshape profiles comprising approximately 10% of the data pool.

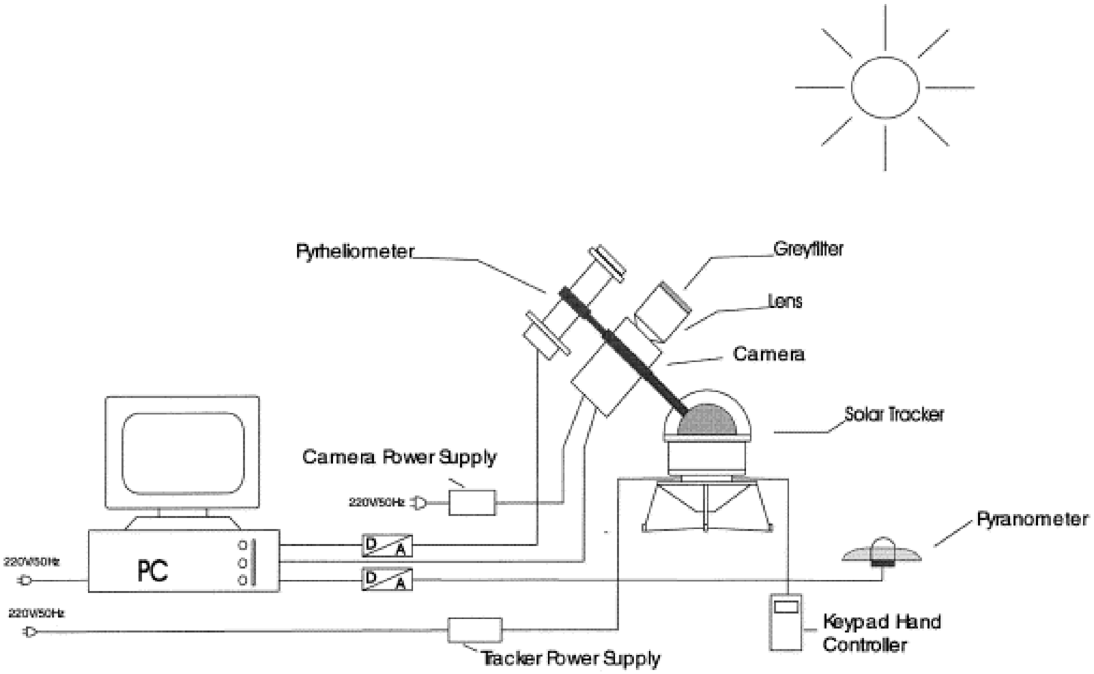

Figure 2.6: Block diagram of the sunshape measurement system used at DLR (Neumann & Witzke, 1999)

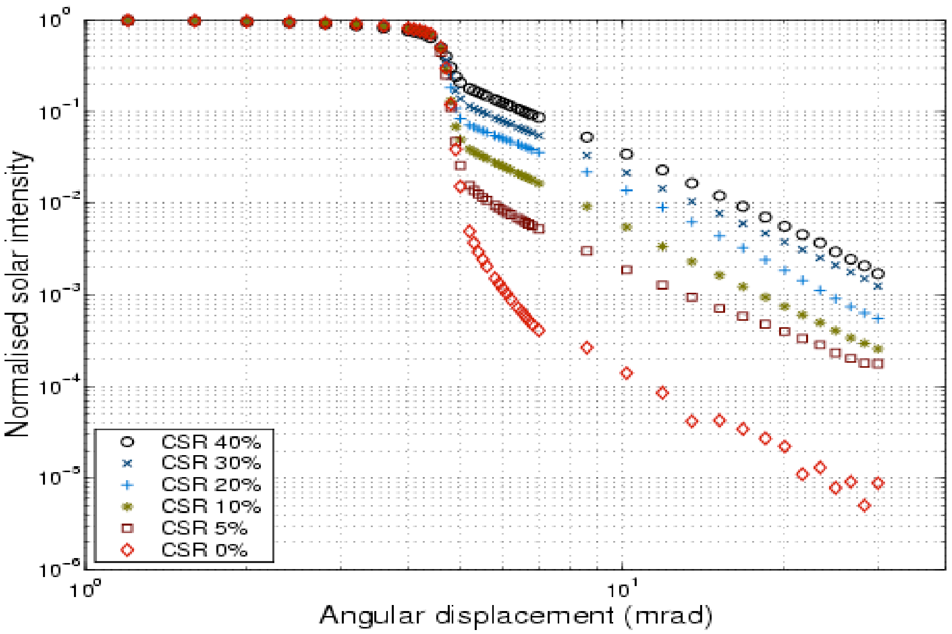

Figure 2.7: Averaged solar profiles from the DLR sunshape measurements (Buie, 2004)

2.4.3 Teide Observatory Solar Aureole Measurements

Solar Aureoles were measured with the help of the vacuum Newton telescope of the Teide Observatory (OT) with 40-cm aperture as described by Jorge et al. (1998). The aureole profiles were measured using a pinhole photometer at different wavelengths as shown in Figure 2.8 and air masses of the range of 1-2.5. A total of 12 aureoles were measured in a day and using blind and guided extrapolation techniques, aureole profiles were extrapolated to the infrared wavelengths from the visible wavelengths as shown in Figure 2.9, in which R_θ is the angular extent of the aureole from the solar limb. The blind extrapolation technique required the assumption that the aureoles follow the Angstrom formula ($K_\lambda^a = \beta\lambda^{-a}$) and separate instrumental and atmospheric components of the aureole could be computed. Values of β and α were fitted at each distance from the limb and the value at the IR wavelength was found. The guided extrapolation was obtained by carrying out radiative- transfer and Mie- calculations which agreed fairly well with the results from the blindly extrapolated aureole.

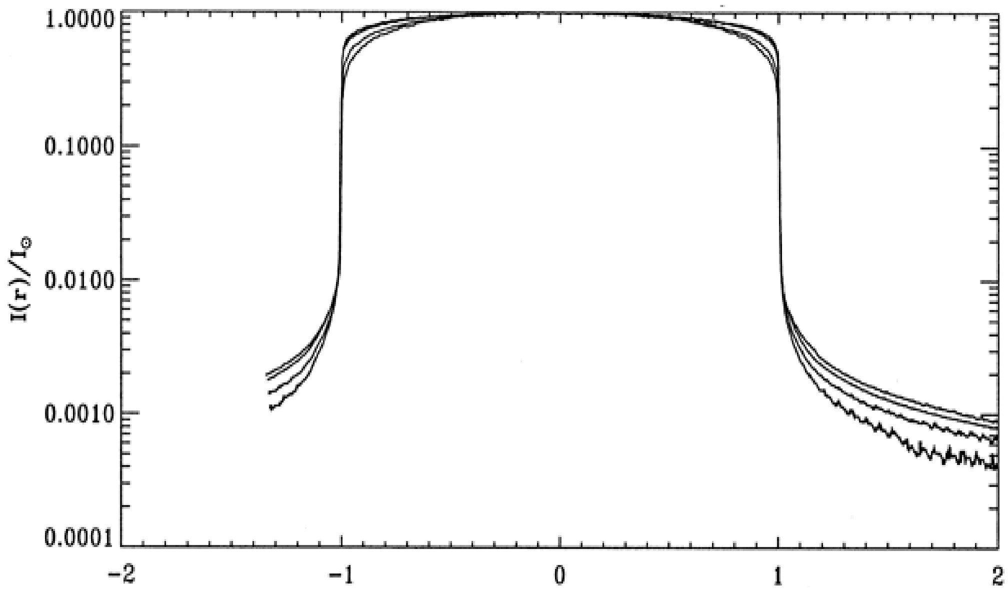

Figure 2.8: Aureole Profiles observed 8 July 1997 at Teide Observatory (Jorge et al. (1998)

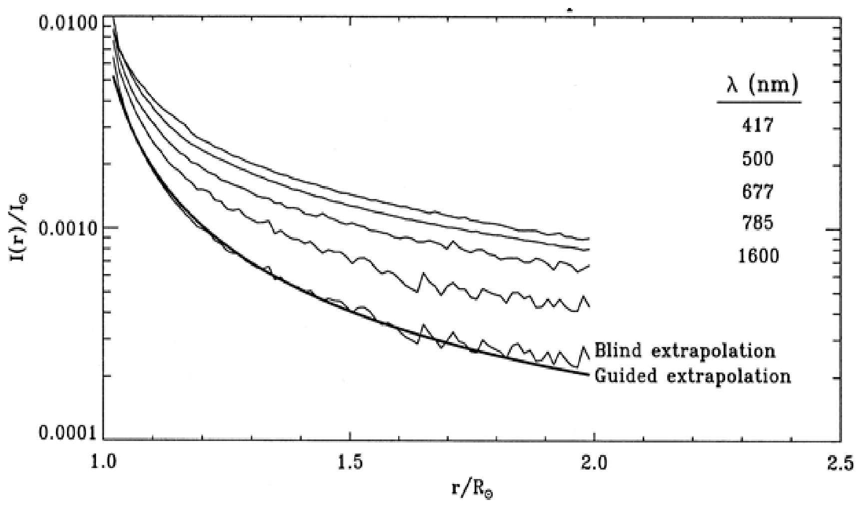

Figure 2.9: Aureole profiles with extrapolated results from Jorge et al. (1998)

2.4.4 Solar Aureole Radiance Distribution Measurements from Unstable Platforms

A novel imaging solar aureole radiometer was described by (Ritter & Kenneth, 1999) which can be operated on an unstable platform (e.g. ship or airplane) using a CCD array to image the aureole, while a neutral density occulter on a long pole is used to block the direct solar radiation.

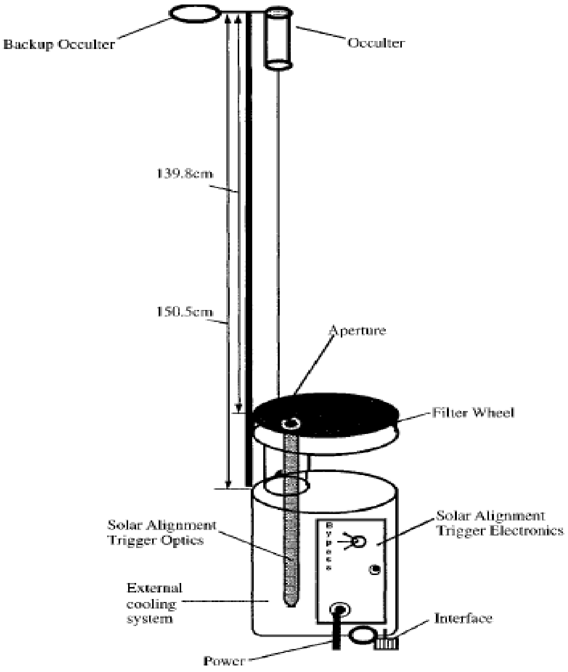

Figure 2.10: Schematic of the imaging aureole radiometry system (Ritter & Kenneth, 1999)

This instrument (Figure 2.10) acquired the circumsolar radiance up to half angular extent of 7.5° of the center of solar disk. The combination of an imaging radiometric instrument with the presence of an image of the solar disk and the use of optoelectronic alignment and triggering system makes this instrument very unique.

2.5 Sky Models

Irradiation from the circumsolar region was recognized and included in some sky models since at least 1979 (Hay & Davies, 1980). The circumsolar diffuse component on a tilted collector in the Hay and Davies model is based on the assumption that all of the diffuse radiation can be divided into two parts: the isotropic and circumsolar, given by (Duffie & Beckman, 2006, Third Edition):

$$I_{d,T} = I_{T,d,iso} + I_{T,d,cs} \tag{2.5}$$

Anisotropy index determines a portion of the horizontal diffuse radiation that is treated as forward scattered and is defined as a function of transmittance of the atmosphere for beam radiation as shown in equation 2.6:

$$A_i = \frac{I_{bn}}{I_{on}} = \frac{I_b}{I_o} \tag{2.6}$$

where I_{bn} is the beam normal irradiance and I_{on} is the extra-terrestrial irradiation. The diffuse radiation on a tilted collector is thus, given (Duffie & Beckman, 2006, Third Edition) by:

$$I_{d,T} = I_d \left[(1 - A_i)\left(\frac{1+cos\beta}{2}\right) + A_i R_b\right] \tag{2.7}$$

where $I_{d,T}$ is the total diffuse radiation on the horizontal surface, I_d is the horizontal diffuse radiation, $I_{T,d,iso}$ is the isotropic diffuse and $I_{T,d,CS}$ is the circumsolar diffuse component of solar radiation. However, the sunshape effect remains unchanged with the tilt, so the slope of the collector treated as 0 (β=0) gives the total diffuse radiation as a combination of circumsolar and isotropic diffuse radiation. Perez model (Perez, Seals, Ineichent, Stewart, & Menicucci, 1987) includes the horizon brightening factor along with the circumsolar brightness factor with more detailed analysis of all the three components of the diffuse radiation, given by equation 2.8 (Duffie & Beckman, 2006, Third Edition):

$$I_{d,T} = I_d \left[(1 - F_1) + F_1 \frac{a}{b}\right] \tag{2.8}$$

Slope (β) can be treated as zero to obtain the horizontal diffuse component since sunshape is not germane to the tilt of the collector. F_1 is circumsolar brightness coefficient, a and b account for the angles of incidence of the cone of the circumsolar radiation on tilted and horizontal surfaces. These brightness coefficients are functions of three parameters- zenith angle, clearness and brightness. Perez also defined the reduced brightness coefficients which represent the respective normalized contributions of the circumsolar and horizon regions to the total horizontal diffuse radiation (Perez, Seals, Ineichent, Stewart, & Menicucci, 1987). The circumsolar region extending up to 25^o half angle was found to provide the best overall performance and results for 0^o point source, 35^o, 15^o and 25^o are also presented. It is important to note that the circumsolar region in this model was assumed to have a fixed width with a homogenous circular zone and has an extremely coarse angular resolution. Hence, this kind of circumsolar representation can be acceptable only for collecting elements with wide field of view (eg. flat place collectors). In order to obtain the actual radiance profiles of the circumsolar region and the disk, a more detailed description of the forward scattered radiation accounting for the insolation conditions of the radiance profiles is needed.

2.6 Gueymard Model for Correction of Circumsolar Spectral Irradiance

The circumsolar irradiance ($E_{dc\lambda}$) is described as a function of atmospheric scattering processes and aerosol optical characteristics and wavelengths, given by equation 2.9 (Gueymard, 2001):

$$E_{dc\lambda} = 2\pi \int_0^{\xi_1} L_{a\lambda}\,(\xi) P(\xi) sin\xi cos\xi d\xi \tag{2.9}$$

where $L_{a,\lambda}(\xi)$ is the azimuthally averaged radiance that exists along the almucantar, $P(\xi)$ is the phase function, ξ_1 is the maximum half viewing angle.

An aerosol scattering function normalized to 1 that describes the forward peaked scattering pattern of aerosol particles is discussed by (Gueymard, 2001), which is specific to each aerosol's size distribution and refractive index, calculated from Mie Theory. All calculations are simplified through a library of functions of ξ in SMARTS2. The aerosol single scattering albedo, fictitious optical depth due to molecular multiple scattering, augmentation of the radiance by back scattering processes between ground and atmosphere are also evaluated in order to obtain the circumsolar correction factors for different wavelengths and air masses. All this can be performed on SMARTS to predict the spectral and broadband circumsolar irradiance within a cone of any angle up to 10^o half angle around the sun under clear sky conditions. Figure 2.11 demonstrates that the CSR is highly variable, depending on the solar zenith angle, wavelength, humidity, aerosol optical depth and also to the radiometer's aperture angle.

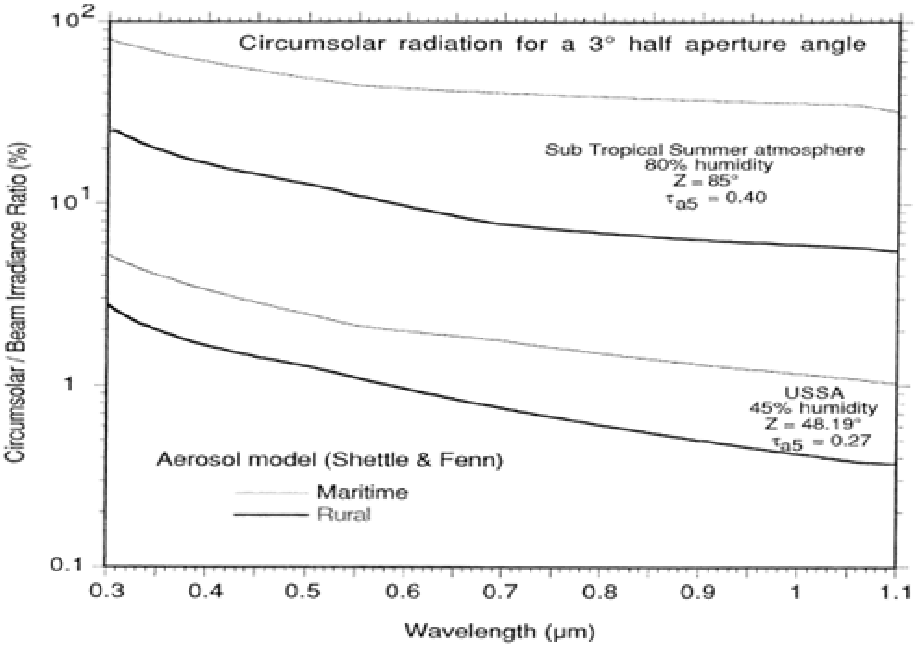

Figure 2.11: Spectral Circumsolar Irradiance Contribution to the Beam Irradiance for different atmospheric conditions (Gueymard, 2001)

2.7 Rotating Shadowband Irradiometer (RSI)

Diffuse and global horizontal radiation components can be continuously recorded with pyranometers by shading the instrument from direct beam radiation by means of a rotating shadowband. Adjustments for latitude are made once at the time of installation and a correction for the shading of a part of diffuse radiation by the shadowband is estimated and applied to the observed diffuse radiation (Duffie & Beckman, 2006, Third Edition). The direct normal irradiance (DNI) is calculated from the obtained global horizontal (GHI) and diffuse horizontal (DHI) components of solar radiation as equation 2.10:

$$DNI*\cos(\theta_z) = GHI - DHI \qquad (2.10)$$

A microprocessor controlled rotating shadowband irradiometer was described by Michalsky et al. (1986)that consists of a silicon cell pyranometer on a metal stand containing a stepping motor with 0.9^{o} steps that drives the shadowband about a polar axis as shown in Figure 2.12. The vertical component that contains the latitude adjustment track is oriented due north- south with the base in order to orient the motor axis parallel to the rotation axis of the earth.

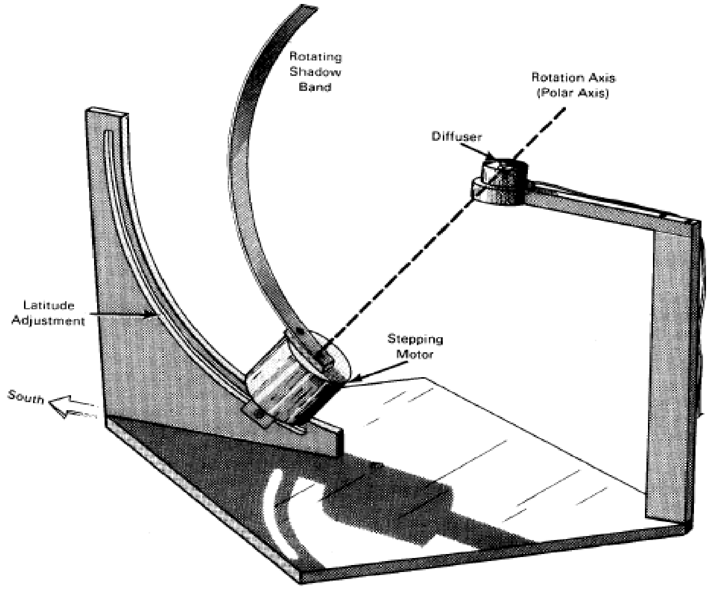

Figure 2.12: Rotating Shadowband Irradiometer (Michalsky, Berndt, & Schuster, 1986)

One digital line is required to send pulses to the stepping motor which is driven in a single direction. The silicon cell produces current output which is converted to a voltage signal by an operational amplifier. This device was first designed to be used as a day lighting resource assessment tool to obtain the three components of radiation available to a site (Michalsky, Berndt, & Schuster, A Microprocessor- Based Rotating Shadowband Radiometer, 1986). It was observed that the unfiltered silicon channel only responds to wavelengths between 300 and 1100nm and does not have a uniform spectral and temperature response (Michalsky, Augustine, & Kiedron, Improved broadband solar irradiance from the multi-filter rotating shadowband radiometer, 2009). With the help of multi-filter rotating shadowband radiometer (MFRSR), the total and diffuse horizontal and direct normal irradiance were obtained using six 10-nm filter detectors with center wavelengths near [415, 500, 615, 673, 870 and 940 nm] and an unfiltered detector. Today, the MFRSR is being widely used to measure the solar irradiance components at different locations. Some of the places using the MFRSR have been listed in Appendix B.

2.8 Sun and Aureole Measurement System (SAM)

The Solar and Aureole Measurement (SAM) system was developed by Visidyne Inc. to measure the Forward Scattering properties of cloud particles and the optical depth of clouds. This forward scattering of sunlight caused by cloud particles produces the sun aureole. This system has been newly designed in 2008 with the capacity of partially unattended operation. Using an analytical algorithm formulated by Visidyne, the size distribution of the light scatterers can be determined from the measured angular radiance profiles of this region (Visidyne, 2011). In order to model the sunshape and obtain the circumsolar ratio of a location, a sunshape measurement system was set up at the PSA, Spain which consisted of the SAM instrument, a sun photometer (CIMEL) and post processing software developed for this purpose. The same set up and algorithm has been used at Masdar for the measurement of the CSR with the help of DLR researchers.

2.8.1 Description of the SAM System

The SAM instrument uses a pair of calibrated imaging cameras to measure the irradiance of the solar disk and the sun aureole. The components of the sensor include (SAM-400 User's Manual_v03, 2011):

- Two spectrally- filtered and calibrated CMOS imaging cameras
- A precision solar tracking mount
- A computer control suite with specialized control software
- Data processing algorithms to process the image data

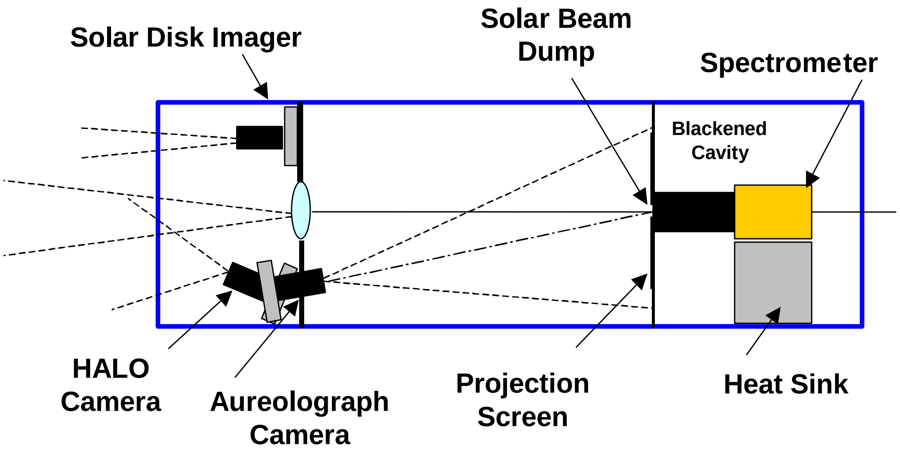

Figure 2.13: Schematic diagram of the principle components of the SAM Optical Head Assembly (SAM-400 User's Manual_v03, 2011)

The SAM system combines two cameras in order to obtain data over large dynamic range to cover the span of radiances from the solar disk to the aureole shown in Figures 2.13 and 2.14.

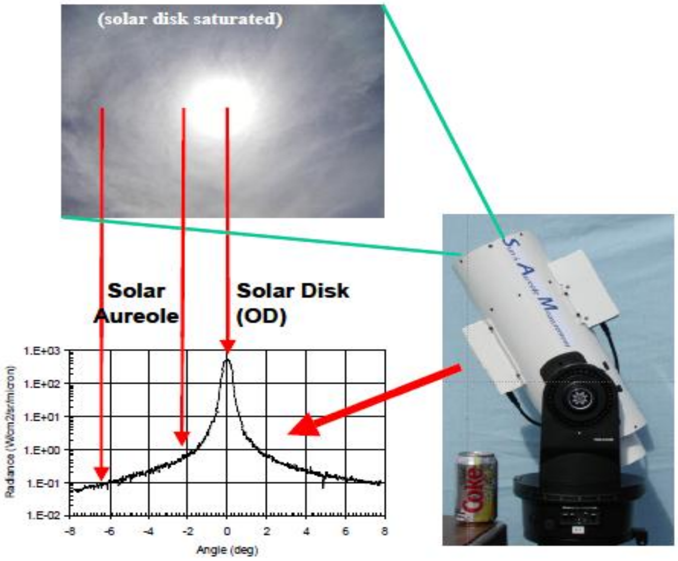

Figure 2.14: Images of the solar disk and the aureole with the SAM and their radiance profile (LePage, Kras, & DeVore, 2008)

The two cameras that are used for imaging include a Solar Disk imager (that directly captures the solar disk) and an aureolograph assembly that images the solar disk into a beam dump allowing the much dimmer aureole to be visible. The image from the aureole camera is required to have a wide angular field around the sun which implies to have a short focal length lens, whereas, the image size of the solar disk needs to be large (long focal length). Hence, the choice of lens is made according to these requirements The SAM optical head assembly (OHA) is mounted on a precision tracker with active tracking feedback that keeps the instrument pointed to the solar disk to within 0.1^o. The tracking takes place in continuous flywheel mode, following the path calculated by an internal ephemeris when the solar disk is not visible. The OHA assembly that is being used in Masdar (Figure 2.15) is also fitted with a high resolution thermoelectrically-cooled spectrometer for column water and aerosol measurements.

Figure 2.15: SAM Sensor mounted on the Radiometer Platform at Masdar

2.8.2 Analysis of SAM Images

A flowchart for the collection and analysis of solar aureole data obtained with SAM is discussed by Devore et al. (2009) as shown in Figure 2.16. The processing of SAM data consists of a series of automated transformations. From each sequence of the Solar Disk (SD) images, the unsaturated image with longest integration time is chosen for calibration such that it provides the best signal-to-noise ratio among the SD images. Dark images are acquired at the beginning and end of each observation session in order to subtract them from the raw images.

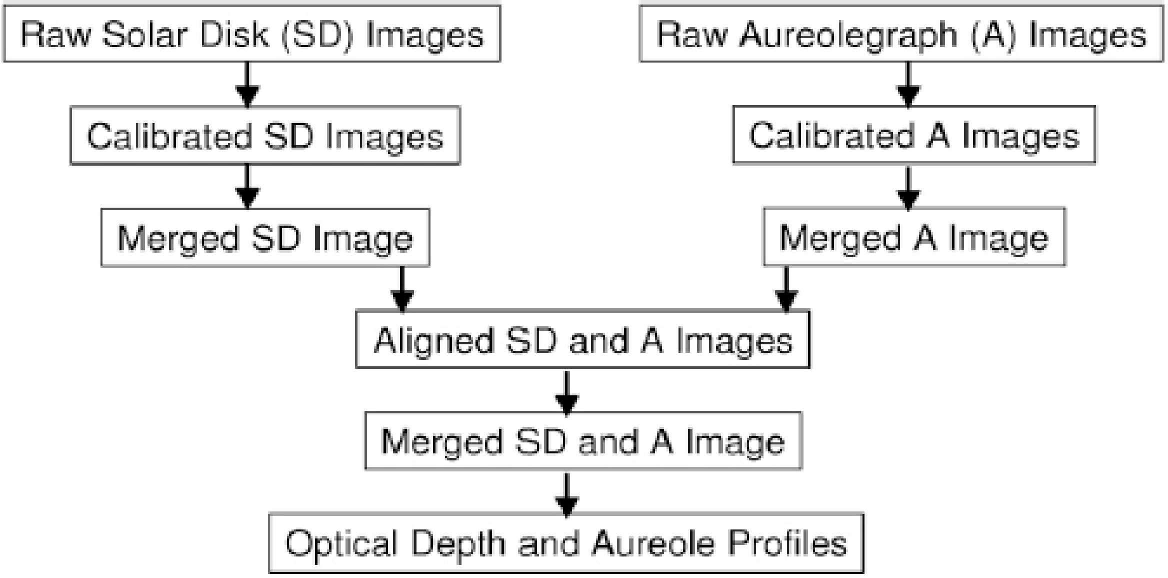

Figure 2.16: Flowchart of data collection and analysis from the SAM (Devore, et al., 2009)

A calibration algorithm is applied to convert the raw data consisting of number values into units of spectral radiance ($Wm^{-2}sr^{-1}nm^{-1}$). After this, the aureolograph (A) images are processed where in each raw A image sequence has the dark image corresponding to the subtracted integration time and then calibrated into units of spectral radiance with a procedure similar to the SD images. The SD image is shifted, rescaled, cropped and placed inside the empty beam dump portion of the A image stack with the relative alignments of the SD and A as explained by

Devore et al. (2009). For each aureole recorded by the SAM, a mean profile and an associated approximate particle size distribution are derived from the diffraction approximation.

Wilbert et al. (2011) discussed that the images produced by the solar disk camera cannot be used for radiances below 1/4th of the central irradiance of the disk due to scattering effects in the optics. Hence, the photograph of the disk cannot be used for the angular distances that are greater than the disk angle. This happens for low CSRs due to which a data gap between the edge of the disk and an approximate angle of 0.475° from the center occurs when the two images are combined. For higher CSRs, the data gap decreases because the images of the solar disk camera can be used up to higher angles. A detailed post processing analysis and its uncertainties have been discussed by Wilbert et al. (2011). The spectral dependence of the solar radiance profiles has been explained by the approximation shown in equation 2.11:

$$L(\lambda,\theta) = P(\lambda,\theta).F_s(\lambda).\frac{\omega(\lambda)\tau(\lambda)}{4\pi\mu_s}.\exp\left(-\frac{\tau(\lambda)}{\mu_s}\right) \tag{2.11}$$

F_s is the extra-terrestrial solar flux, ω is the single scattering albedo, τ is the total vertical optical depth, μ_s is the cosine of the Solar zenith angle and θ is the scattering angle that is approximated by the angular distance between a point in the sky and the center of the solar disk. The diffraction process as described by Fraunhofer theory is used at the wavelengths of interest and for particles sizes around 10μm as follows:

$$\mathrm{P}\left(\lambda 2, \alpha 2\ =\ \alpha 1.\frac{\lambda_2}{\lambda_1}\right) \sim P(\lambda_1,\alpha_1).\left(\frac{\lambda_1}{\lambda_2}\right)^2 \tag{2.12}$$

Combining the equations 2.11 and 2.12 an expression for scattering in most clouds was obtained from which the normalized spectral radiance profiles are calculated from another profile using the ratio of two considered wavelengths as shown in equation 2.13 by Wilbert et al. (2011):

$$L\left(\lambda 2, \alpha 2 \;=\; \alpha 1.\frac{\lambda_2}{\lambda_1}\right) \sim L(\lambda_1, \alpha_1).\left(\frac{\lambda_1}{\lambda_2}\right)^2 \frac{F_S(\lambda_2)}{F_S(\lambda_1)} \qquad (2.13)$$

The aerosol phase function P (θ) is calculated using Mie theory for water drops with radii from 0.1 to 10 µm. For scattering angles greater than 50°, Rayleigh scattering competes with aerosol scattering. Figure 2.17 shows the phase function for Rayleigh scattering and marine stratus layer along with aerosol scattering.

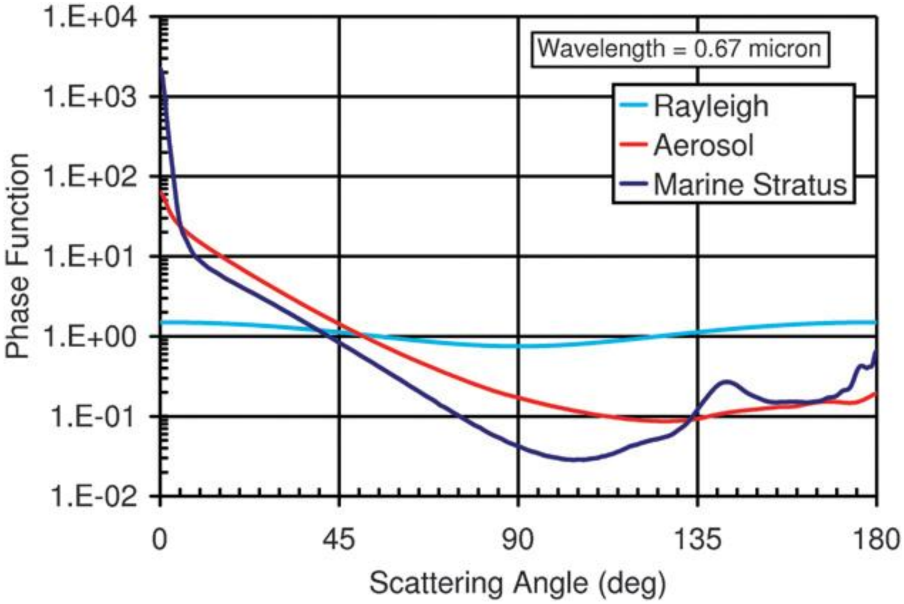

Figure 2.17: Phase Function for aerosols used in SAM

The total optical depth of the atmosphere column between the SAM and sun is obtained by averaging the radiance over the solar disk and comparing it with a fiducial exoatmospheric value. The total optical depth is multiplied by the cosine of the solar zenith angle in order to obtain the total vertical optical depth from the top of the atmosphere to the observer (Devore, et al., 2009). The diffraction approximation described by (Devore, et al., 2009) is applied to the SAM measurements to derive the effective radii of cloud particles and particle size distributions. Smaller particles near the boundary layer cumulus and aerosols produce a shallower aureole profile and result in a steeper particle size distribution. A theoretical relationship between the slope of the aureole profile and size distribution of the particles in the atmosphere is based on approximating scattering that depends solely on diffraction. The aureole radiance is obtained as a combination of two layers comprising of SAM- measured aureole radiance reduced by transmittance of the aerosol layer and SAM- measured transmittance of cloud layer as discussed by Devore et al (2009).

CHAPTER 3

Sunshape Profiling Irradiometer

The design and development of the SPI for retrieving the radial profile of solar flux across the sun’s disk and the circumsolar region is described in this chapter. The SPI can provide CSRs for solar resource assessment, estimates of turbidity useful to climate research and collection of real-time data that may be useful input to global or regional weather forecasting models at very low cost and maintenance. The SPI signal trajectories can be used to infer the circumsolar ratio at a given time and location with a suitable inverse model, also proposed in chapters 4 and 6. The absorption and scattering of solar radiation in the atmosphere, total aerosol column mass and size distribution (especially when used in conjunction with multi-filter detectors), atmospheric radiation balance etc. can be inferred from the irradiance profiles generated by this instrument. An SPI prototype has been built by modifying a stepping-motor-based Rotating Shadowband Irradiometer (RSI) with minor changes to the CR1000 control and data collection program and mechanical modifications that are novel yet simple. While our main contributions are in post processing, the choice of instrument is also crucial. There are several reasons behind choosing the shadowband design for the SPI:

- A single detector is used to generate the sunshape profile thus eliminating calibration problems that commonly occur while using high resolution cameras.

- Pointing errors and misalignment problems are reduced with the SPI because it uses a single (polar) axis sweep mechanism with exactly reproducible step size.
- The single axis mechanism is reliable and requires no maintenance.
- Circumsolar telescopes and cameras like the Sun and Aureole Measurement System cost on the order of $80,000, whereas a conventional RSI costs about $3000.
- There is no requirement of continuous calibration after the SPI is installed and aligned once. Useful information can be obtained even when the fore optic becomes soiled.

3.1 SPI Design Options

Different design combinations of the receiver and shadowband have been considered for the SPI and a sensitivity analysis has been performed numerically for each design (Kalapatapu, Armstrong, & Chiesa, 2011). Three different types of receivers – point, slit and circular have been modeled to verify their sensitivity to noise. To each of these receiver types, three different shadowband geometries (full globe, half globe, and regular RSI) have been combined to determine which combination is least sensitive to the same noise added. This analysis has been performed in order to assess the effect of shading and detector geometry on the sensitivity of sunshape retrieval, based on which a point receiver with a full globe band has been observed to be the best design for the SPI. However, a point receiver gives insufficient signal. Instead, a modified optical receiver with a narrow slit on a black foil has been considered for the SPI prototype as shown in the third model of Figure 3.1.

Figure 3.1: Point, Circular and Slit receivers (Kalapatapu, Armstrong, & Chiesa, 2011)

The three different shadowband models considered in the analysis are illustrated in Figure 3.2 in which the third model has been used for the SPI prototype. Although the slotted full globe model is least sensitive to noise for the sunshape retrieval, the conventional RSI model has been modified and used for the SPI prototype because access to machining and fabrication services in UAE is very limited. Also, this model requires low maintenance because the cleaning of the full globe model would be more difficult as compared to a regular RSI model.

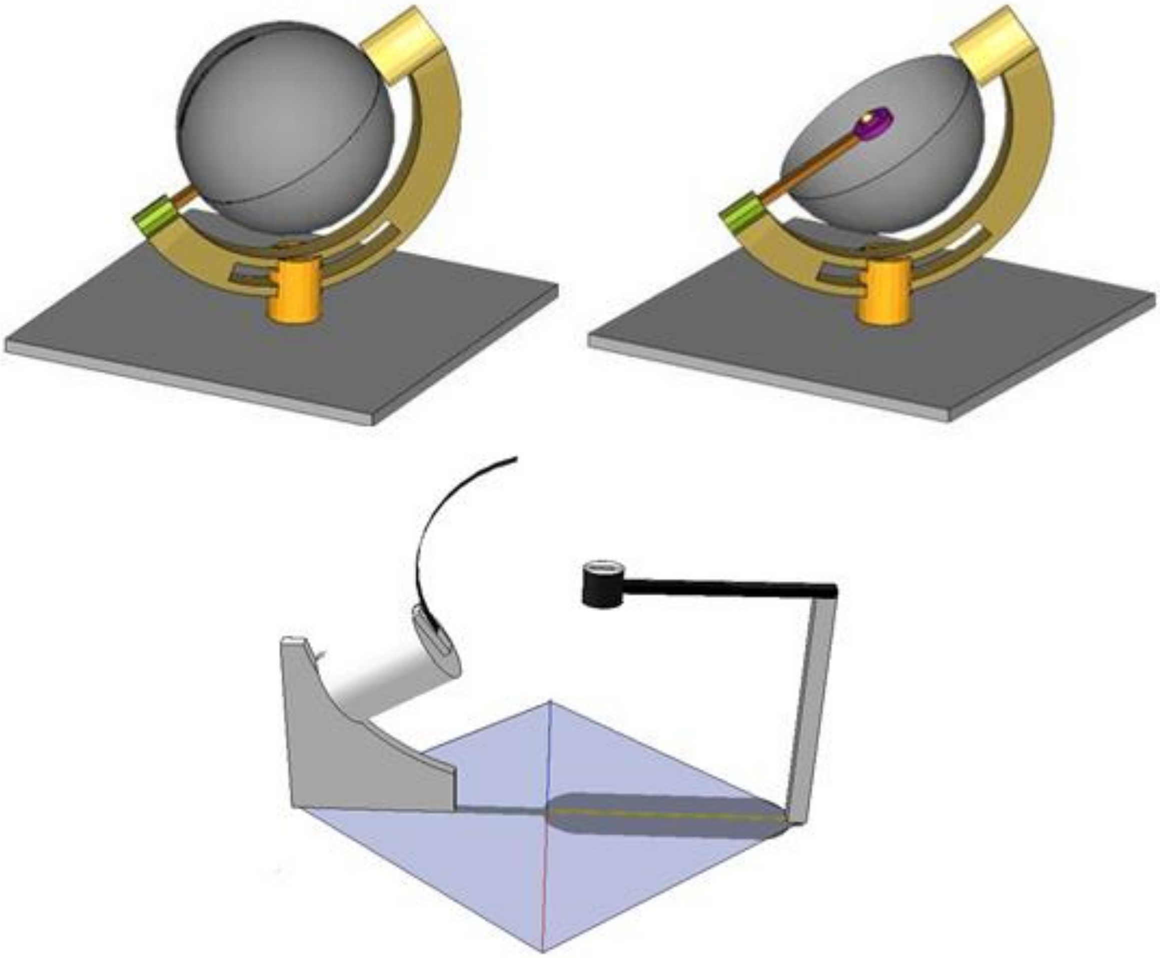

Figure 3.2: Alternative shading devices for SPI a) Slotted full globe b) Half globe c) Traditional RSI (Kalapatapu, Armstrong, & Chiesa, 2011)

3.2 Description of the SPI

A stepper motor driven polar-axis Rotating Shadowband Irradiometer (RSI) has been modified to build the SPI prototype. The modifications on typical RSIs entail using a modified optical slit receiver with azimuth= 0^o and tilt equivalent to the latitude of the location such that the North-South diameter of the receiver is on the band- motor (polar) axis as shown in Figure 3.3. Effective resolution of 800*26= 20800 micro steps/revolution in half- step mode is achieved by scanning the circumsolar and solar disk regions 26 times in 2 minutes. (The half stepping gives a resolution of 0.45^o and 800 steps per revolution). The Licor receiver is covered with a piece of black foil into which a very narrow rectangular slit is cut from the center on the axis line in order to sharpen the corners of the trough like SPI trajectory. Thus, the amount of rounding of the corners of the trough is related in a more sensitive way to the circumsolar radiation. Figure 3.4 illustrates the modified slit receiver in the SPI prototype.

Figure 3.3: Sunshape Profiling Irradiometer (SPI) prototype

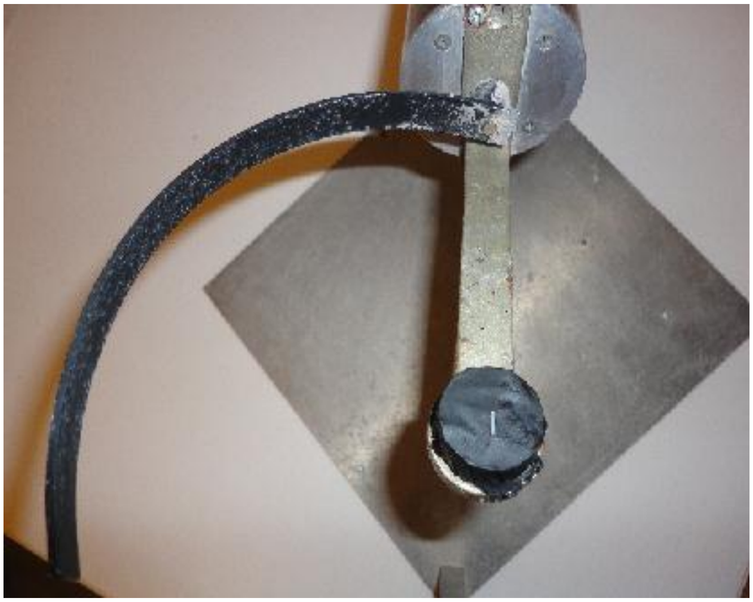

Figure 3.4: SPI receiver with a black foil and a slit at the center

3.2.1 Hardware and Connections

The hardware and other connections for the SPI prototype are listed in Table 3.1.

Table 3.1: Hardware and Connections in SPI

Part	Function	Model
Driver Chip	Converting the step and direction commands to power signals in proper phase sequence	Allegro UCN5804B
Motor	Rotating the band continuously and performing the Sweeps back and forth around 9.25^o half angle of the sun	Vextra PH264-02B
Cable	Carrying the Power and home signal from the driver to the motor	Round or Square (Motor end) to Driver End
Controller	Programming, time-keeping, input-output of the data, collection and pre- processing of the resulting data	Campbell Scientific CR1000
Receiver-detector	Measuring the radiation falling on the diffuser element	Licor PY200 Pyranometer
Bracket	Holding the receiver on the band-motor (polar) axis	Generic

3.2.2 Mechanical Configuration

Like the conventional RSI (Michalsky, Berndt, & Schuster, 1986), the SPI shading band is also driven by a stepper motor mounted on a track formed into a circular arc centered on the receiver. Latitude adjustment of the instrument is made possible by placing the motor on this track between 0^o and $\_+ 65^o$ very accurately, according to the latitude of the location. Some of the shadowband based instruments provide a 3-position track only for high, medium and low latitudes but for the SPI it is important to position the tilt of the motor axis with horizontal very accurately at the latitude angle. The shadowband arc is made long enough to ensure the occultation of the diffuser on the receiver on all days of the year and the angle subtended for all positions of the shadowband must be the same. The band radius (distance between the center of the diffuser and the band) is 85mm. The total range of 47^o of the sun's declination is accommodated by the shadowband arc of 117.75^o (90^o+ 23.5^o (declination) + 4.25^o (subtended half angle of the band)).

3.3 SPI Operation and Control

A CR1000 data logger is used for the SPI control functions and measurement of the radiation on the receiver. It consists of a CPU, analog and digital inputs/outputs, and memory which are controlled by the operating system in conjunction with a user defined program. The user program is written with a BASIC like programming language that includes data processing and analysis routines (Campbell Scientific, 2008). The stepping sequence, calculation of the sun position, measurement of irradiation, data storage and collection with time- are all programmed with the CRBasic programming language. Figure 3.5 shows the CR1000 unit with motor control printed circuit board and cables of the SPI. The analog specifications of CR1000 are included in Appendix C.

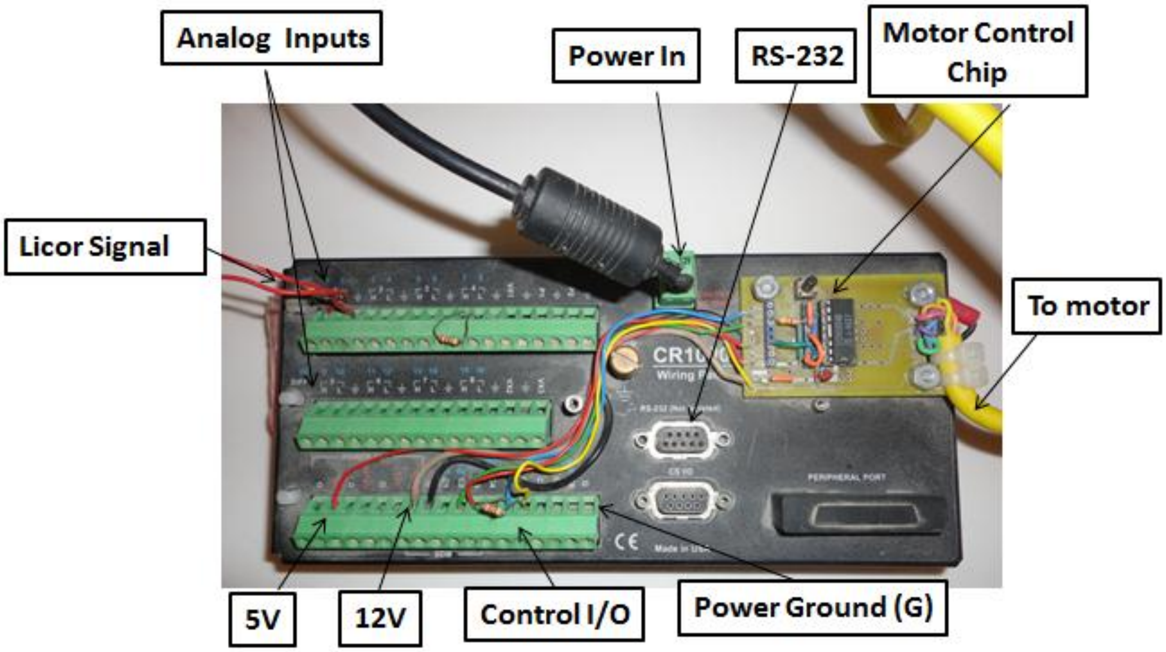

Figure 3.5: CR1000 data logger used in SPI and its components

The refraction corrected hour angle is calculated according to the local solar time based on the real time of the CR1000 controller. Hence, an accurate time keeping and physical alignment of the instrument as well as correct latitude, longitude specification in the control program must be ensured. The logger time must be set and maintained within one minute of the Coordinated Universal Time (UTC). The controller generates the half stepping sequence and rotating direction in response to a series of step pulses determined by the state of its Direction and Half inputs which are normally wired to the CR1000 control terminals C2 and C3 and the Home signal is wired to C5.

The operation of the SPI includes a sequence of steps and sweeps in a span of 2 minutes. The SPI is programmed such that the shadowband starts from its home position, then calculates the position of the sun very accurately and its corresponding step number to reach the sun position. The program instructs the shadowband to stop 21 half steps before the actual sun position (9.25^{o})

from where it starts its first sweep of 41 steps, keeping the solar disk at the middle. The measured radiation at the receiver from the sweep of the shadowband in 41 steps gives a trough like trajectory of angular solar irradiance. After the 41^{st} step, the shadowband goes back to its first step very quickly, and starts the second sweep after 4 seconds. In this way, it performs 26 sweeps in 1.8 minutes and then goes back to its home position to wait for the completion of 2 minutes so that the program re-calculates the sun position and repeats the same sequence of sweeps and steps after every 2 minutes.

Each half step of the stepper motor covers an angle of 0.45^{o}, so the resolution of the steps is increased by utilizing the sun's motion from the 26 sweeps traversed by the shadowband. In this way, the sunshape trajectories generated by the SPI consist of higher resolution data points at regions of interest, i.e. the solar disk and circumsolar region.

3.4 Orientation of the Receiver

The SPI receiver is mounted on the band motor (polar axis) with a supporting bracket attached to the stepper-motor case as shown in Figure 3.3. The reason behind modifying the orientation of the receiver is to eliminate the angular movement of the shadow cast by the band on the receiver with time of the day. Two cases with respect to the orientation of the receiver were observed and analyzed for measuring the sunshape profiles:

- Horizontal Receiver- slit arranged horizontally in the N-S direction (conventional RSI).
- Tilted Receiver- slit coaxial with motor axis in the N-S direction (as in SPI).

3.4.1 Shadow Analysis

During the morning and evening hours of the day, the non-parallel alignment of the horizontal slit receiver with respect to the motor axis results in an angular movement of the shadow on the slit. The analytical signal was observed to match with the experimental results only during the noon time, when the shadowband is parallel to the slotted receiver. This has been demonstrated in Figure 3.6 by analyzing the shadow with detector geometry using Google Sketchup Tool for solar noon time. Figure 3.7 illustrates the angular shadow cast on the same slit horizontal receiver in the afternoon at 14:30. This shows that the slot ends have very different views of the solar disk before and after noon. Due to this misalignment, it was realized that axial alignment is needed for the slit alignment. A new design of the receiver position has been tested and implemented for the SPI by means of a bracket that holds the receiver in the polar axis. Figure 3.8 demonstrates the perfectly aligned receiver case in which the shadow of the band is always aligned on the slit axis during all times of the day.

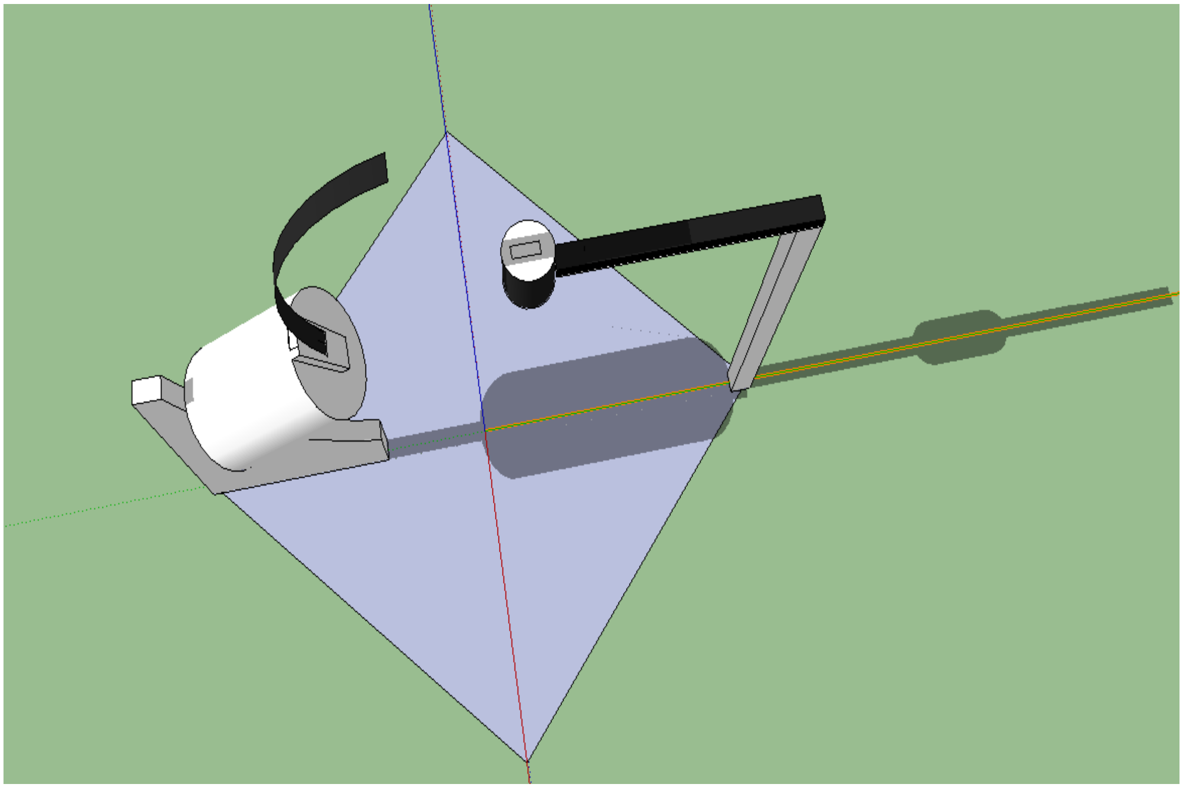

Figure 3.6: Horizontal Receiver in N-S direction at Solar Noon Time

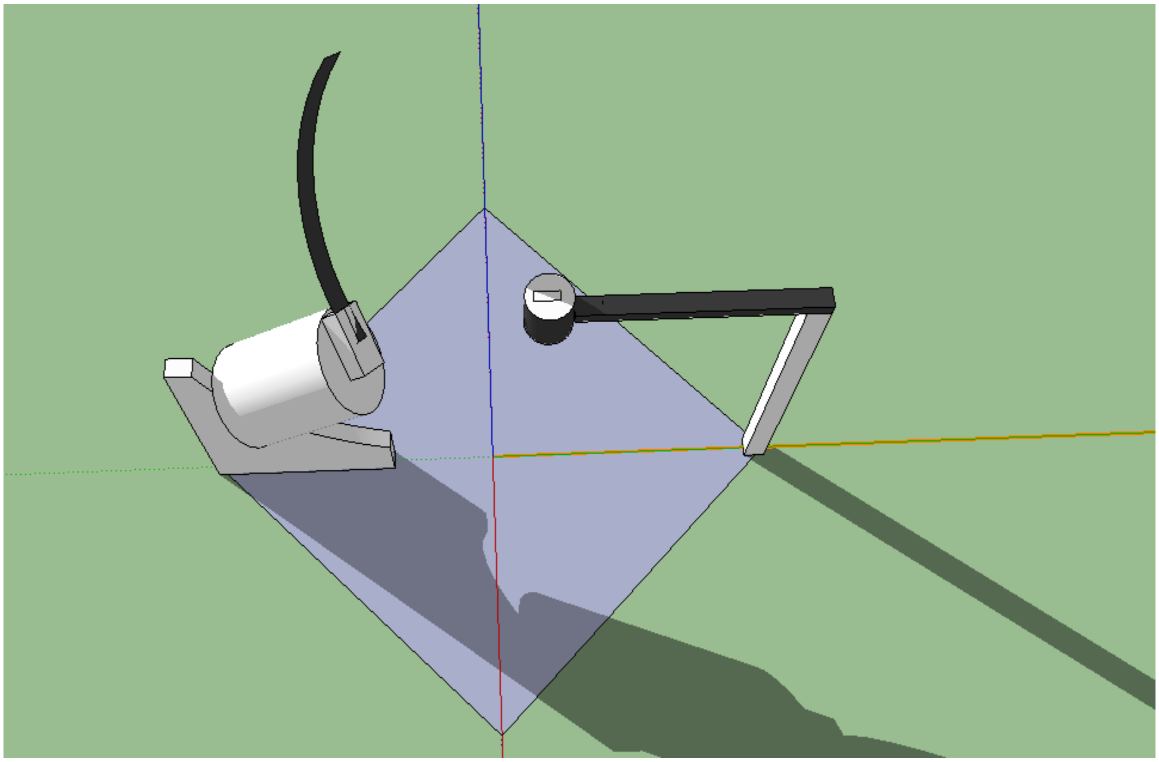

Figure 3.7: Horizontal Receiver in N-S direction at 14:30 in the afternoon

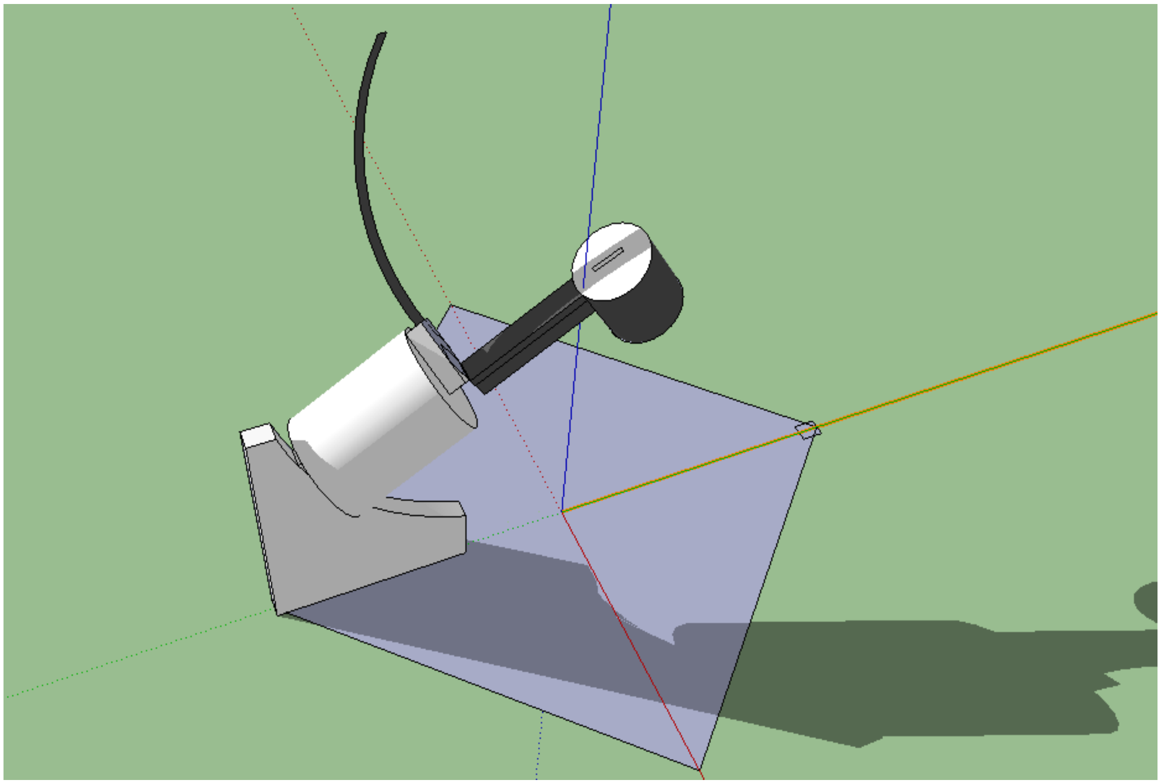

Figure 3.8: Titled Receiver on Polar Axis at 15:30 afternoon

Figure 3.9 shows the aluminum bracket that was fabricated and attached to the motor in order to hold the receiver on the polar axis.

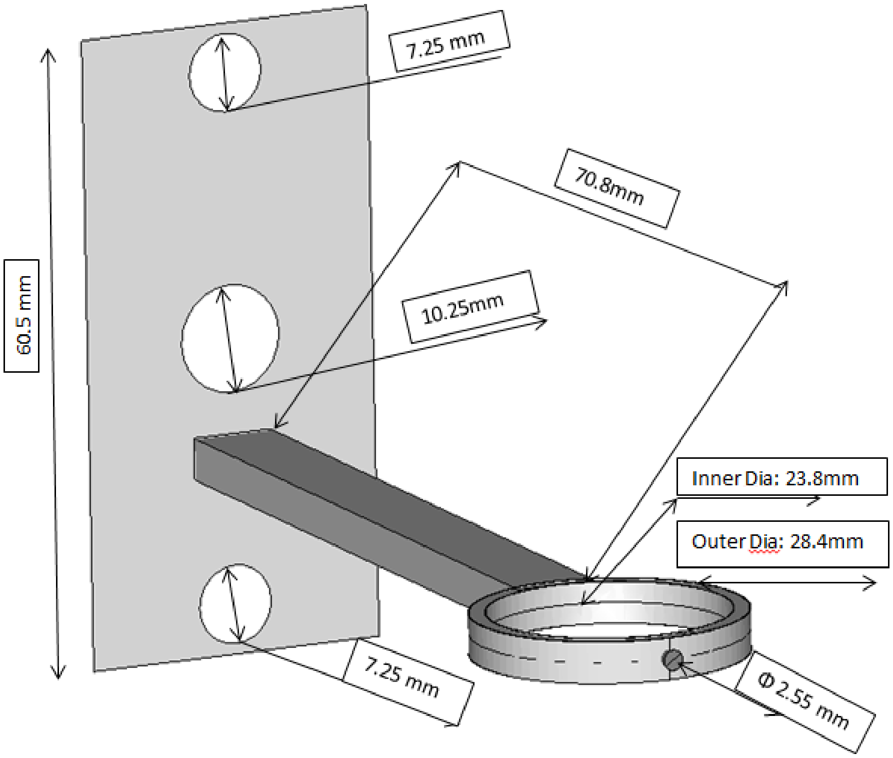

Figure 3.9: Fabricated Bracket to hold the receiver in the polar axis

3.4.2 Sensitivity of the CSR Retrieval with receiver Orientation

The SPI signal for a particular sweep forms a trough shaped trajectory with flat bottom when the shadowband covers the solar disk. The intensity falling on the receiver increases as the shadowband moves away from the solar disk region and becomes constant once the shadowband enters the isotropic sky region. The transition region from the solar disk to the sky region represents the circumsolar region and the circumsolar ratio (CSR) is influenced by the amount of rounding at the corners of the trough trajectory. This shows that SPI trajectories measured with the horizontal slit receiver are affected with the angular movement of the shadow during the day. Hence, the sensitivity of the flux profiles to gaussian noise in the SPI trajectories of the two receiver orientations has been tested. The purpose of sensitivity analysis is to compare the two types of SPI trajectories with the same magnitude of noise added. Gaussian noise of signal to noise ratio 30 with 1000 random numbers has been added to the intensity curve pertaining to a particular CSR for the axial and non- axial alignments of the receiver. Figure 3.10 shows the simulated sunshape trajectories of the SPI for the axial alignment of the receiver on the polar axis and the non-axial alignment using a horizontal receiver as in the case of a conventional RSI.

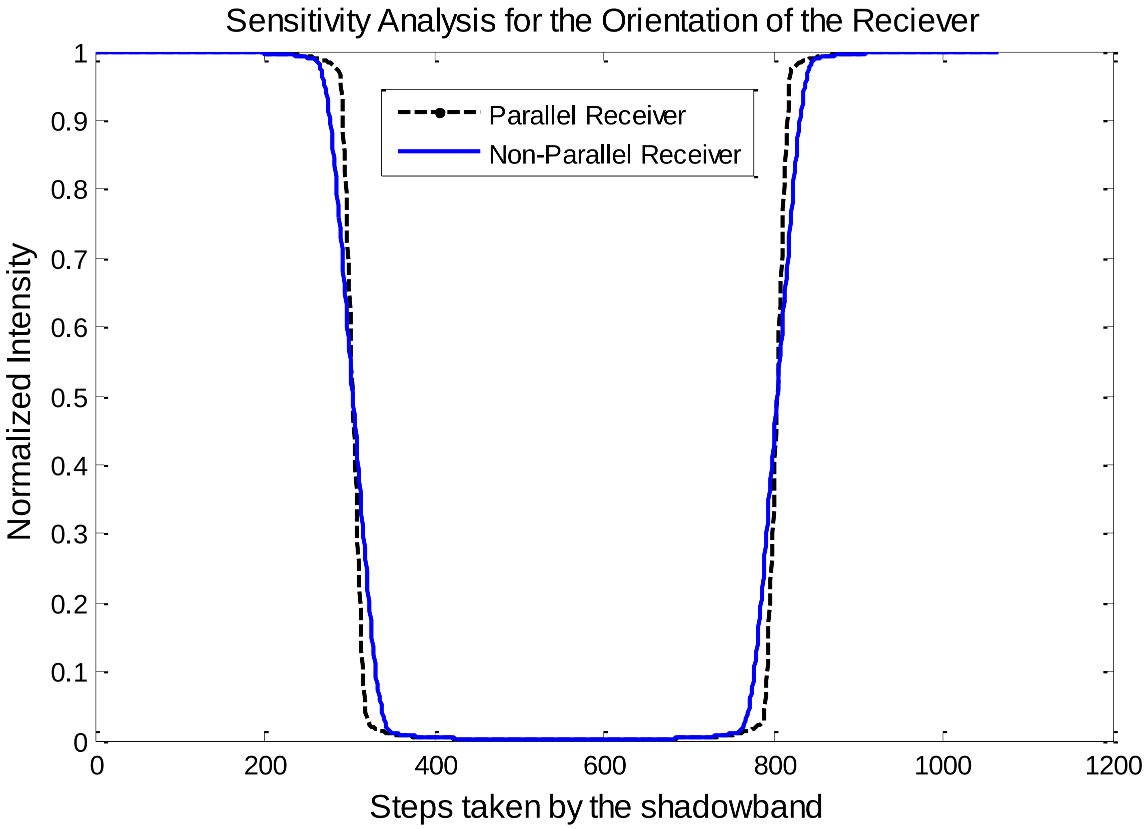

Figure 3.10: Sensitivity analysis of the simulated SPI trajectories for horizontal (non- axial) and tilted (axial) receiver orientations

In order to assess the sensitivity of the SPI signal to noise for both the cases, the statistical parameter that has been used is: Root Mean Squared deviation (RMSD), which indicates the deviation between the original and noisy signals given by equation 3.1:

$$\text{RMSD}=\sqrt{\frac{\sum_{i=1}^{N}\left(\left(SPI_{Signal}\right)_i-\left(SPI_{NoisySignal}\right)_i\right)^2}{N}} \tag{3.1}$$

where N is the number of total data analyzed. The obtained RMS deviation for perfectly aligned receiver has a mean of 0.0691and non-parallel receiver has a mean of 0.0717 for the same standard deviation of the applied Gaussian Noise. Hence, the perfectly aligned receiver position is observed to have a more stable flux profile that is less sensitive to the same noise added to each of them. This shows that accurate alignment of the receiver on the band motor (polar) axis is essential in order to obtain the sunshape profiles from the SPI. The alignment procedure for the SPI has been included in Appendix D.

CHAPTER 4

Inverse Model with Buie’s Sunshape

4.1 Buie’s Model for Circumsolar Ratio

D.C. Buie proposed an empirical circumsolar brightness model (Buie, 2004), which is dependent only on one variable, the circumsolar ratio (χ). It was observed from the LBL and DLR sunshape measurements (Figures 2.4, 2.5 and 2.7 from chapter 2) that the profile of the circumsolar region is almost linear in log- log space. This linear relationship between intensity and angular displacement is expressed as a power function by equation 4.1 (Buie, 2004):

$$\Phi(\theta) = \begin{cases} \cos(0.326\theta)/\cos(0.308\theta), \{0 < \theta < 4.65\mathrm{mrad}\} \\ e^{\kappa}\theta^{\Upsilon}, \{\theta > 4.65\mathrm{mrad}\} \end{cases} \tag{4.1}$$

Where γ is the gradient of the curve, given by:

$$\gamma = 2.2\ln(0.52\chi)\,\chi^{(0.43)} - 0.1 \tag{4.2}$$

κ is the intercept of that curve at an angular displacement of zero:

$$\kappa = 0.9\ln(13.5\chi)\,\chi^{(-0.3)} \tag{4.3}$$

A radial displacement of 4.65 mrad or 0.266^{o} for the solar disk has been taken into account in the above equations. The linear relationship between the intensity of the circumsolar region to that of the radial distribution in log- log space has been plotted based on Buie’s equations in Figure 4.1.

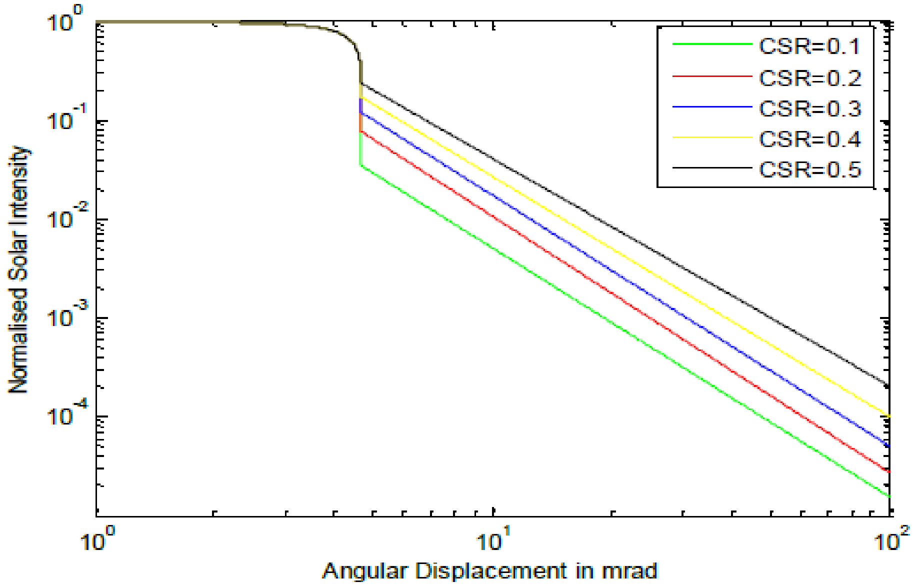

Figure 4.1: Angular distribution of solar radiation obtained from Buie's Model

4.2 Inverse Buie Model

The SPI trajectory is used to obtain the estimate of CSR with the help of an integration technique on Buie's equations from which the circumsolar ratio corresponding to the measured sunshape profile can be identified. A family of normalized simulated signals corresponding to different CSRs is generated by integrating Buie's equations. The CSR from the family of simulated signals that best matches the measured SPI trajectory is identified from the residuals of the simulated signals with respect to the measured signal using least squares. The CSR that gives the least RMS deviations is declared to be the CSR of the measured SPI trajectory. Figure 4.2 shows the family of simulated signals using an integration technique on Buie's equations and Figure 4.3 shows the RMS deviations plot of the family of simulated curves at different CSRs with respect to the measured SPI trajectory. A fine grid of CSRs from 0.05 to 0.17 in steps of 0.01 has been compared and evaluated with the measured trajectory from which CSR=0.12 shows the least deviation from the measured signal in Figure 4.3.

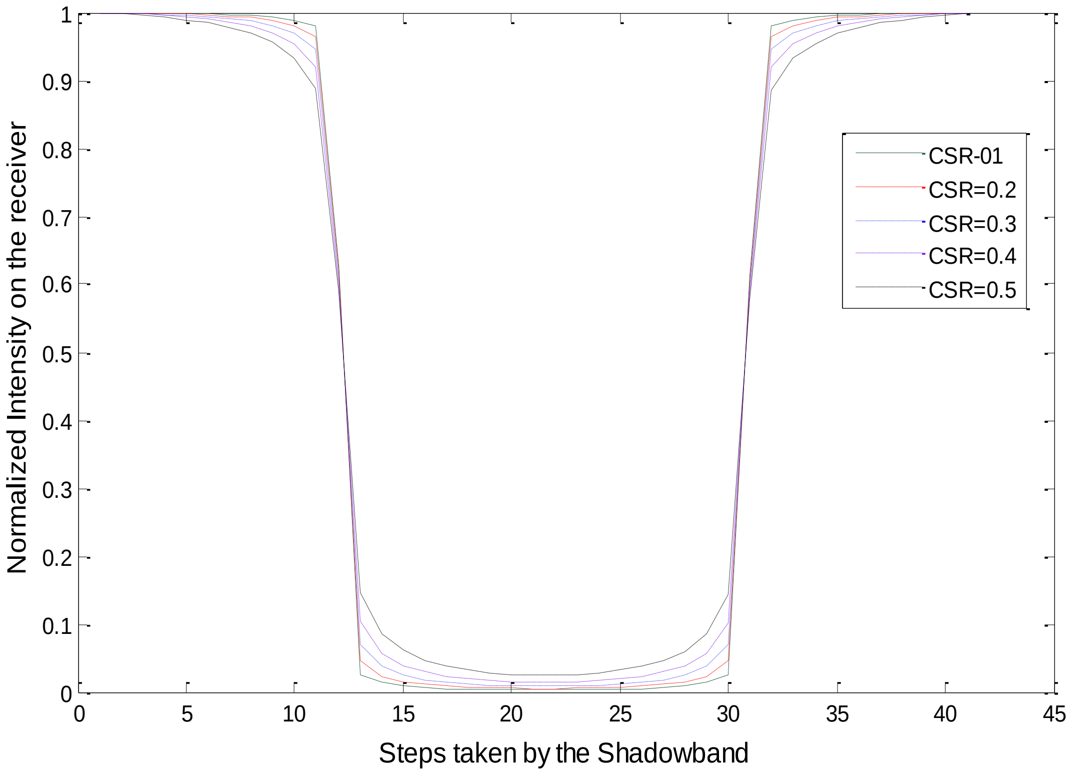

Figure 4.2: Family of simulated signals generated at different CSRs

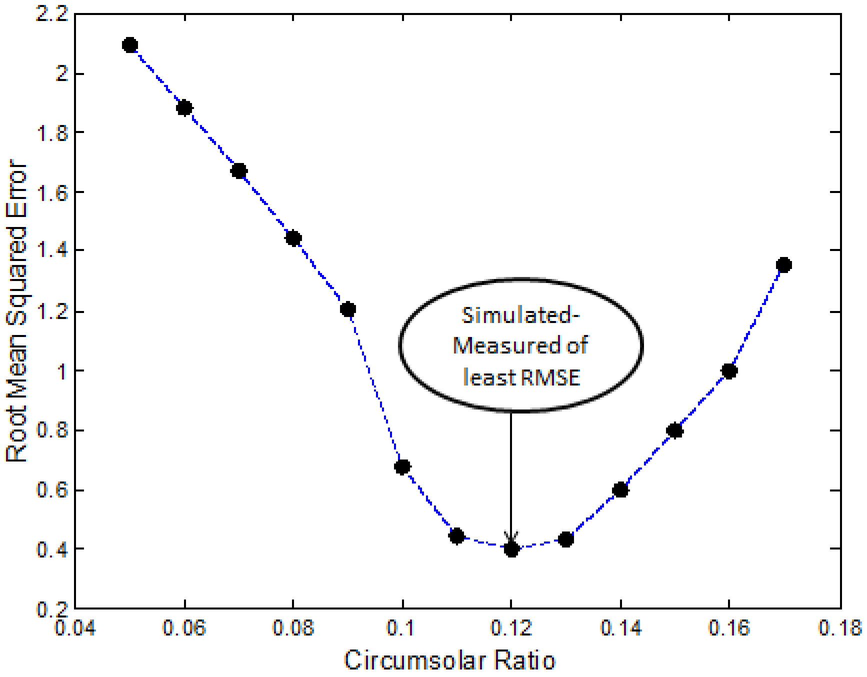

Figure 4.3: RMSE plot of the family of simulated signals with respect to measured SPI trajectory

4.2.1 Integration using Buie's Equations

Buie's equations produce the brightness profiles at the brightness points as function of the angular displacement of each point from the center of the solar disk. The arc of the shadowband covers a strip of the sky whose average brightness is determined by performing integration on a number of brightness points along the strip.

This integration over the circumsolar region is performed by assuming a rectangular patch of the sky containing the solar disk and the solar aureole (Figure 4.4). This rectangular area is divided into 4428 North-South (N-S) strips with the solar disk always at the center of the patch. The N-S length of the region covered by the shadowband has been assumed to be the same as that of the width of the chosen rectangle (α) = 150 mrad E-W. The length of the rectangle is equivalent to the arc swept by the shadowband in our practical testing, i.e. 322 mrad (18.45^{o}~ 41 half steps).

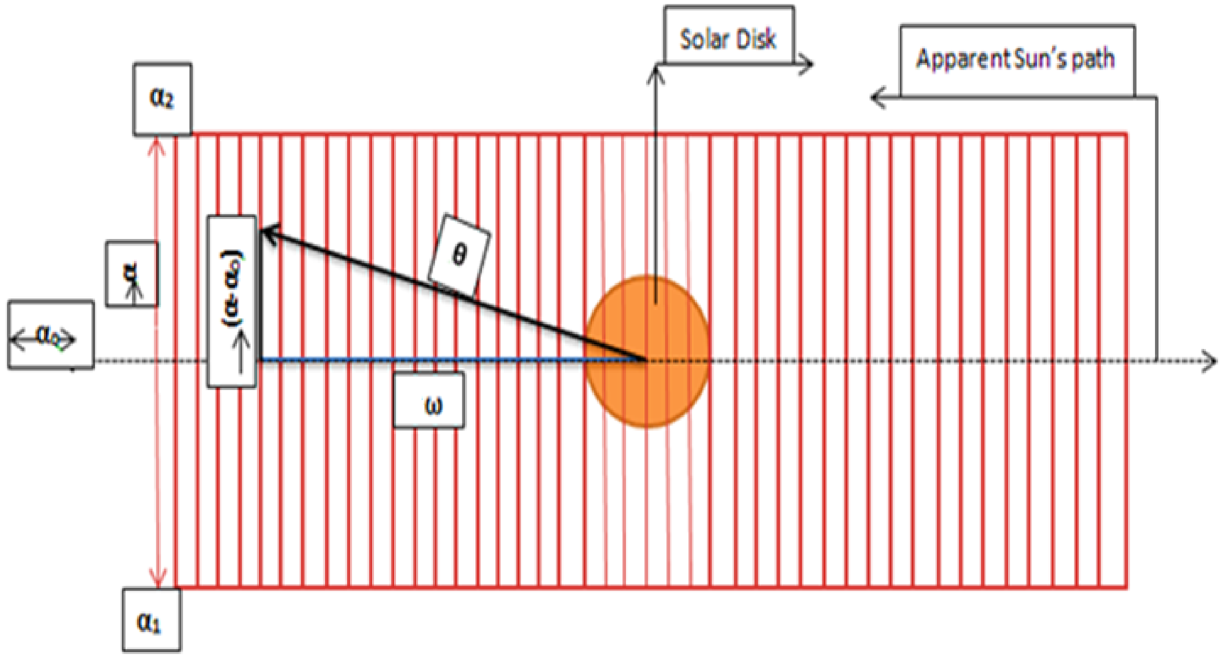

Figure 4.4: Pictorial representation of the strips around solar disk and circumsolar region (not to scale)

Each strip of the rectangle consists of 12000 points spanning α_1 to α_2. At any point on any strip, the angular displacement can be calculated by approximating the patch of sky as a planar rectangle using Pythagoras theorem. ω is the perpendicular distance to the position of the shadowband from the center of the solar disk. The distance of each point on a line from the center line of the strip is equal to 'α-α_o'. Hence, the angular displacement of every point from the center of the disk can be calculated as:

$$\theta = \sqrt{(\alpha - \alpha_o)^2 + \omega^2} \tag{4.4}$$

Intensity from a given strip is equal to the summation of intensities at every point on the strip. Hence, the angular displacement θ of the Buie's Equation (4.1) is replaced by the calculated θ from equation 4.4, which gives the Intensity of the rectangular region as viewed from a point receiver as given in equation 4.5:

$$I_\omega = \int_{\alpha 1}^{\alpha 2} Buie(\omega, \alpha, \chi) d\alpha = 2 \int_{\alpha_o}^{\alpha_2} Buie(\omega, (\alpha - \alpha_0), \chi) d\alpha \tag{4.5}$$

The width of the shadowband has been measured to subtend 148.35 mrad (or 8.5°) at the center of the diffuser which is equivalent to 1950 strips of the rectangle.

Hence, the measured intensity on a point receiver is equivalent to the intensity corresponding to the strips of the rectangular patch that are blocked by the shadowband during its traverse subtracted from the total intensity contributed by all the strips in the rectangular patch (obtained by changing ω from 1 to 4428) as described by equation 4.6:

$$I_{measured}(j) = \xi_0 + \xi_1 \left\{ \sum_{\omega=1}^{4428} I_\omega - \sum_{i=j-n}^{j+n} I_\omega \right\} \tag{4.6}$$

j is the step taken by the shadowband, n is the half width of the shadowband arc projected on the rectangular patch, ξ_0 and ξ_1 are the obtained coefficients from least squares.

In case of a receiver with finite width in reality, the view factor from one edge of the receiver is different from the other. Hence, a weight function (Figure 4.5) to accommodate for the width of the slit receiver has been considered to obtain more realistic simulated trajectories.

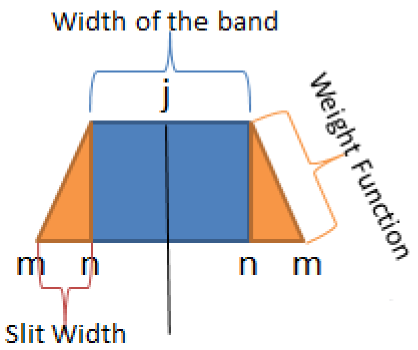

Figure 4.5: Weight Function for the finite width of the slit receiver

In this case, the indices j and n are the same as those used in the equation for point receiver. However, m represents the width of the slit receiver whose weight is added during the entry and exit of the shadowband on the receiver aperture during its sweep as shown in equation 4.7:

$$I_{measured}(j) = \xi_0 + \xi_1\{\sum_{\omega=1}^{4428} I_\omega - \sum_{i=j-n-m}^{j-n} \frac{i-n-m}{m} I_\omega - \sum_{i=j-n}^{j+n} I_\omega - \sum_{i=j+n}^{j+n+m} \frac{i-n}{m} I_\omega\} \tag{4.7}$$

4.3 Least Squares Coefficient ξ_0

The measured normalized SPI signal at every step of the shadowband ($I_{measured}(j)$) is compared with each of the simulated SPI signals from the family of normalized curves generated by the integration technique described in section 4.2. The estimate of CSR is obtained from the residuals of the measured SPI trajectory and the simulated SPI signals. Coefficients ξ_o and ξ_1 are estimated by ordinary least squares for each simulated SPI signal. ξ_o represents the diffuse radiation of the sky region outside the rectangular patch that falls on the receiver and a portion of ground reflected radiation that also falls on the tilted receiver.

Figure 4.6 shows the offset (ξ_o) between the measured SPI trajectory and the simulated signal pertaining to a particular CSR. This offset is due to the diffuse radiation on the receiver which has not been taken into account in the simulation.

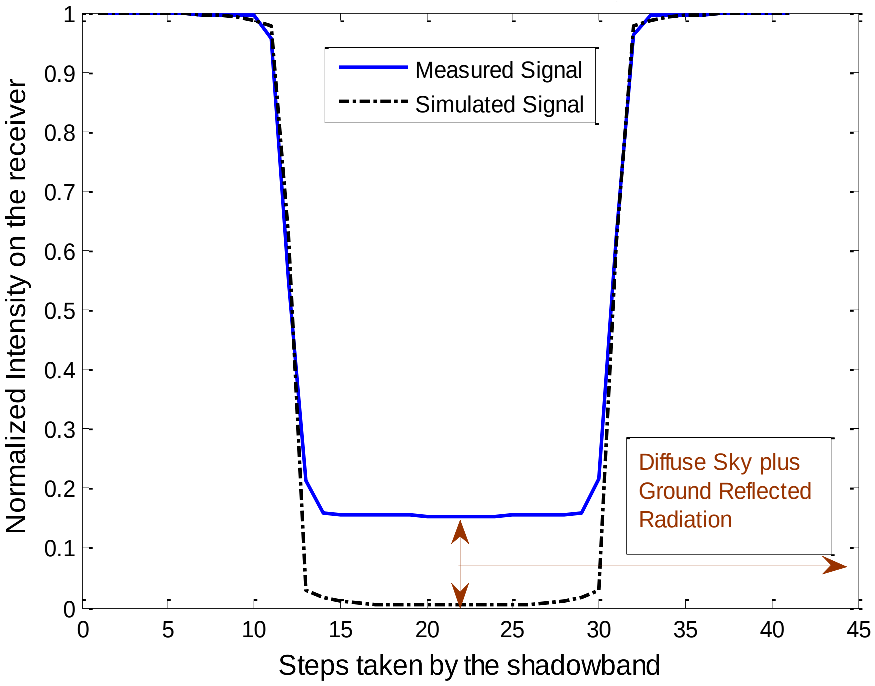

Figure 4.6: Measured and Simulated SPI Trajectories

4.4 Sweep Symmetry

As discussed in Chapter 3, the SPI makes 26 sweeps with 41 motor steps in each sweep within a time span of two minutes and then returns to its home position. The time difference between one sweep to another is set to be 4 seconds during which the sun moves by an angle of 0.0167°. Each sweep results in a trough like trajectory whose symmetry varies with the center position of the solar disk. In order to perform the inverse model on the trajectory of the SPI receiver's signal, the most symmetric two curves are picked out of the 26 different curves obtained from the 26 sweeps. If y_i represents the measured signal containing 41 points, then the most symmetric sweep is determined by obtaining the RMSE between the intensity values at 20 steps to the left and 20 steps to the right of the middle step of the SPI trajectory at step 21. For the bottom portion of the trough, 9 points on either side of the middle step are considered to test the symmetry with equation 4.8:

$$Minimum \left\{ \sqrt{\frac{\sum_{i=1}^{9}(y_{I+i}-y_{I-i})^2}{9}} \right\} \tag{4.8}$$

Where I is 21 (middle step out of 21 steps) and the trajectory that gives the least RMSE is taken as the most symmetric sweep. A combination of two symmetric sweeps is considered in order to increase the data points on the trough trajectory such that the most symmetric sweep is separated by the other sweep by 0.225^o. Figure 4.7 illustrates a symmetric sweep of the SPI signal.

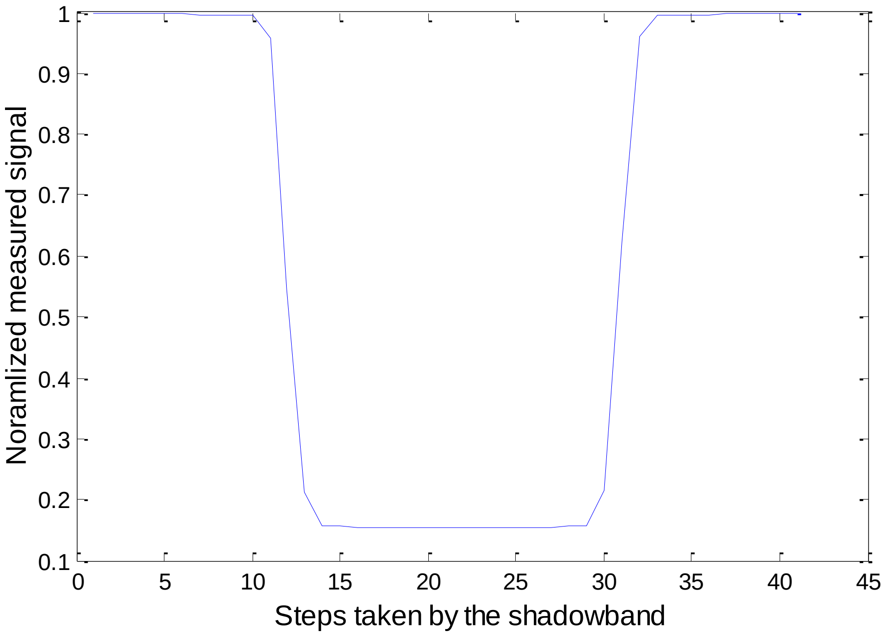

Figure 4.7: Measured SPI Signal of a symmetric Sweep on Feb-27 at 12:02pm

The sensitivity of the sweep symmetry is tested and numerically analyzed. It is observed that for a particular scan time of 2 minutes, the most symmetric sweep gives the estimate of CSR with least Mean Squared Error (MSE) from the family of CSR curves generated with the inverse Buie Model. It is also observed that the difference in the CSR estimates from the least symmetric to the most symmetric sweeps is equivalent to 0.02 in Figure 4.8. This can be due to the motion of the sun during the sweeps of the shadowband.

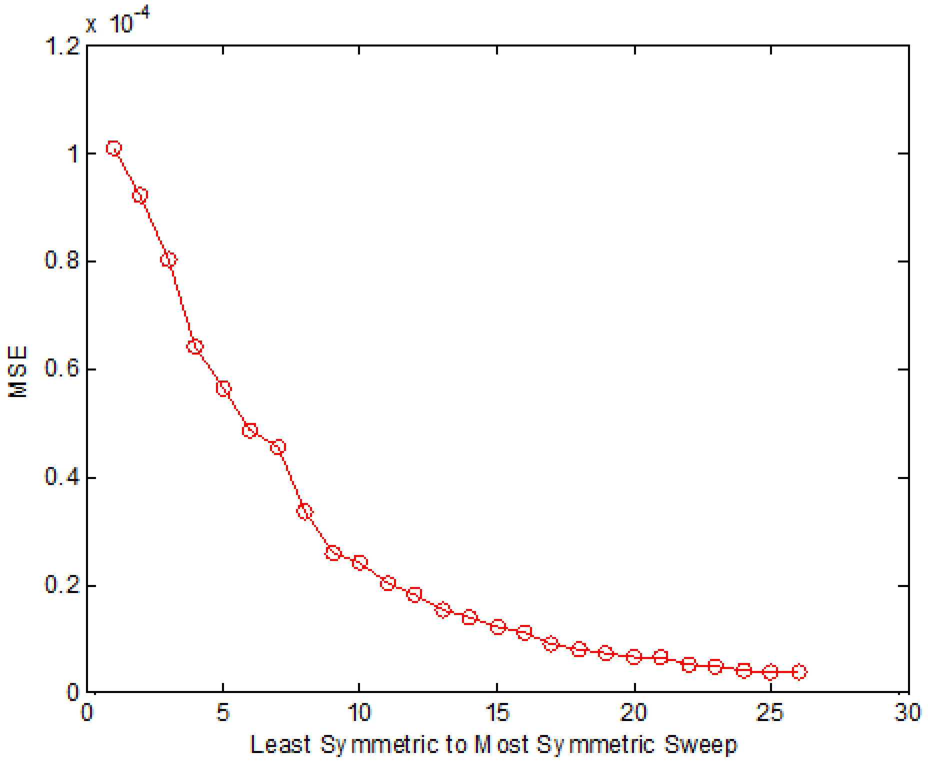

Figure 4.8: Sensitivity of the Sweep Symmetry

The initial idea was to combine all the measured signals corresponding to the 26 sweeps into one signal trajectory with 1066 steps all together to get high resolution data, but due to the signal noise and changing of sky conditions, smooth trajectories could not be obtained for all times of the day. The signal noise could also possibly due to alignment and vibration errors. On clear sky days, the combined signal resulted in smooth distribution of steps from all the 26 sweeps. Figure

4.9 illustrates the SPI signal after combining all the signals from 26 sweeps for smooth combination as well as combined signal of the sweeps with noise. Under hazy or unclear conditions, the combination of the sweeps results in noisy signal trajectories due to which accurate CSR estimates cannot be obtained from least squares. The signal noise is observed at the bottom of the trough and more on the outside the umbral region with the combined signal of 26 sweeps on unclear days as shown by the black trace in Figure 4.9. Hence, the inverse model is performed only on two symmetric sweeps out of the 26 sweeps and not on the combined trajectory of all the 26 sweeps.

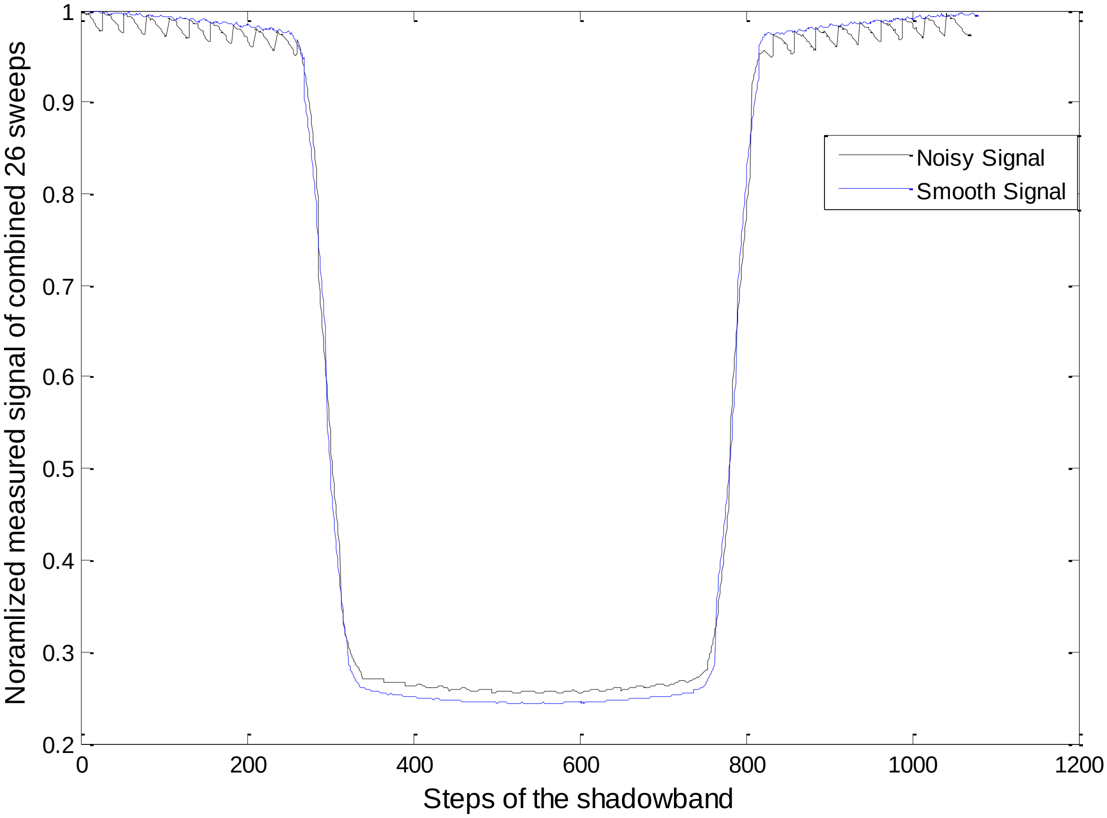

Figure 4.9: Combination of all sweeps of the SPI

Figure 4.10 illustrates the CSR estimates obtained from a single symmetric sweep and a combination of two symmetric sweeps that are 0.225^{o} step angle apart. The signal noise increases slightly for the combined signal but more data points result in a better least squares estimate. Hence, the CSR estimates are sometimes different with single and combined sweep trajectories. More investigation is needed on analyzing the reason behind the signal noise and further modification is required to reduce the signal noise. For example, one can use 16- bit instead of 12- bit analog to digital converter (see Appendix C).

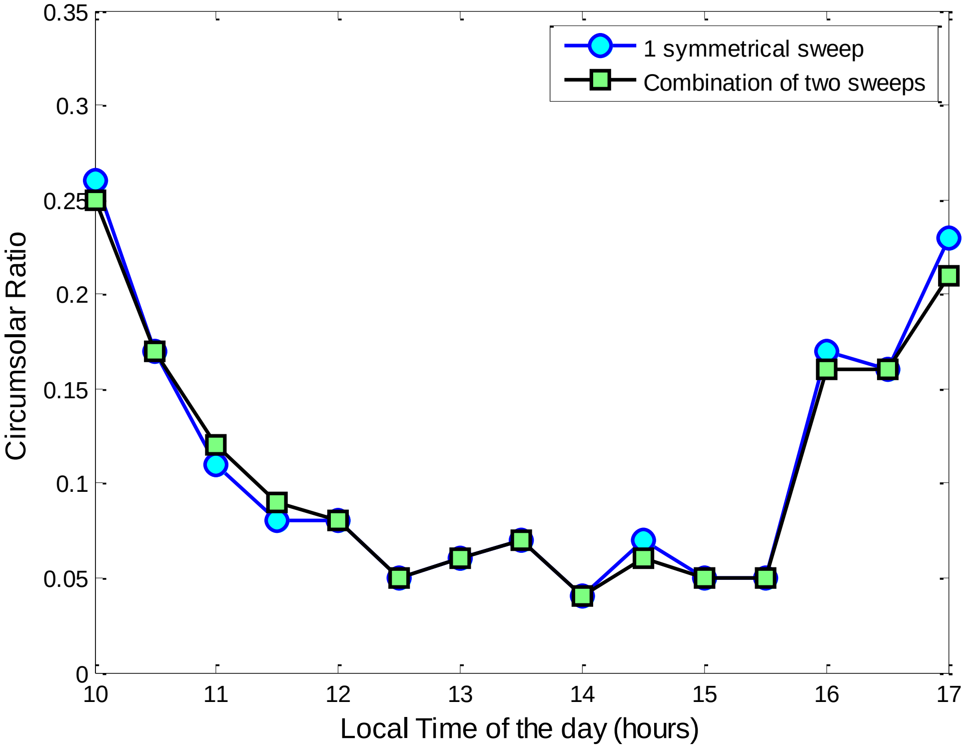

Figure 4.10: CSR for one sweep and combination of two sweeps

4.5 Estimated CSRs with time of the day

Applying the above described inverse Buie model to the measured SPI trajectories from the 12th of February to the 2nd of March, 2012; the circumsolar ratios under different atmospheric conditions have been estimated. On clear days, the circumsolar ratio is observed to decrease relatively during the noon time as compared to that in the morning and evening hours. Figure

4.11 shows the predicted results of the Circumsolar Ratio Vs. the time of the day with the inverse model using the SPI trajectories after every 10 minutes of interval and using a coarse grid of the CSR values from 0.1 to 0.35 for the simulated signals. The sky condition on the 23rd of February 2012 was clear (less hazy) with the peak DNI = 779 W/m^2. The CSR varies from 0.35 at 10 am to 0.1 during noon and 0.25 in the evening at 4 pm.

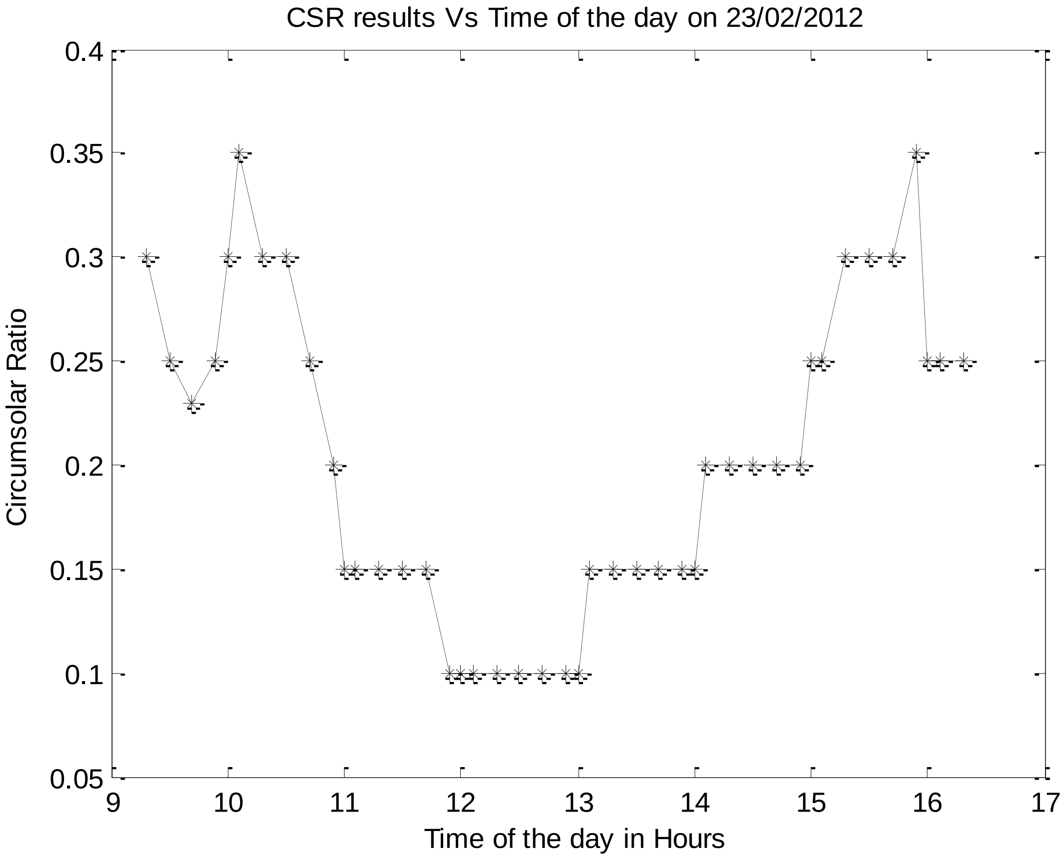

Figure 4.11: Predicted CSR values Vs Time on Feb-23, a clear Day

The sky condition on the 27th of February 2012 was observed to be very clear with almost no haze or dust. The predicted CSRs are found to be very low as compared to other days of the usual Abu Dhabi weather conditions. The CSR is estimated by least squares to be low below 10% during high DNI ranging from 750- 854 W/m^2. Figure 4.12 illustrates the variation of the

CSR with time of the day (every ten minutes) under very clear sky conditions. The results are in agreement with literature by Neumann et al. (2002); that says the CSR on clear blue sky conditions is almost constant over the day and lower than 5%.

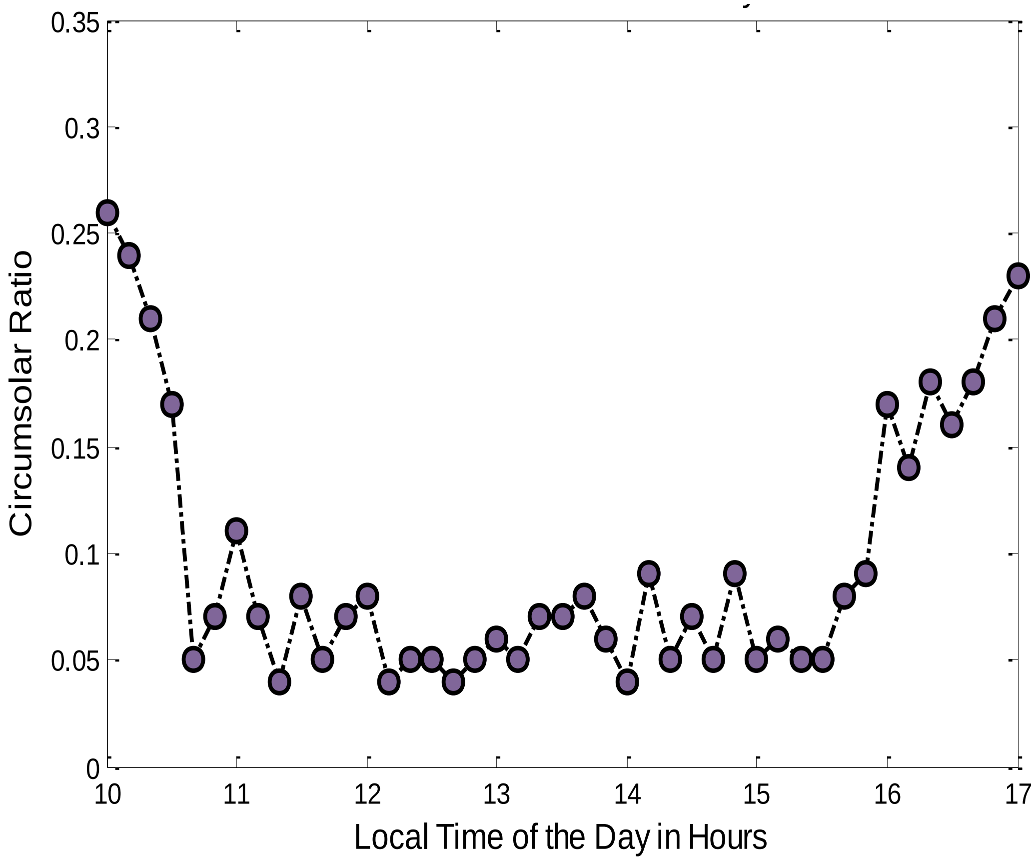

Figure 4.12: Predicted CSR values Vs Time onFeb-27 under clear blue conditions

However, no clear trend of CSRs is observed on unclear and hazy days that are typical to Abu Dhabi's climate. Figure 4.13 illustrates the variation of CSR with time on a dusty, unclear day on March -01 when high values of circumsolar ratios (almost 0.6) are estimated from the inverse Buie model. The peak DNI attained on the 1st of March is 451W/m^2 which explains the reason behind the high CSR values. The aerosol optical thickness may be expected to be high on a dusty day, which also contributes to the large amount of forward scattered radiation at the circumsolar region leading to high values of CSRs.

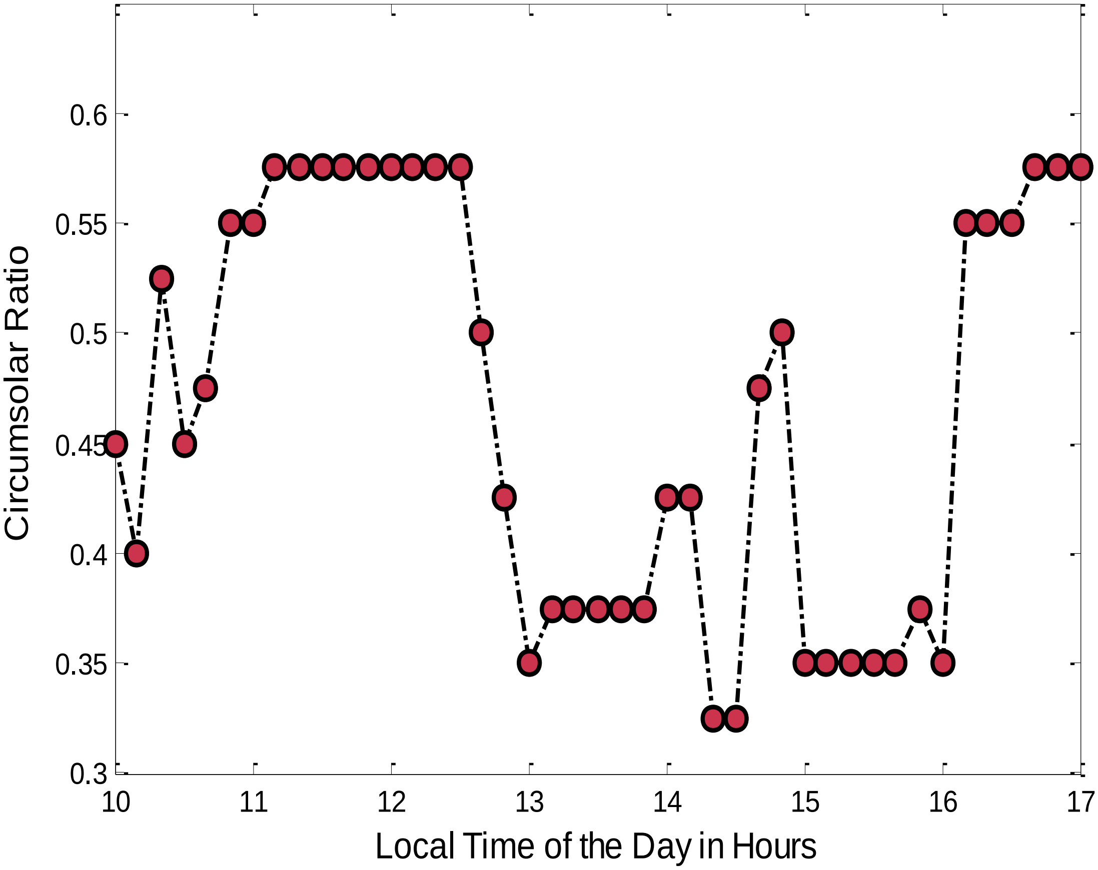

Figure 4.13: Predicted CSR values under unclear, dusty day on Mar-01

It is important to note that the Buie's equations are applicable only for clear sky conditions and the half- angular extent of the sun aureole is taken as only 43.6 mrad (or 2.5^{o}). Under dusty conditions when the CSR reaches up to almost 60%, the angular extent of the aureole can also be expected to be much higher than the limit assumed by Buie. Hence, the integration procedure with Buie's model is observed to work well only for clear sky conditions and not for dusty days that are typical to Abu Dhabi's climate.

4.5.1 Variation of CSR with Air Mass

The air mass (m) is defined as "*the ratio of the mass of atmosphere through which beam radiation passes to the mass it would pass through if the sun were at the zenith*" in (Duffie & Beckman, 2006, Third Edition) and m is calculated assuming negligible refraction of the beam[1]:

$$m = \frac{1}{cos\theta_z} \tag{4.9}$$

On clear days, the CSR is expected to increase with increase in air mass, because air mass is the least during the solar noon and increases with increase in zenith angle and higher air mass results in more forward scattering of the beam. However, on unclear, dusty days, no clear trend of the CSR variation with air mass is expected as observed from Figure 4.13, the CSR randomly changes with time of the day. Figure 4.14 shows the clear trend in the variation of estimated CSRs with the air mass on a clear day- Feb27.

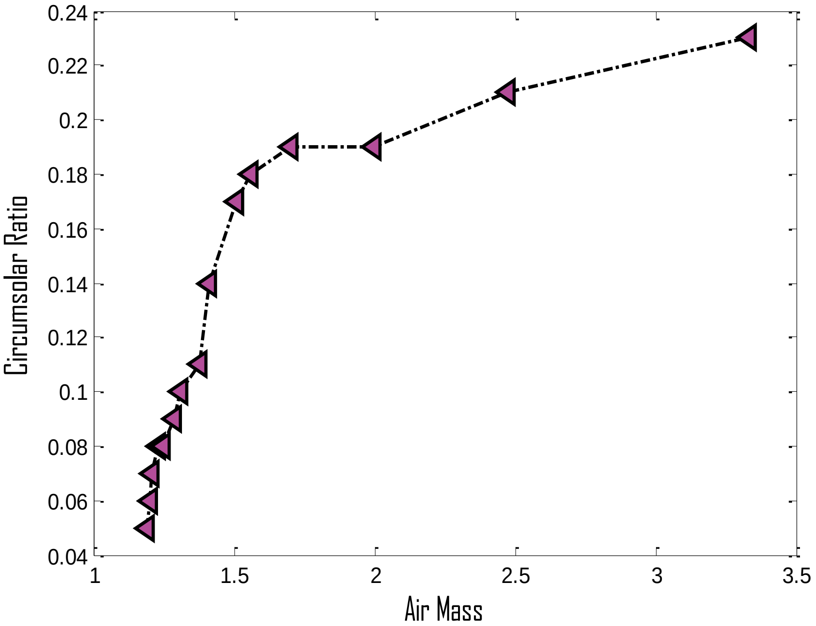

Figure 4.14: Predicted Circumsolar Ratios with varying Air Mass on Feb-27

---

[1] (Kasten & Young, 1989) accounts for refraction as: $m = \frac{\exp(-0.0001184h)}{\cos(\theta_z)+0.05057(96.080-\theta_z)^{-1.634}}$

4.5.2 Variation of CSRs with DNI

The CSRs obtained on Feb-27 are compared with the DNI of the day in Figure 4.15. Previous LBL works showing the CSR dependence solely on DNI, approximated by a polynomial function has been discussed by (Neumann, von der Au, & Heller, 1998). Further correlation studies at the DLR stated that the CSR does not depend on the DNI in a simple monotonic way (Neumann, von der Au, & Heller, 1998). However, it is observed that the instantaneous samples of CSRs increase with decrease in DNI and vice versa on any given clear day.

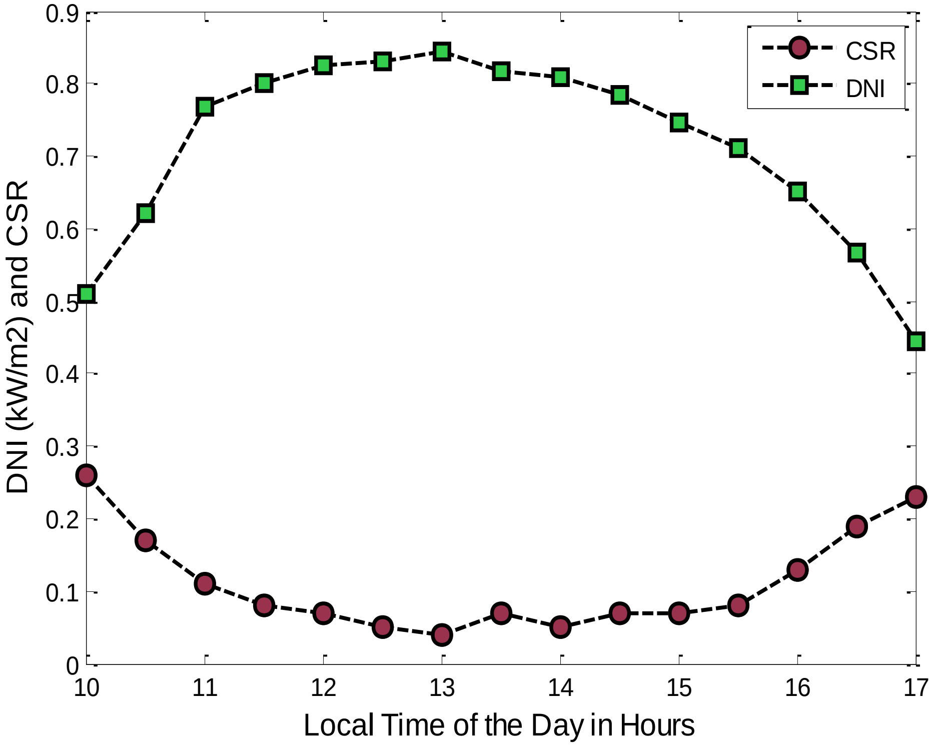

Figure 4.15: DNI and CSR on Feb-27, a clear day

4.6 Obtained Least Squares Coefficients

As discussed in section 4.3, two coefficients ξ_o and ξ_1 are obtained from least squares such that ξ_o is proportional to the Diffuse Horizontal Radiation received from outside the rectangular patch considered for the Buie's Sunshape. A part of ground reflected radiation is also included in this coefficient since the receiver is tilted to the polar axis. Hence, ξ_o is expected to be lower than the total diffuse irradiation on a horizontal receiver except in rare cases where there is a large reflected component from the bit of ground to which the south-tilted receiver of the SPI is exposed. Figure 4.16 shows the two least squares coefficients at different times during the day on Feb-27 (a clear day).

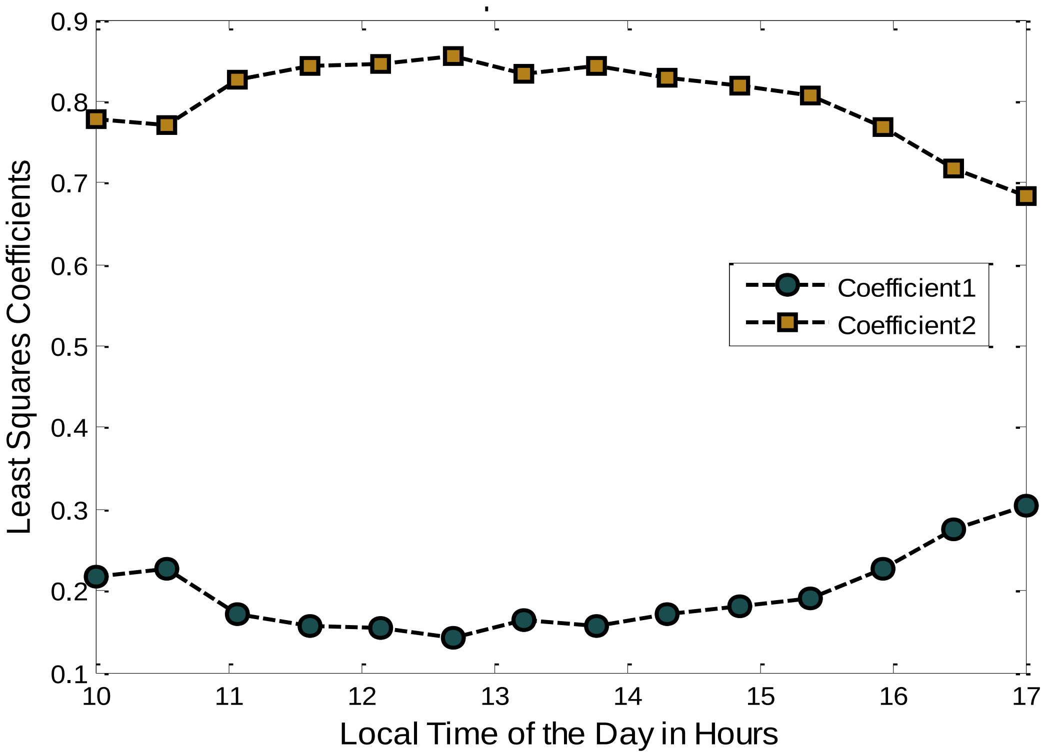

Figure 4.16: Least Square Coefficients ξ_o and ξ_1 with time on a clear

The two least squares coefficients from Figure 4.16 are observed to add up closed to 1. This indicates that if ξ_o is proportional to the diffuse radiation then ξ_1 could be proportional to the cosine-corrected DNI plus the diffuse irradiation from within the rectangular patch in which Buie's sunshape is assumed. Hence, it is expected to be always more than the measured DNI because the patch is larger (in terms of solid angle) than the solid angle subtended by the traditional DNI measuring instruments.

In order to confirm our prediction of the relation of the two least squares coefficients to the measured DHI and cosine- corrected DNI, the ratios of the measured $\frac{DHI}{GHI}$ and $\frac{DNI\ cos\theta_z}{GHI}$ on the 27th of Feb have been plotted along with ξ_o and ξ_1 for the same day. Coefficient 1 of least squares in Figure 4.17 represents ξ_o which is observed to be lower than the measured $\frac{DHI}{GHI}$ through out the day as predicted. Also, ξ_1 which is labelled as Coefficient 2 in Figure 4.17, is observed to be always higher than the measured $\frac{DNI\ cos\theta_z}{GHI}$ because of the larger solid angle of the rectangular patch as opposed to that of the DNI measuring isntrument. This defines the limited potential of the SPI to also work as a conventional RSI apart from its main function of measuring the sunshapes.. A direct inverse model is proposed in chapter 6 which would give a truer estimate of the measured DNI and DHI for any location and time of the day.

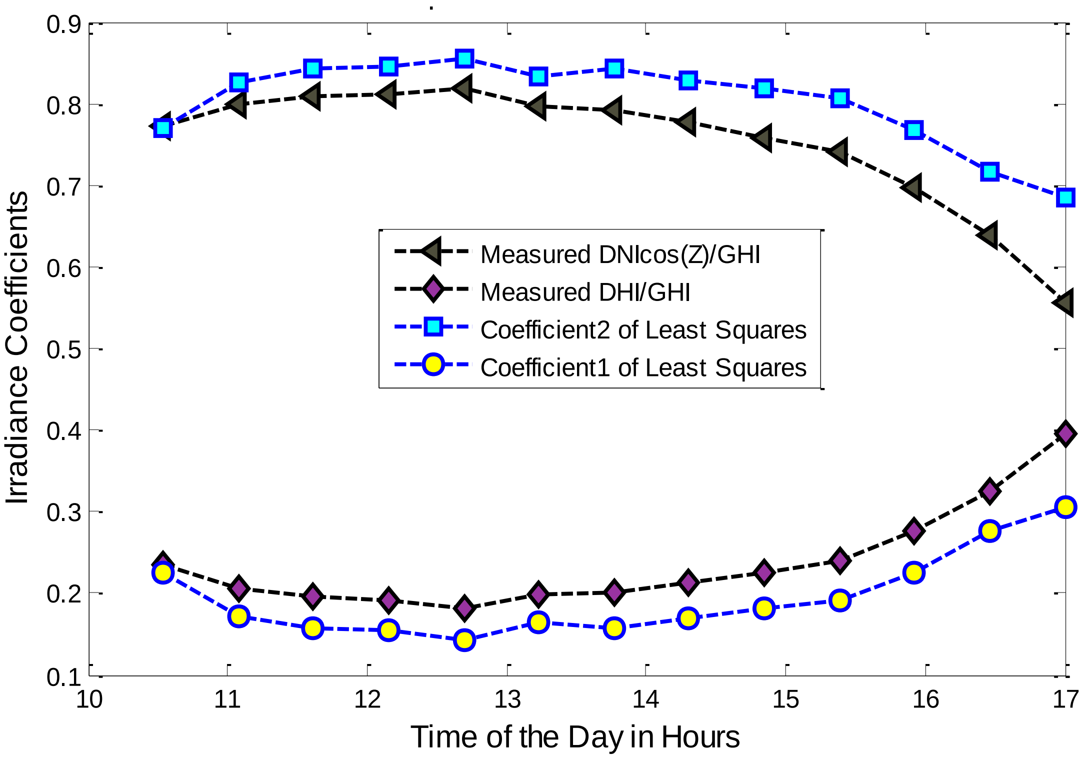

Figure 4.17: Least Squares Coefficients and the measured components of Solar Irradiance.

It is important to note that the normalizing factor for the SPI is not exactly the Global Horizontal Irradiance (GHI); rather it is GHI minus irradiation from bit of north sky not visible to the receiver plus radiation reflected from the bit of south ground that is visible. The ground reflected part includes both DNI and DHI components and can be addressed by standard models for tilted collectors such as the isotropic diffuse model given by (Liu & Jordan, 1963).

4.7 Impact of CSR on the Intercept Factor of Parabolic Troughs

The impact of varying CSRs with time of the day and location on the radiation intercepted by the receiver of a CSP plant with parabolic troughs has been analyzed using an optical model described by (Bendt, Rabl, Gaul, & Reed, 1979). Dimensions and design of the collector and receiver have been taken from Euro Troughs standards (Geyer, et al., 2002). In this model, the sunshape error has been convolved with the optical and surface errors of the collectors. The methodology is described in Appendix E. The intercept factors of the parabolic troughs have been evaluated with the CSRs of a) clear blue sky day (Feb-27) and b) dusty day (Mar-01) as shown in Figure 4.18. It is observed that the intercept factor on a clear sky day is more than 95% for the whole day and it is equivalent to more than 97% during solar noon. This shows that the efficiency and hence, power output of the CSP plant under low CSR conditions would be high. On a dusty day, however, the intercept factor is observed to decrease considerably to a maximum of 92% after noon. For the high CSR day during morning hours, the intercept factor has reduced to 83%. This indicates that the impact of circumsolar radiation in regions with high concentrations of aerosols, dust, and relative humidity like UAE is important for determining the true solar to thermal efficiency and power output of a concentrating solar system. The acceptance angle of a receiver in a solar concentrating system is much lower than that of a DNI measuring instrument. Hence, the angular distribution of solar radiation plays a vital role in determining the optimal receiver aperture and acceptance angle for a given plant and site, which when not considered results in an overestimation of the power output due to the large acceptance angles of the DNI measuring instruments. Every 1% percent drop in efficiency results in huge losses for the investors. On dusty days, with drop in intercept factor by more than 5%; the investment losses can be expected to be even higher. For higher concentrating facilities like central towers, parabolic dishes etc. the impact of the circumsolar radiation on the radiation intercepted by the receiver would be more than that in parabolic troughs. This is because the maximum theoretical concentration for point focus concentrators is inversely related to the square of half acceptance angle as mentioned in equation 1.1.

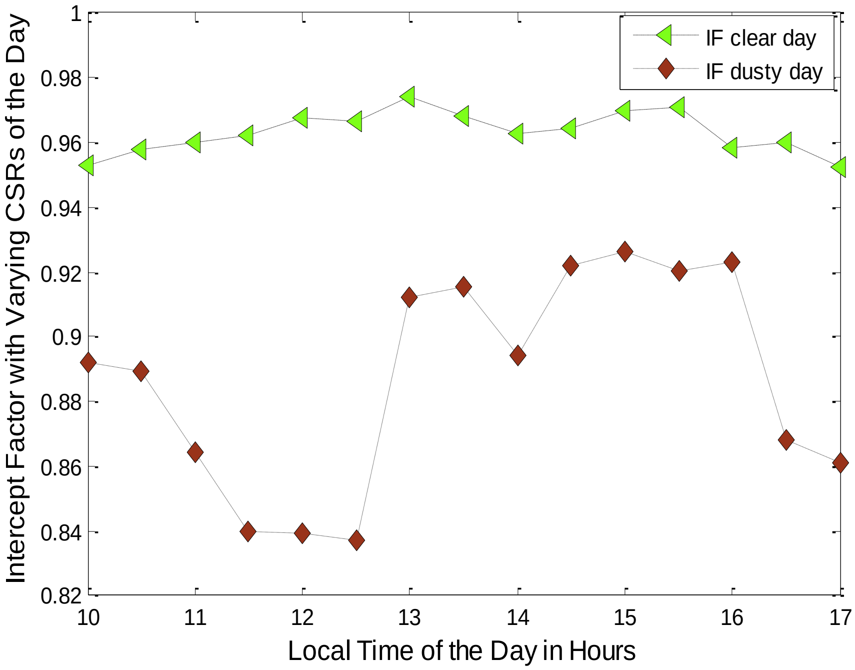

Figure 4.18: Intercept Factor of Parabolic Troughs as function of CSR and time, Feb-27 and Mar-1, 2012

Hence, the CSR is an important parameter for improved solar resource assessment that should be taken into account in the optical models of concentrating solar technologies.

CHAPTER 5

SAM Data and Validation

The Sun and Aureole Measurement System (SAM) captures the images of the solar disk and aureole up to a large half acceptance angle of 9.9^{o} using calibrated CCD cameras, as mentioned in chapter 2. It is a very expensive instrument and too sensitive for general met-station deployment. However, as a research instrument it provides accurate and high resolution brightness maps that are useful for calibrating the SPI. Figure 5.1 shows the SAM and other sensors on the radiometer platform at Masdar.

Figure 5.1: SAM and other sensors on the Radiometer Platform at Masdar

The CSRs obtained by the inverse model from the SPI measurements are compared with the broadband CSRs estimated from the aureole profiles by the Sun and Aureole Measurement System (SAM) at the same location and under same atmospheric conditions on the radiometer platform at Masdar. The images captured by the cameras in SAM are then processed with the help of auto_gui processor to convert the images taken by the camera into 2-D plots of optical depth, spectral radiance, vertical, horizontal and radial irradiance profiles of the aureole. The inbuilt program in the SAM system creates graphical displays of the output parameters. The 2-D plots generated by the software are post processed to obtain the broadband CSR, using the equations discussed in chapter 2. The post processing for the CSR estimates has been performed with the help of a model derived by Stefan Wilbert, DLR, PSA, Spain (Wilbert, et al., 2011).

5.1 Aureole Profiles generated by the SAM

The SAM produces radial, vertical and horizontal profiles of the sun aureole along with varying optical depth with time of the day and spectrum at wavelengths from 400 to 1000 nm for a particular day (Feb-12) as shown in Figures 5.2, 5.3, 5.4, 5.5, and 5.6.

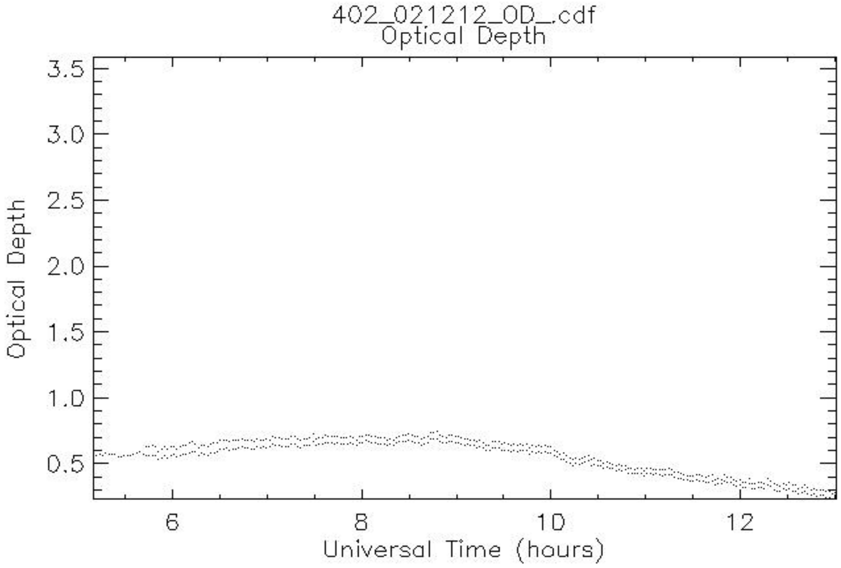

Figure 5.2: Optical Depth from SAM on 12/02/2012

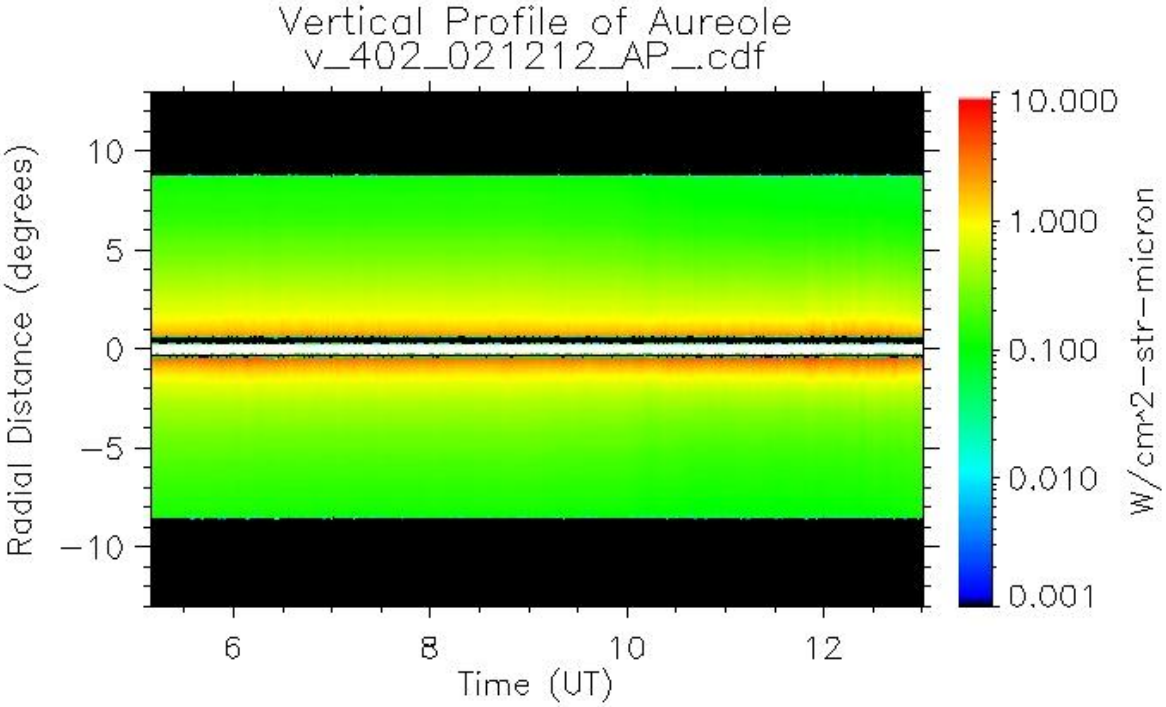

Figure 5.3: Vertical Aureole Profile

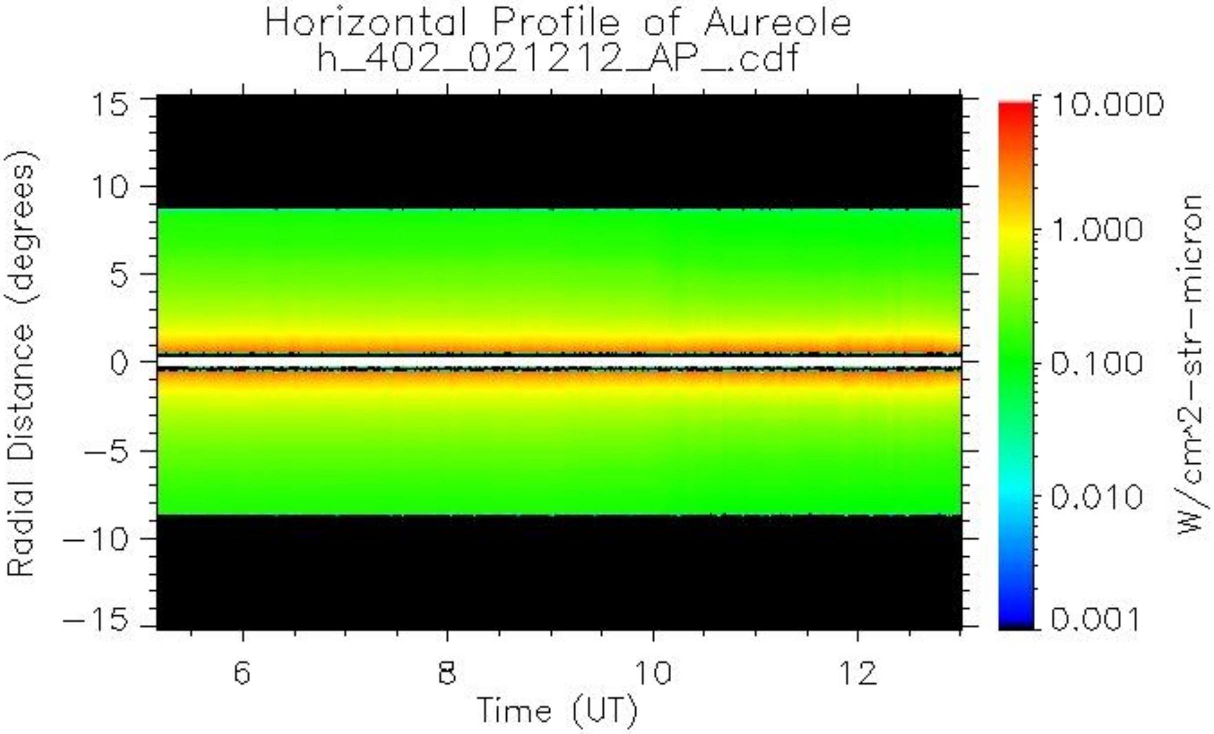

Figure 5.4: Horizontal Aureole Profile

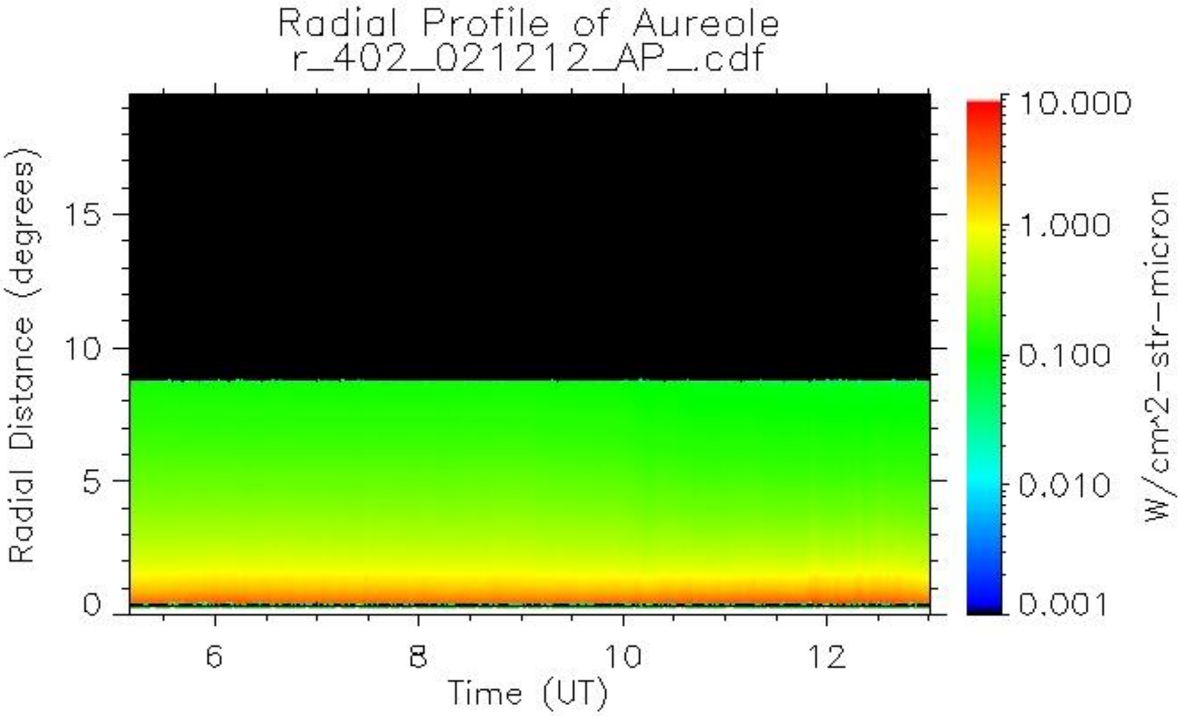

Figure 5.5: Radial Profile of the Aureole

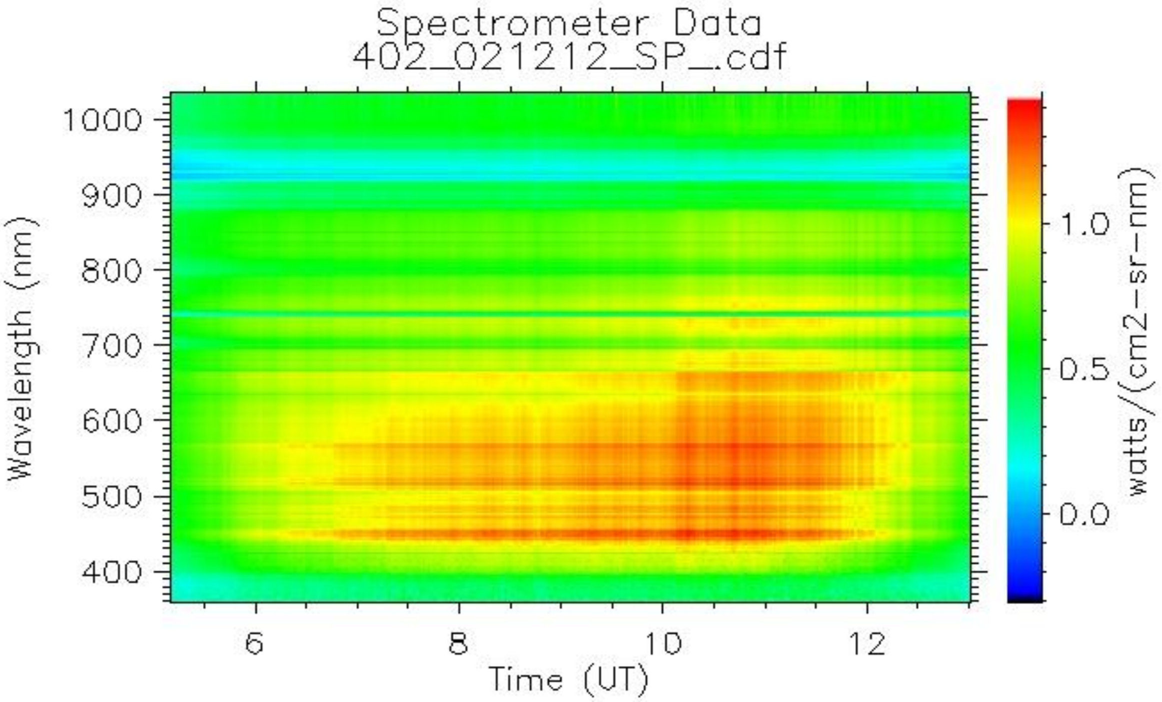

Figure 5.6: Spectral Distribution of radiance from wavelengths 400 to 1000 nm from SAM

5.2 Comparison of SPI and SAM based CSR's

The broadband CSRs from the SAM are compared to the estimated CSRs from the inverse Buie model of the SPI sunshape trajectories. It is important that all the data required for the post processing the SAM images is available from the same site and that all the sensors are maintained well, to accurately predict the broad band CSRs from the aureole profiles of the SAM. The spectral irradiance from the Sun Photometer was not available at the site during the experimentation with the SAM. Hence, the data from an aeronet station at Mezaira, 200 km away from Masdar has been used for post processing (Aeronet Aerosol Robotic Network, 2004).

CSRs from the SAM may not be reliable due to the lack of regular cleaning and unavailability of the spectral irradiance data. Figure 5.7 shows the CSRs of the SAM and the SPI between 9:30 am to 10:30 am on the 15th of February. It is observed that the estimated CSRs from the SPI-inverse Buie model follow in the trend of SAM but due to the reasons mentioned previously, proper validation of the CSR results cannot be made. The CSRs from both the instruments however, appear to be within the same range of 0.3 at 9:30 am to 0.2 at 10:30 am with an RMS deviation of 2.294%. RMS deviation indicates the deviation between the CSRs from the SPI and SAM as shown in equation 5.1:

$$\text{RMSD}=\sqrt{\frac{\sum_{i=1}^{N}\left((CSR_{SAM})_i-(CSR_{SPI})_i\right)^2}{N}} \tag{5.1}$$

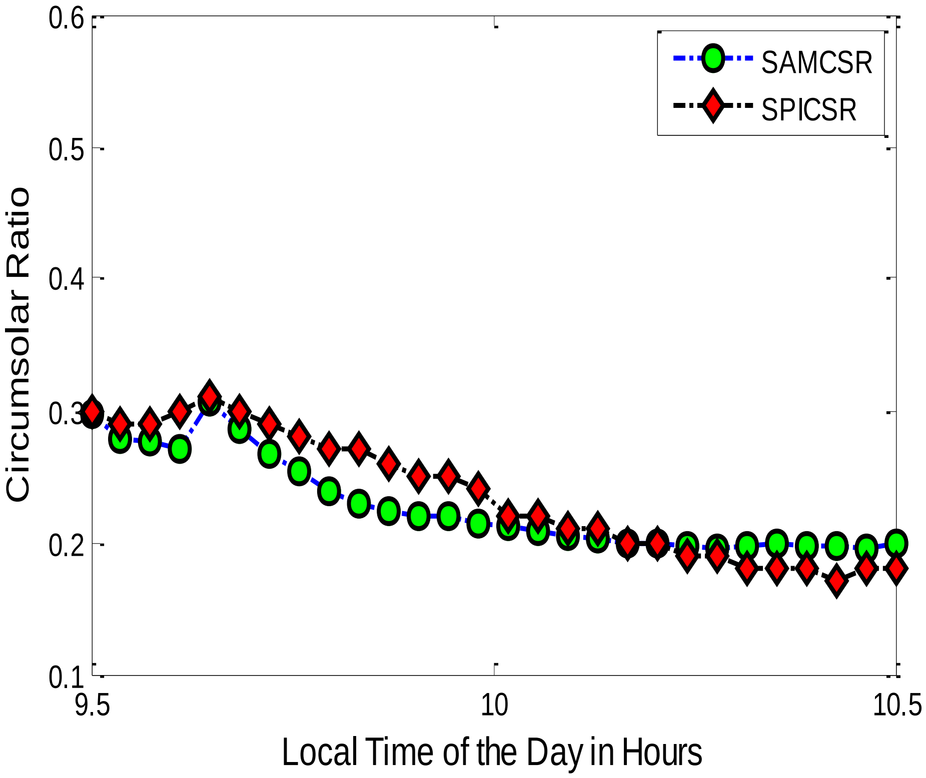

Figure 5.7: SPI-inverse Buie and SAM based CSRs on 15Feb-2012

CSRs obtained from the two instruments are compared in Figure 5.8 and Figure 5.9 on different days. The trends in the variation of CSR's with time of the day and with the DNI appear to be the same. The RMS deviation of the two CSR estimations on the 16th Feb is 5.51%. The RMS deviation of the CSRs from the SAM and SPI-inverse Buie model on the 19th Feb from 11:00 am to 17:00 pm is 4.238%. For the three days of proper SAM operation, the RMS deviations calculated from the CSRs of SPI-inverse Buie and SAM from the aureole profiles measured by both the instruments at the same location and time are observed to be fairly low.

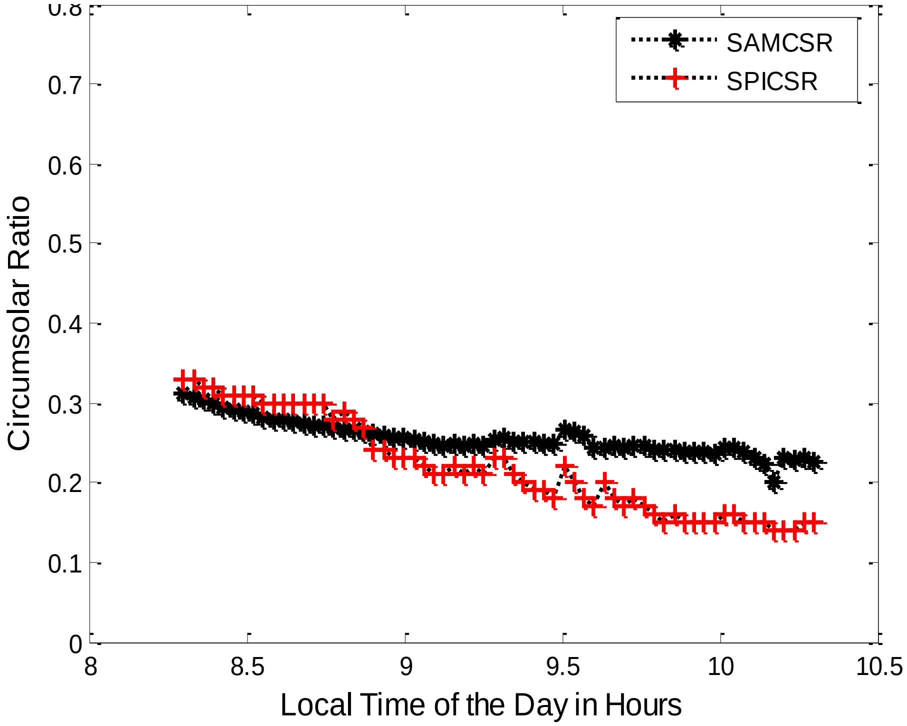

Figure 5.8: CSRs estimated from SAM and SPI-inverse Buie Model on 16Feb.

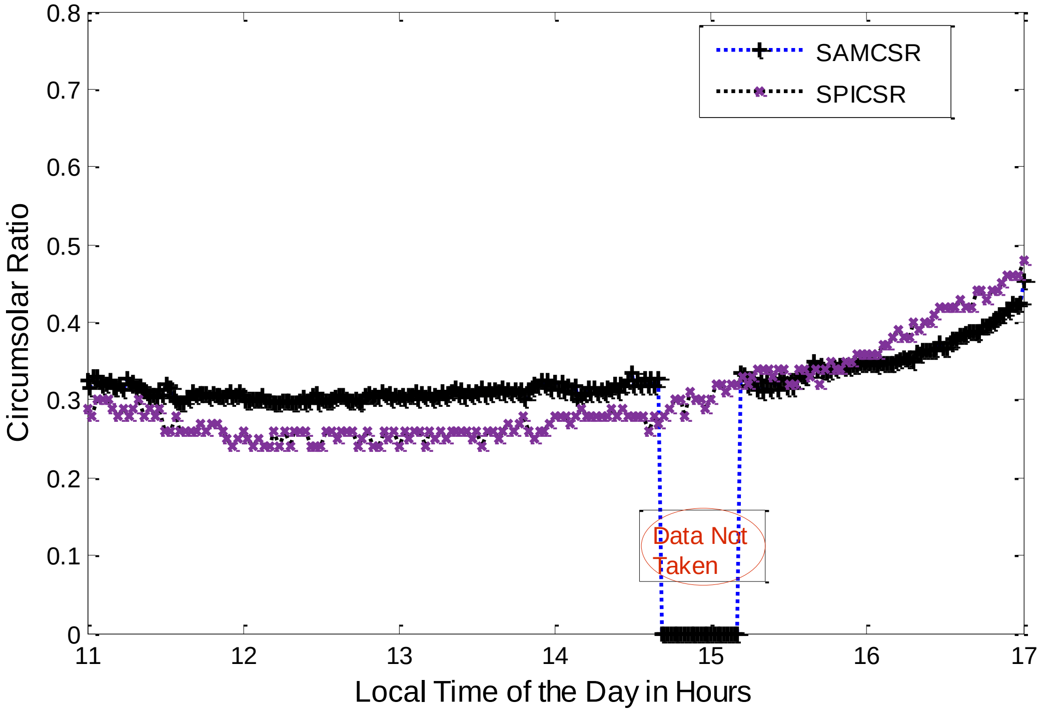

Figure 5.9: CSRs estimated from SAM and SPI for every 2 minutes time interval on 19Feb.

5.3 Inference from the SPI-SAM CSR comparison

Both the SPI and SAM broadband results show similar trends and variation with time of the day as well as DNI. From the CSR trends and low RMS deviations from the SAM results, one can see the potential of SPI to be used for obtaining the circumsolar brightness profiles with the proposed inverse model. However, it requires high quality large datasets from both the SAM and SPI to fully validate the SPI instrument and retrieval methods. All the post processing parameters for the CSR estimation from the SAM must be taken from the same site for more accurate results. Hence, more data observation, processing and experimentation with the SAM is needed for comparison of the CSR estimates from the two instruments.

CHAPTER 6

Direct Inversion Model

Buie's model is observed to work well only for clear sky conditions and the assumed angular extent of the solar aureole is only 43.6 mrad. The least squares method gives a close estimate of the CSR from the inverse Buie model but it cannot be used to determine the CSR precisely. Moreover, the actual sunshape radial brightness profiles cannot be obtained from the inverse model based on Buie's equations because Buie's model assumes:

- Radial symmetry
- A functional form of the aureole radial brightness profile
- A functional form of the solar disk radial brightness profile
- Slope of aureole brightness profile changes to zero abruptly when the diffuse sky brightness is reached.

Hence, a more complete and rigorous model is needed to obtain the actual brightness profiles for regions that have large aerosol concentration, relative humidity and hazy skies like Abu Dhabi since the existing sunshape models are based on clear sky conditions. It is theoretically possible to obtain the brightness profiles from 1-axis sky scans under less restrictive assumptions. In other words, we wish to infer the actual sunshape from an SPI signal trajectory.

In this chapter, a direct inversion model is derived that uses an enhanced sky model to obtain the radial brightness profile by using weights that correspond to the view factors of the solar disk, aureole and the sky region as viewed from the slot of the full globe SPI model during its traverse of the sky.

The full globe slotted SPI model is mentioned in Chapter 3 as a possible alternative to the design of the SPI in which the receiver is placed inside a slotted globe such that as the slot rotates, the receiver can measure the irradiance from each strip of the sky. This has not been manufactured due to the low fabrication facilities. This variation of the SPI, along with the direct inversion of the trajectories obtained from it would give the actual radial brightness profiles all over the sky. Apart from the sunshape profiles, this model can also estimate the true DNI, DHI, brightness at any strip or region in the sky.

New assumptions for the Direct Inversion model include:

- Radial symmetry of the circumsolar region.
- Uniform brightness of ground.

6.1 Geometrical Model

The sky is divided into a number of N-S strips by great circles of a unit sphere running in the North-South direction (lines of longitude). The position of the sun in the sphere is calculated from the declination and hour angle for a particular day and time. The SPI is adjusted already for the latitude of the location by the tilt angle of the receiver; hence, this model is applicable for any location with the latitude- adjusted SPI. Concentric circles representing the sun aureole are assumed to extend up to the whole sky region. Brightness points are enclosed within quadrilaterals formed by the great circles of the sphere running from N-S direction and concentric circles with solar disk as the center as shown in Figure 6.1 (not to scale). The entire sky region is divided into strips passing through these curves which are further more divided into quadrilaterals (boxes surrounding the brightness points) with finite areas that contribute to the weights of the view factors of each region of the solar disk, circumsolar and sky region.

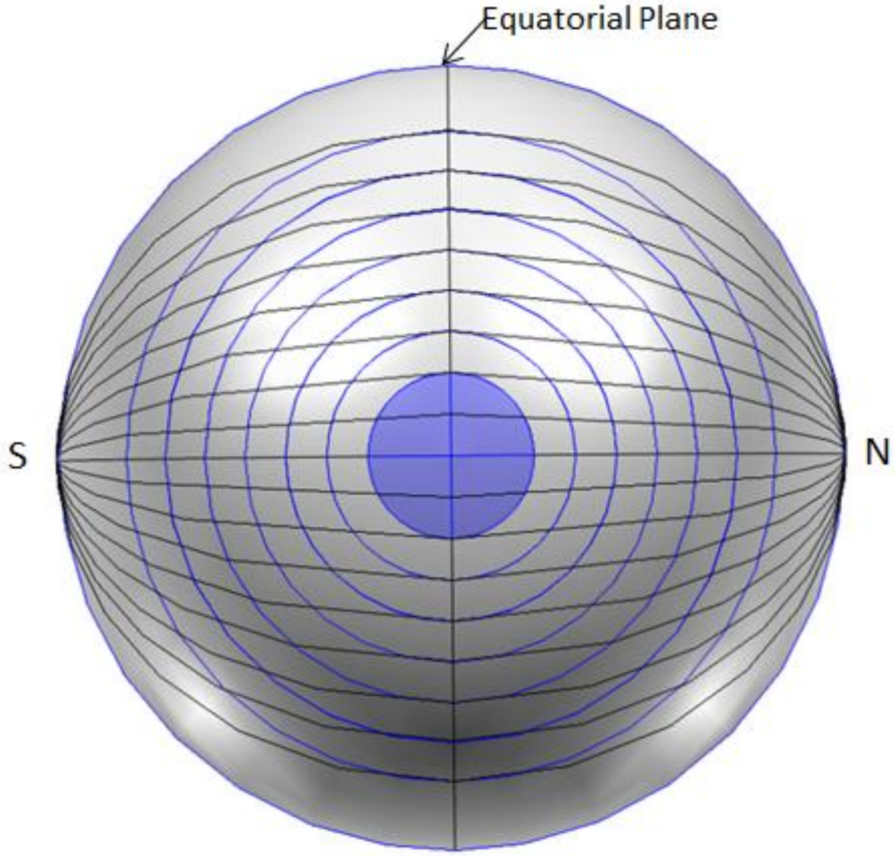

Figure 6.1: Geometry- direct inversion model (special case: declination=0^o, hour angle =0^o)

Figure 6.1 describes the geometrical model for a particular case when the sun is on the equator during solar noon at equinox (declination =0^o and hour angle of the sun =0^o). Depending on the time of the day and declination, the angle from the vertical plane to the center of the solar disk and other angle from the horizontal plane to the disk center keep varying. Hence, the geometry of the concentric circles changes according to the declination and hour angle of the sun.

The solid circle on the sphere in Figure 6.1 indicates the solar disk and the concentric circles formed around the disk represent the radial brightness zones including the circumsolar region of the sky. The great circles represent the directional stepwise motion of the shadowband from one end of the sky patch to the other covering the solar disk at the center of the trajectory. The intersection points of the longitudinal curves and the circles represent the brightness points. The positions of these brightness points are obtained from spherical geometry and then the areas of the quadrilaterals containing the brightness points in the middle are calculated. For simplicity, the intersection points of the curves containing the brightness points (β) are joined perpendicularly to the great circles on either side in order to obtain rectangles similar to Latitude-Longitude rectangles on the spherical surface of the earth. The latitude angles however, are obtained from the intersection of the circles around the solar disk with the great circles that represent the longitudinal curves. The distribution of brightness points in the quadrilaterals is shown for one quadrant of the hemisphere in Figure 6.2. The sky geometry discussed in Figure 6.1 is zoomed in to one quadrant considering symmetricity amongst the other quadrants for this special case when the sun is at equinox, on the equator at solar noon. When the hour angle of the sun and declination changes, the symmetry condition is no longer valid and the angles of the concentric circles change accordingly. The brightness at the center of the disk is represented by β_o shown in Figure 6.2 (not to scale). The distribution of brightness points from β_1 is illustrated in Figure 6.2. The brightness points are all considered to be concentric to the center of the solar disk to create a matrix such that the distance from the center (first point) to each brightness point on each strip varies according to the equation of a circle. The cross section of each quadrilateral is numerically calculated to obtain the area matrices discussed in the next section.

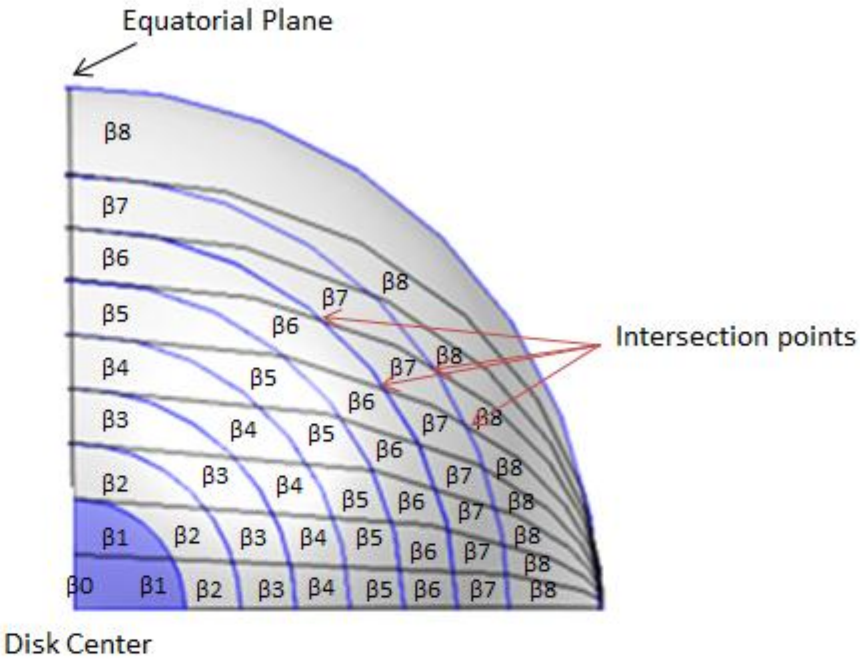

Figure 6.2: Distribution of Beta (Brightness Points) in the direct inversion model

6.2 Inversion procedure

The procedure for direct inversion of the SPI signal using view factors follows the logical sequence as below:

Step ϕ: A grid comprising different aperture angles $\vec{r}$ is generated for creating the concentric circles around the solar disk. Another similar grid is created for angles of the great circles (longitude curves) on the equator or 0^o latitude plane.

Step1: Generate of Position Matrix from $\vec{r}$: This matrix determines the positions of the intersections points between the great circles and the concentric circles around the solar disk. Brightness points shown in Figure 6.2, are contained in the centers of the quadrilaterals formed by four of these intersection points (two consecutive latitude points on every two consecutive longitude curves) from the position matrix.

From the arcs formed between every two consecutive longitude curves and cone angles from the center of the concentric circles on great circles, the third arc joining the equator plane to the intersection points of the longitude curves and concentric circles can be obtained. This is done by applying spherical Pythagorean Theorem on the spherical triangles formed by these arcs. The angles from the equatorial plane to the intersection points are obtained from the arc lengths calculated by the spherical Pythagorean Theorem (equation 6.1). If the sides of a spherical right triangle (R= radius of sphere) are a,b and c, such that c is the side containing the hypotenuse,

$$\cos(c/R)=\cos(a/R)*\cos(b/R) \tag{6.1}$$

Step2: Calculate cosine factor of each box containing a Brightness Point: A simple example of the situation when the sun is pointing directly above the receiver during solar noon, at the equator in an equinox condition has been shown in Figure 6.3. The quadrilateral formed at the center of the solar disk is assumed to be directly on top of the receiver, which implies that all the other quadrilaterals in the model are positioned at an angle from the center. Hence, the cosine component of the intensities from these quadrilaterals falls on the receiver.

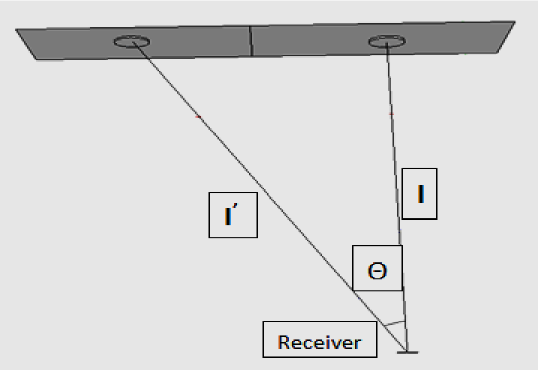

Figure 6.3: Cosine Factor for each quadrilateral from the receiver

From Figure 6.3, if the radiance of the directly perpendicular box from the receiver is I and then radiation falling from the other box at an angle θ from the receiver normal is given by:

I ’cos (θ)*F (θ,az) (6.2)

F (θ,az) is the angular correction to the cosine response of the detector which is calculated by measuring the instrument’s response to a stabilized parallel uniform light beam in the laboratory as discussed by (Armstrong, Schmelzer, Flynn, Hodges, & Michalsky, 2006). However, we may find the azimuth effect (az) to be weak. Each instrument is calibrated for deviations from the ideal cosine response. The procedure for this calibration and observed cosine response is included in Appendix F. The cosine response has not been calibrated for SPI yet but it is intended to be done in the near future.

Step3: Area Matrix: The cross section of each quadrilateral contributes to the weights of the view factors from each strip of the sky. The areas of the spherical quadrilaterals formed by the intersection of the curves with brightness points in the middle are calculated by assuming the geometry of quadrilaterals as latitude longitude rectangles as shown in Figure 6.4. Perpendicular arcs between the great circles (longitudes) produced from the intersection points of the curves containing the brightness points create latitude- longitude rectangles. In this model, the latitude points are calculated from spherical trigonometry at every point of intersection.

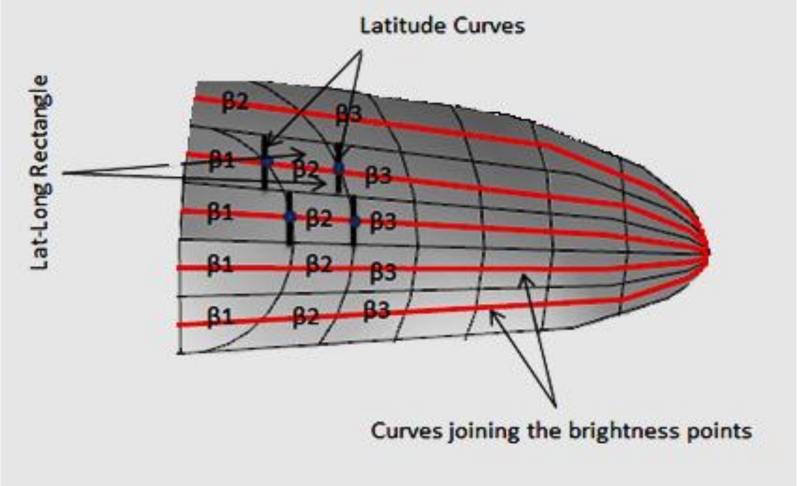

Figure 6.4: Latitude- Longitude Rectangles for the Area matrix

The area of the latitude- longitude rectangle formed on a unit sphere is calculated as follows:

$$\text{Area}=\frac{\pi}{180}*|\sin(\text{latitude1})-\sin(\text{latitude2})|*|\text{longitude1}-\text{longitude2}| \tag{6.3}$$

Latitudes 1 and 2 represent angles from the plane of equator to the two points on either side of a brightness point (β) and Longitudes 1 and 2 represent the angles of two great circles on the equatorial plane within which the quadrilateral is enclosed.

The idea behind generating the Area matrix is that if the intensity of the strips observed from the slotted full globe is given by X_i, then it is obtained by equation 6.4:

$$X_i = \sum Area_{ij} * \cos(\theta_{i,j}) * F(\theta, az) * \beta_j \tag{6.4}$$

The A matrix is created from the product of Area and cosine (θ) matrices and β represents the brightness points. The detector signal or cosine-corrected average brightness (X_i) from each strip is calculated as:

$$X_o= A_{0,0}\beta_0 + A_{0,1}\beta_1 + A_{0,2}\beta_2 + A_{0,3}\beta_3 + \ldots\ldots\ldots\ldots\ldots\ldots + A_{0,n}\beta_n$$

$$X_1= A_{1,1}\beta_1+ A_{1,2}\beta_2 + A_{1,3}\beta_3 + \ldots\ldots\ldots\ldots\ldots\ldots + A_{1,n}\beta_n$$

$$X_k= A_{k,k}\beta_K+ A_{k,k+1}\beta_{k+1}+ \ldots\ldots\ldots\ldots\ldots + A_{k,n}\beta_n$$

$$X_n= A_{n,n}\beta_n$$

Step4: Brightness Profile (Beta): If X_i represents the measured signal from a slotted full globe, the brightness profile (β) can be obtained from the product of the inverse of A matrix times the Measured signal (X).

$$\vec{X}= \bar{\bar{A}}*\vec{\beta} \Rightarrow \bar{\bar{A}}^{-1}*\vec{X} = \vec{\beta} \tag{6.5}$$

6.3 Obtained Brightness Profile from the described procedure

Linear spacing sequence of $\vec{r}$ is not required, rather a fine grid of $\vec{r}$ only in the circumsolar region is desired, and the grid can further be modified to a coarse grid in the sky region outside the aureole. Area matrix is generated for all the points of $\vec{r}$ with the equation for the area of latitude-longitude rectangle as described in the previous section. The Area matrix is verified by adding the areas of all the spherical rectangles of the sphere to check if the summation gives the surface area of a unit sphere which is 2π steradians. A course grid of 10^{o} spacing area matrix for one quadrant of the sphere is used to verify the Area matrix in Table 6.1.

Table 6.1: Area matrix for a coarse grid for verification

			A matrix for one Quadrant						Summation	
0.030	0.029	0.028	0.025	0.022	0.017	0.013	0.008	0.003	0.175	
0.052	0.031	0.027	0.023	0.018	0.013	0.008	0.003		0.175	
0.068	0.033	0.026	0.020	0.015	0.009	0.003			0.175	
0.081	0.036	0.026	0.018	0.011	0.004				0.175	
0.095	0.037	0.024	0.014	0.005					0.175	
0.110	0.038	0.020	0.006						0.175	
0.127	0.036	0.011							0.175	
0.150	0.024								0.175	
0.175									0.175	
								total	1.571	equal to pi/2

From Table 6.1, it is observed that the summation of areas of the latitude-longitude rectangles enclosed within two consecutive longitudinal curves forming a lune is always the same due to the constant dihedral angle between every two longitudinal curves (great circles) considered in this analysis.

After the Area matrix verification, a sample calculation is performed for the special case of sun position on the equator at equinox with fine grid of equal spacing for the concentric circles as well as great circles for the whole sky.

The intersection points of the concentric circles with the longitudinal curves are calculated using the spherical trigonometry which produces the required $\vec{r}$. The areas of the latitude longitude rectangles are calculated as discussed previously from equation 6.3.

The aim is to obtain the Brightness distribution profile or the brightness points from this model from the measured signal X. Due to the unavailability of measured signal X from the full globe variation of the SPI, the values of X have been estimated numerically. The area matrix is multiplied with the β points generated as shown in equation 6.6:

$$\beta = \begin{cases} Buie's\ Brightness, & B(r) > DHI \\ Diffuse\ Horizontal\ Radiation, & B(r) < DHI \end{cases} \tag{6.6}$$

The brightness distribution of Buie’s sunshape is considered up to the angular limit $\vec{r}$, until the brightness is higher than the diffuse sky radiation (W/m^2/steradian) with the assumption of isotropic sky radiation distribution outside the circumsolar region. When the diffuse radiation is larger than Buie’s brightness, β is assumed to remain constant and equivalent to the diffuse radiation for isotropic sky.

X is obtained from the product of A matrix with the generated β. Noise is added to the obtained signal (X) in order to make it more realistic as the measured signal from the slotted full globe. Inverse calculations are performed on this measured signal to obtain the brightness profile (Beta) originally used to derive the measured signal without noise.

6.3.1 Calculation Example

Assumptions:

- CSR=10% (0.1)
- Sun Position: Top of the equator at equinox

- Zenith angle (θ_z) =0^o, Elevation angle (el) =90^o, Location altitude(A) =0

For this example, Beta points were first generated from Buie's sunshape for CSR=0.1. From the correlation of CSR with Direct Normal Irradiance and Global Horizontal Irradiance (Neumann, von der Au, & Heller, 1998), the ratio of DHI/GHI or R_{dg} is obtained as a function of elevation:

CSR is related to R_{dg} and F (el) as shown in equations 6.7 and 6.8 discussed by (Neumann, von der Au, & Heller, 1998):

$$CSR= 70 - 65.948*R_{dg}/F\ (el) \tag{6.7}$$

$$F(el)= 15.9822*(elevation)^{-0.669} \tag{6.8}$$

DNI through clear atmospheres is obtained from Hottel's model with the zenith angle, altitude and climate type in the location as the input parameters. The atmospheric transmittance is defined by equation 6.9 (Duffie & Beckman, 2006, Third Edition):

$$\tau_b = a_0 + a_1 \exp\left(\frac{-k}{cos\theta_z}\right) \tag{6.9}$$

where the constants a_o^*, a_1^* and k^* depend on the location altitude, in this case, it is taken as zero.

$$a_o^*= 0.4237- 0.00821(6-A)^2$$

$$a_1^*= 0.5055+ 0.00595(6.5-A)^2$$

$$k^*= 0.2711+ 0.01858(2.5 -A)^2 \tag{6.10}$$

a_o, a_1 and k are obtained from the ratio of the above coefficients with the correction factors (r). The correction factors vary with the climatic conditions of the location. For this case, mid-latitude summer is considered to obtain the correction factor from Hottel's model. Then the DNI for the day is calculated from the extraterrestrial radiation (G_{on}):

$$G_{beamnormal} = G_{on}\tau_b \tag{6.11}$$

Horizontal beam radiation on hourly basis is obtained from equation 6.12:

$$I_{cb} = I_{on}\tau_b cos\theta_z \tag{6.12}$$

The extraterrestrial radiation G_{on} is obtained from the day of the year as (Duffie & Beckman, 2006, Third Edition):

$$G_{on} = G_{sc}(1 + 0.033cos\frac{360n}{365}) \tag{6.13}$$

where n is the day of the year, G_{sc} is the solar constant= 1367W/m^2

GHI is estimated from the obtained DNI through the CSR correlation ratio R_{dg} from which the DHI is estimated as in equation 2.10 of chapter 2.

Buie's sunshape produces normalized profiles of the brightness distribution; hence, the curves are needed to be denormalized in order to compare the radiance of the Buie's brightness with the DHI. Hence, the normalized brightness values of the points within the full aperture angle of 5^o are integrated to find the factor (F) which when multiplied to the integral equals the measured DNI by the pyrheliometer within a solid angle of 5^o.

$$F * 2\pi \int_0^{2.5} rB(r)dr = DNI\ measured\ from\ a\ solid\ angle\ of\ 5^o \tag{6.14}$$

It is observed that the intensity of Buie's sunshape at 5.85 mrad half angle is equivalent to the DHI at a low value of assumed CSR of 0.1 at zenith angle= 0^o. However, for higher CSR's of

0.5, it is observed that the Buie's Sunshape equals the DHI at 52.3 mrad which is outside the 43.6 mrad aureole limit.

The obtained signal X from the product of A matrix with Beta (from Buie plus diffuse radiation outside the calculated aureole limit) is treated as the measured signal after adding noise with signal to noise ratio =30 as shown in Figure 6.5.

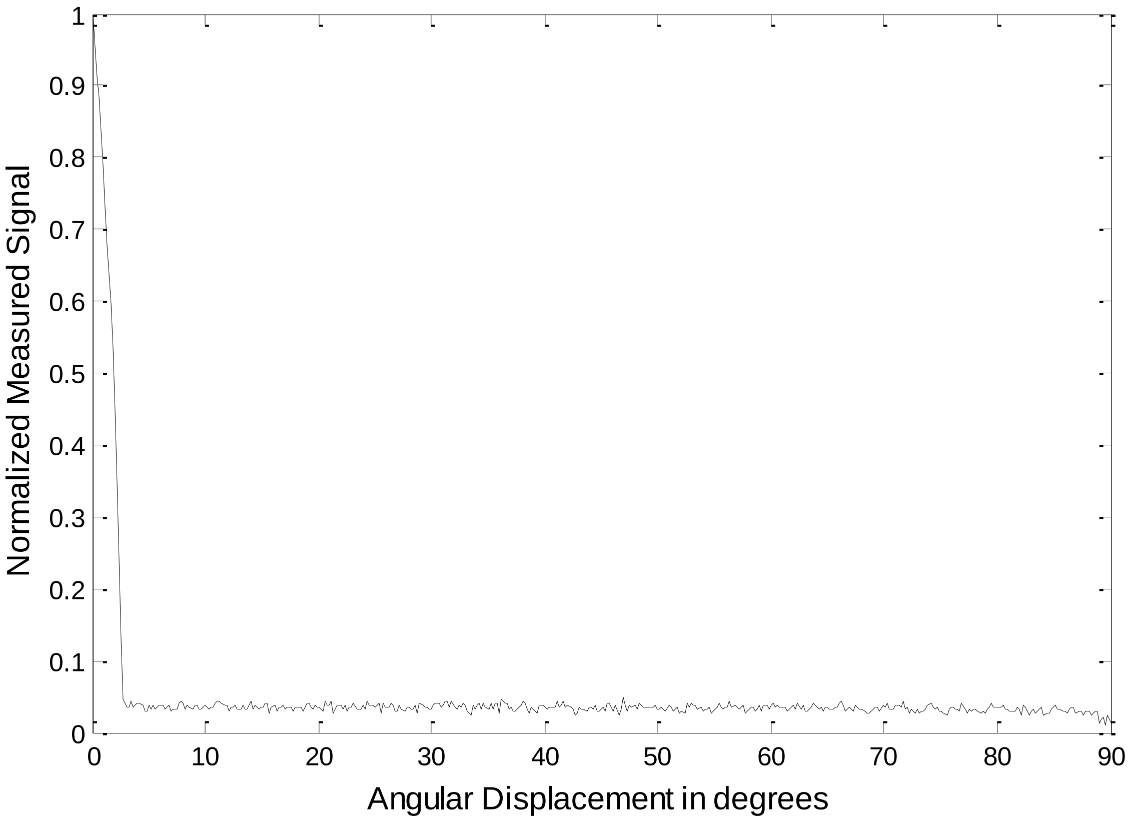

Figure 6.5: Measured SPI full globe signal

The brightness distribution of Beta points is obtained from the product of the noisy X (measured signal) with the inverse matrix of A as shown in Figure 6.6. This shows that the direct inversion procedure can be used for obtaining the brightness profiles for any circumsolar ratio and for any climatic condition. A more complete inversion procedure with truly measured radiation would prove to be useful for obtaining the whole sky mapping. This could be used in climate research as well as improved resource characterization for applications that need an accurate circumsolar and/or sky model such as concentrating solar power (CSP, CPV), day lighting, and evaluation of the urban heat island.

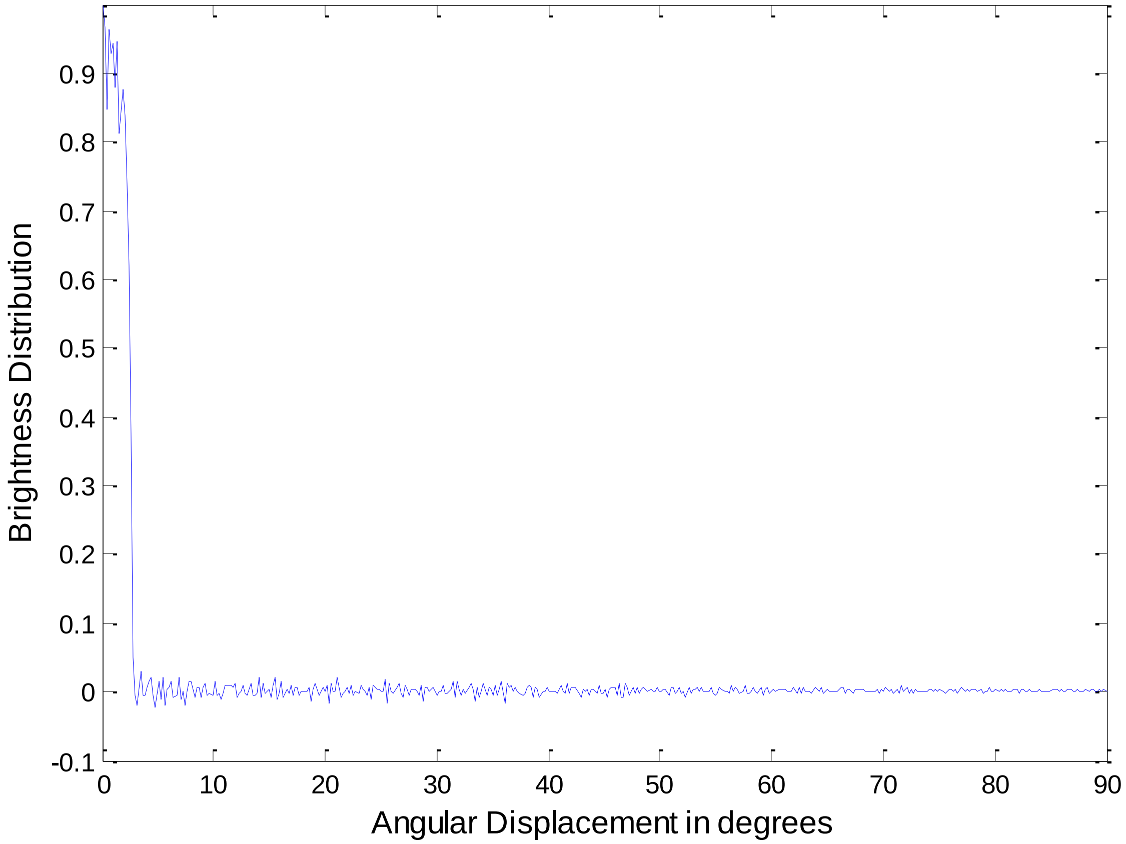

Figure 6.6: Brightness Profile from Direct Inversion

It is important to note that β(r) (obtained brightness profile) shown in Figure 6.6 from the direct inversion can be smoothed by using a coarser grid of $\vec{r}$ as one moves further from the solar disk. Then, the derived brightness profile would be less noisy than that shown in Figure 6.6.

CHAPTER 7

Conclusions and Recommendations

This thesis describes the development and validation of the initial performance of a new instrument called the Sunshape Profiling Irradiometer (SPI) for measuring the circumsolar brightness profile. Two numerical models have been formulated to retrieve the sunshape profiles.

One method uses Buie's model for the terrestrial spatial distribution of normalized circumsolar profiles to get an estimate of the CSR from the trough trajectory of the SPI. It is observed that Buie's model in low turbidity but hazy atmospheric conditions that occur often in Abu Dhabi, the simulated SPI signals do not perfectly match the measured SPI signals. The assumed limit of the subtended angle (43.6 mrad) from the center of the solar disk to the aureole extent used by Buie appears to be too small when aerosol content and humidity are high.

Due to lower limit of the subtended angle of circumsolar region from the center of the solar disk, the edges of the simulated signal outside the umbral region have constant values for the simulated signal. However, on hazy days with high circumsolar ratios, the measured signal has a continuously changing trend of the intensity as we move away from the umbral region of the trough trajectory until we enter into the sky region. Hence, a more complete model for the estimation of CSR based on View Factors of discretized regions of the disk, aureole and sky is proposed. The resulting basis functions are purely based on geometry and hence, can be used to map the whole sky for any climatic condition. The brightness profiles for a general case of the sun's position at the equator during equinox are derived with this model for the full globe model of the SPI.

In the inverse Buie model, least squares regression is performed on the measured signal with the family of simulated curves with varying CSRs. The best fit of the curves with least mean squared error identifies the CSR with respect to the measured SPI trajectory. The inverse model results have been analyzed under different sky and atmospheric conditions from which different trends of CSR variation with time of the day and air mass have been obtained. The coefficient of least squares (ξ_o) pertaining to the sky radiation plus part of ground reflected radiation falling on the receiver is observed to be proportional to the DHI outside the rectangular patch of the assumed Buie sunshape. The other coefficient (ξ_1) is observed to be proportional to the DNI plus circumsolar contributions with appropriate cosine corrections within the solid angle of the rectangular patch. This shows the potential of the SPI to also function as a conventional RSI.

The effect of circumsolar radiation on the acceptance angles of parabolic troughs is studied and numerically analyzed with an optical model proposed by (Bendt, Rabl, Gaul, & Reed, 1979). The intercept factors with varying CSRs have been obtained for parabolic troughs with geometry and design from Euro Troughs standards under the weather conditions at Masdar. It is observed that the impact of circumsolar radiation on the intercept factors of parabolic troughs is high on dusty days as compared to clear days. This impact is expected to be even higher for point focus solar concentrating technologies like parabolic dishes, central receiver towers etc. For regions with high concentrations of aerosols, humidity, etc. the circumsolar radiation is observed to play a vital role in determining the true optical efficiency and thus, the power output of the plant.

The CSRs obtained from the SPI trajectories with the inverse Buie model are compared with the broadband CSRs obtained from the SAM based system. Due to operational problems with the SAM, validation of results is incomplete. But the CSRs from SPI-inverse Buie model are observed to follow the trend of the CSRs from the SAM. Validation and comparison of the CSRs is ongoing to fully demonstrate the inverse model as well as describe the potential of the SPI and the inverse model for obtaining the circumsolar brightness profiles.

Future Recommendations

Improvements and future works can be listed under several categories:

a. Instrument modifications
    - Sensitivity study of noise with respect to the width of the slit receiver and optimization of the shadowband width to yield more informative trough trajectories even at higher CSRs.
    - Micro stepping to increase the resolution of the steps in order to get more data points for the inverse model would result in more precise estimation of the circumsolar profile near the edge of the disk.
    - Use of different multi filter detectors for the brightness profiles at different wavelengths to get a better understanding of the forward scattering of molecules and particles as function of wavelength.

b. Brightness profile retrieval
    - Model the direct inversion with a coarser grid of $\vec{r}$ outside the circumsolar region in the direct inversion model to obtain smooth brightness profiles.
    - Measure and apply cosine correction to slit receiver and refine optical design of the detector fore optics (slit receiver).

  - Measure SPI trajectories for the whole sky to obtain the actual brightness profiles from which sunshapes and whole sky flux can be mapped by using the direct inversion model.

c. Validation and deployment

  - Process more data from the SAM to compare and validate the inverse models and performance of the SPI hardware.

d. Met- analysis

  - Explore the relation between aerosol size distribution and CSR.

APPENDIX A

Abbreviations and Nomenclature

CSP	Concentrated Solar Power
CPV	Concentrated Photovoltaics
DNI	Direct Normal Irradiance (W/m^2)
DHI	Diffuse Horizontal Irradiance (W/m^2)
GHI	Global Horizontal Irradiance (W/m^2)
CSR	Circumsolar Ratio
RSI	Rotating Shadowband Irradiometer
MFRSR	Multi Filter Rotating Shadowband Radiometer
SPI	Sunshape Profiling Irradiometer
WMO	World Meteorological Organization
LBL	Lawrence Berkeley Laboratories
RDB	Reduced Data Base
DLR	Deutsches Zentrumfür Luft- und Raumfahrt (Germany's aerospace agency)
SAM	Sun and Aureole Measurement System
RMSD	Root Mean Squared Deviation
MSE	Mean Squared Error
CCD	Charge Coupled Device

θ_c	Half acceptance angle
C_{max}	Maximum theoretical concentration
R_b	Ratio of beam radiation on tilted surfaces to that on horizontal surface at any time
Φ_{cs}	Radiant flux contained within the circumsolar region of the sky
Φ_i	Incident radiant flux from the solar disk and circumsolar region
$B(r)$	Radial distribution of the solar and circumsolar brightness at an angular distance r
$I_{d,T}$	Diffuse radiation on a tilted collector
$I_{T,d,iso}$	Isotropic component of the diffuse radiation
$I_{T,d,cs}$	Circumsolar component of diffuse radiation
A_i	Anisotropy index
I_{bn}	Beam Normal Irradiance
I_{on}	Extra-terrestrial irradiation
β	Slope of collector or receiver
F_1	Circumsolar Brightness Factor
$E_{dc\lambda}$	Gueymard's circumsolar irradiance
$L_a(\xi)$	Azimuthally averaged radiance that exists along the almucantar
$P(\xi)$	Phase Function
θ_z	Zenith Angle
F_s	Extra-terrestrial solar flux
μ_s	Cosine of the Solar zenith angle
τ	Total vertical optical depth
γ	Gradient of the radiance profiles in log- log space
κ	Intercept of angular radiance distribution curve at an angular displacement of zero

$\alpha-\alpha_o$	Distance of each point on a line from the center line of the strip of Buie's rectangl
ω	Perpendicular distance to the position of shadowband in Buie's rectangular patch
ξ_o	Least Squares coefficient proportional to diffuse radiation outside Buie's rectangle
ξ_1	Least Squares coefficient proportional to direct radiation within the rectangule
I_ω	Intensity of a strip as viewed from a receiver at position ω
m	Air Mass
X	Intensity of each strip of the sky as viewed by the receiver on ground
β	Brightness points in Direct Inversion Model
R_{dg}	Ratio of DNI/GHI
τ_b	Atmospheric transmittance
n	Day of the year
G_{sc}	Solar Constant (1367 W/m^2)
$I_{measured}$	Measured SPI Signal for the Inverse Model with Buie's Sunshape
X	Measured SPI Signal for the Direct Inversion Model
A	Area Matrix multiplied with the cosine factor matrix
$F(\theta,az)$	Receiver/ detector's cosine response

Nomenclature for Appendix E

θ_i	Incidence angle on Parabolic Troughs of Bendt et. al optical model
C	Geometric Concentration Ratio ($C=D/\pi d$) of Parabolic Troughs
C_o	Optimal Concentration Ratio of Troughs from Bendt et. al optical model
$B_{real,sun}(\theta)$	Angular Profile of the real sun for line focus geometry ($W/m^2 rad$)
$B_{eff}(\theta)$	Effective source (W/m^2 rad)
$\Upsilon_{trough,linear}$	Intercept Factor of the effective linear line focus Trough- receiver

Υ_{Gauss}	Intercept Factor if sun is approximated by Gaussian distribution
D	Aperture width (m) of the parabolic collector
d	Diameter of the cylindrical absorber (m)
$E(\theta)$	Distribution function of optical errors (rad^{-1}) of the collector
$f(\theta)$	Angular acceptance function
$G(\sigma C)$	Function used for optimizing C
I_b	Beam component of solar irradiance (W/m^2)
I_d	Diffuse component of solar irradiance (W/m^2)
q_{in}	Portion of I_b that reaches the receiver (W/m^2 of aperture area)
q_{net}	Power output of the collector (W/m^2 of aperture area)
X_s	Contribution of shading term to critical intensity ratio
α	Absorptance of receiver
τ	Transmittance of receiver
ρ	Reflectance of receiver of parabolic troughs
$\sigma_{contour}$	Rms angular deviation of contour from design direction (mrad)
$\sigma_{displacement}$	RMS angular spread which accounts for imperfect placement of receiver (mrad)
$\sigma_{specular}$	RMS spread of reflected beam due to imperfect specularity of reflector material
$\sigma_{tracking}$	Angular error due to imperfect tracking of the collector (mrad)
$\sigma_{optical}$	Rms angular spread caused by all optical errors (mrad)
σ_{Sun}	Rms angular width of sun in line focus geometry (mrad)
σ_{tot}	Total rms beam spread (mrad)
φ	Rim Angle of the collector (mrad)
f	Focal length of the trough

APPENDIX B

RSI and MFRSR deployment in different locations

Rotating shadowband instruments are used in different research laboratories and industries due to their reliable single axis mechanism, low calibration errors, low maintenance, low cost, low misalignment and pointing errors. Table B.1 shows the different places that have deployed the MFRSR for Solar Resource assessment.

Table B.1: RSI and MFRSR Deployment at different locations (Kalapatapu, Armstrong, & Chiesa, 2011)

No	*Places using Rotating Shadowband Irradiometer and MFRSR*
1.	National Wind Technology Center M2 Tower, Colorado
2.	Solar Radiation Research Laboratory-Schott, Irradiance Inc., Ascension Technology, Inc.
3.	Solar Technology Acceleration Center (SolarTAC), MRI, Aurora, Colorado
4.	SMUD, Anatolia, California
5.	SOLRMAP: Tucson, AZ; South West Solar Technologies, AZ; Escalante, NM; Milford, UT;
	CA; Kalaeloa Oahu, HI, La Ola Lanai, HI; Swink, CO; San Luis Valley, CO
6.	Nevada Power Clark Station (NPCS), Nevada and University of Nevada, Las Vegas (UNLV)
7.	Lowry Range Solar Station (LRSS) and Xcel Energy Comanche Station (XECS), Colorado
8.	Sacramento Municipal Utility District (Anatolia), California
9.	Elizabeth City State University (ECSU), North Carolina
10.	Bluefield State College (BSC), West Virginia
11.	Humboldt State University (SoRMS) and San Clemente Island Data (SCID), California
12.	South Park Mountain Data (SPMD) and Lamar Low-Level Jet Project (LLLJP), Colorado
13.	ARM Radiometer Characterization System (RCS), Oklahoma
14.	Oak Ridge National Laboratory (ORNL), Tennessee
15.	Multifilter Rotating Shadowband Radiometer at Southern Great Plains (SGP), North Slope

16.	ARM Mobile Facility- FKB (Black Forest, Germany), GRW (Graciosa Island, Azores), HFE
17.	Solar MilleniumMeteostations, Spain
18.	Ultra Violet Multifilter rotating shadowband radiometers at Colorado State university,
19.	Reines Hall, University of California, Irvine Campus by Yankee Environmental Systems
20.	UT Austin, Clear Lake (NASA), Edinburg (UT Pan American), UT El Paso, Canyon
21.	Fifteen stations at Texas from Texas Solar Radiation Database
22.	National Solar Thermal Test Facility (NSTTF) at Sandia National Laboratories (SNL), New
23.	PSA, and several locations in southern Spain and Morocco by DLR
24.	CSIRO YES MFR7 Earth Observation Center (1); Atmospheric Research
25.	Global Monitoring Division, NOAA, US
26.	Pacific Northwest National Laboratory (PNNL), University of Hawaii- Manoa, and Aerosol

APPENDIX C

CR1000 Analog Specifications

Analog inputs of CR1000 include 8 differential or 16 single ended configured channels. Basic resolution is the Analog to Digital (A/D) resolution of a single conversion. Resolution and range of the differential measurements with input reversal is given in Table C.1.

Table C.1: Range and Resolution of Differential measurements (Campbell Scientific, 2008)

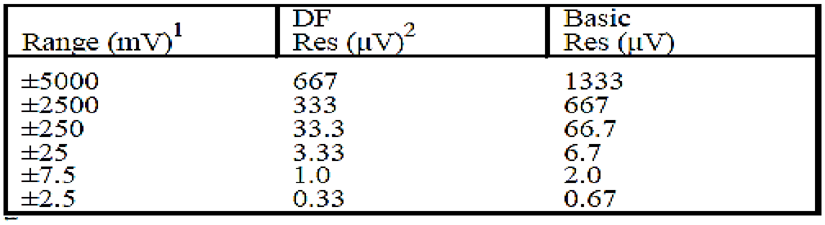

Range (mV)[1]	DF Res (µV)[2]	Basic Res (µV)
±5000	667	1333
±2500	333	667
±250	33.3	66.7
±25	3.33	6.7
±7.5	1.0	2.0
±2.5	0.33	0.67

We have used ± 25mV scale with a 2kΩ sensing resistor. Sustained input voltage without damage is within the maximum range of 16Vdc. Offsets for the differential and single ended measurements are calculated as given in (Campbell Scientific, 2008). Input noise voltage for differential measurements on 2.5 mV voltage ranges is 0.34 µV RMS for 250 µs integration and 0.19 µV RMS for 50/60 Hz integration. Output voltage at no load range goes as high as 5.0 V.

Table C.2: Input amplitude and frequency (Campbell Scientific, 2008)

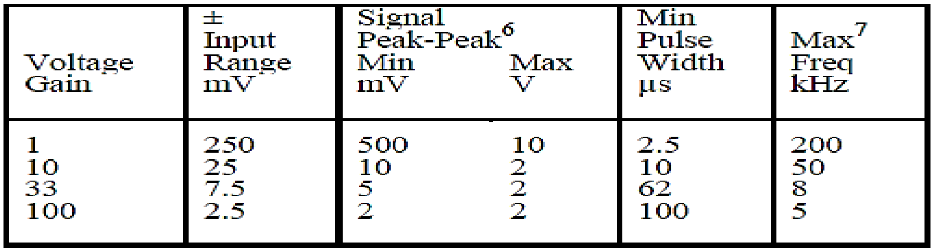

Voltage Gain	± Input Range mV	Signal Peak-Peak[6] Min mV	Max V	Min Pulse Width µs	Max[7] Freq kHz
1	250	500	10	2.5	200
10	25	10	2	10	50
33	7.5	5	2	62	8
100	2.5	2	2	100	5

APPENDIX D

SPI Alignment Procedure

The SPI’s motor bracket must be parallel to the local geographic North-South meridian. This can be done on a clear sunny day by obtaining the solar noon time for the location and rotating the SPI so that the motor bracket faces the same direction as the sun. It must be ensured that the bracket does not cast a shadow to either side of the band motor. The motor bracket should point south in the Northern hemisphere and North in the Southern Hemisphere. The instrument base should be leveled using a leveling bubble with three screws on the SPI base. Because the foregoing operations interact, they may need to be repeated if the base is significantly out of level initially. The receiver and its slit should be aligned such that the slit centerline is coaxial with the motor axis leveled in parallel and at the same height as the hub of the motor. The motor shaft should be mounted parallel to the earth’s rotational axis and a very precise latitude adjustment is needed to set the motor axis with tilt equal to the latitude of the site. Finally the shadowband angle on the shaft must be set to a 90^{o}east from the Nadir by tightening the hub screw while holding the band at 90^{o} east when the motor is in home position.

APPENDIX E

Intercept Factor of Parabolic Troughs as Function of CSR

Using the obtained CSR values from the SPI, the effect of the circumsolar radiation on the intercept factor and efficiency of a CSP- Parabolic Troughs plant has been studied and analyzed. The design and dimensions of the collectors are taken from Euro Troughs standards. A drop in intercept factor on parabolic troughs due to the influence of the circumsolar radiation on dusty days is demonstrated in chapter 4. The incident angle (θ_i) of the beam radiation is calculated by using the Zenith and Azimuth angles obtained from the solar position algorithm which requires the following inputs:

- Location-Longitude, Latitude and Altitude.
- Time-Year, month, day, hour, minutes, seconds, UTC.
- Where UTC is the offset hour given by:
- Local time= Greenwich Time + UTC time.

The absorber tube could be aligned with either North-South or East-west axis. This simulation considers North- South orientation as in Shams-1 and the incident angle is calculated using the equation for an N-S aligned solar trough collector as follows (Stine & Harrigan, 1985):

$$\theta_i=\cos^{-1}\{1-(\cos^2 A*\cos^2 (90-\theta_z))\}^{1/2}$$

The geometry of the collector, receiver, and their optical properties are all taken from Euro Troughs standards as shown in Table E.1 and Table E**.2**

Table E.1: Geometry of Euro Troughs (Geyer, et al., 2002)

Geometry of the Troughs and Receiver	Value	Unit
Distance between rows	17	m
Collector aperture width	5.75	m
Collector aperture area	817.5	m2
Total aperture area for collector	627840	m2
Length of single module	12.5	m
Number of modules per collector	12	
Collector length	150	m
Number of collectors per loop	4	
Number of loops	192	
Diameter of the absorber	0.07	m
Focal point	1.71	m
End loss factor	0.997	

Table E.2: Optical errors of Euro Troughs (Geyer, 2000)

Type of Error	From Euro Troughs	Type of Error	Used in simulation
Tracking Error	<3mrad	$\sigma_{tracking}$	3 mrad
Reflector Error	Avg<3 mrad	$\sigma_{specular}$	2 mrad
Position of Absorber Tube x,y	10mm, 10mm	$\sigma_{displacement}$	5.85 mrad
Contour Error	2 mrad	$\sigma_{contour\perp}$	2 mrad
		$\sigma_{contour\parallel}$	2 mrad

The methodology of calculating the intercept factor at the receiver is based on convolution of optical and surface errors of the collector with sunshape profiles which follows a logical sequence as discussed by (Bendt, Rabl, Gaul, & Reed, 1979):

- Ray Tracing on the collector

- Projection of the Sun Position and optical errors on the collector
- Convolution of optical errors with sunshape profile
- Obtain the angular acceptance function as a result of ray tracing
- Calculation of intercept factor and flux at the receiver for three types of sources: Ideal, Gaussian and Effective.

The intercept factor ϒ, as defined by Bendt et al. (1979) is calculated as shown in E.1 and E.2:

$$\gamma_{trough,linear} = \frac{q_{in}}{I_b} = \frac{\int_{-\infty}^{\infty} f(\theta) B_{eff}(\theta) d\theta}{\int_{-\infty}^{\infty} B_{eff}(\theta) d\theta} \tag{E.1}$$

$$\gamma_{Gauss} = \int_{-\infty}^{\infty} d\theta\, f(\theta) \frac{1}{\sigma_{tot}\sqrt{2\pi}} \exp\left(\frac{-\theta^2}{2\sigma_{tot}^2}\right) \tag{E.2}$$

Where $\gamma_{trough,linear}$ and γ_{Gauss} are the intercept factors for effective and Gaussian sources respectively, σ_{tot} is the total error of the system given by equation E.3 Bendt et al. (1979):

$$\sigma_{tot}^2 = \sigma_{optical}^2 + \sigma_{sun}^2 \tag{E.3}$$

The sunshape error and the optical errors are given by equations E.4 and E.5:

$$\sigma_{sun}^2 = \frac{\int_{-\infty}^{\infty} d\theta\, \theta\, {}^2 B_{sun,real}(\theta)}{\int_{-\infty}^{\infty} d\theta\, B_{sun,real}(\theta)} \tag{E.4}$$

$$\sigma_{optical}^2 = \sigma_{specular}^2 + \sigma_{displacement}^2 + \sigma_{tracking}^2 + (2\sigma)_{contour,\ effective}^2 \tag{E.5}$$

The effective source (B_{eff}) is the convolution of the intensity of radiation coming from an angular region of width $d\theta_{in}$ around θ_{in} and the total error (E), given by equation E.6 (Bendt, Rabl, Gaul, & Reed, 1979):

$$B_{eff}(\theta) = \int_{-\infty}^{\infty} E(\theta - \theta_{in}) B_{source}(\theta_{in})\, d\theta_{in} \tag{E.6}$$

The B_{source} is replaced by the DNI of the site in order to account for the ideal/ uniform source. F(θ) is the angular acceptance function, defined by (Bendt, Rabl, Gaul, & Reed, 1979) as, "*the fraction of rays incident on the collector aperture at an angle θ (from the optical axis) which reaches the receiver*". For a cylindrical receiver, intercept factor is obtained from equation E.7:

$$f_{trough,cyl}(\theta) = \begin{cases} 1 \; for \; |\theta| < \theta_1 \\ \cot\left(\frac{\emptyset}{2}\right) \left(\frac{2tan\frac{\emptyset}{2}}{\pi C\theta} - 1\right)^{1/2} for \; \theta_1 < |\theta| < \theta_2 \\ 0 \; for \; |\theta| > \theta_2 \end{cases} \tag{E.7}$$

Where C= concentration ratio which is the ratio of the collector area over receiver area (Duffie & Beckman, 2006, Third Edition).

Φ is the Rim angle of the trough, calculated as (Duffie & Beckman, 2006, Third Edition):

$$\emptyset = \tan^{-1}\left\{\frac{8(\frac{f}{a})}{[16(\frac{f}{a})^2 - 1]}\right\} \tag{E.8}$$

Where 'f' is the focal length and 'a' is the aperture width of the trough, θ_1 is the largest angle for which all the incident rays are accepted by the receiver, for angles larger than θ_2, only direct hits are accepted.

The intercept factor is calculated from the above described procedure for different circumsolar ratios from the 11 different LBL sites for a particular time of the day at different locations. Figure E.1 illustrates the decrease in the intercept factor with increase in CSR which also explains that the solar to thermal efficiency is reduced considerably at high CSRs.

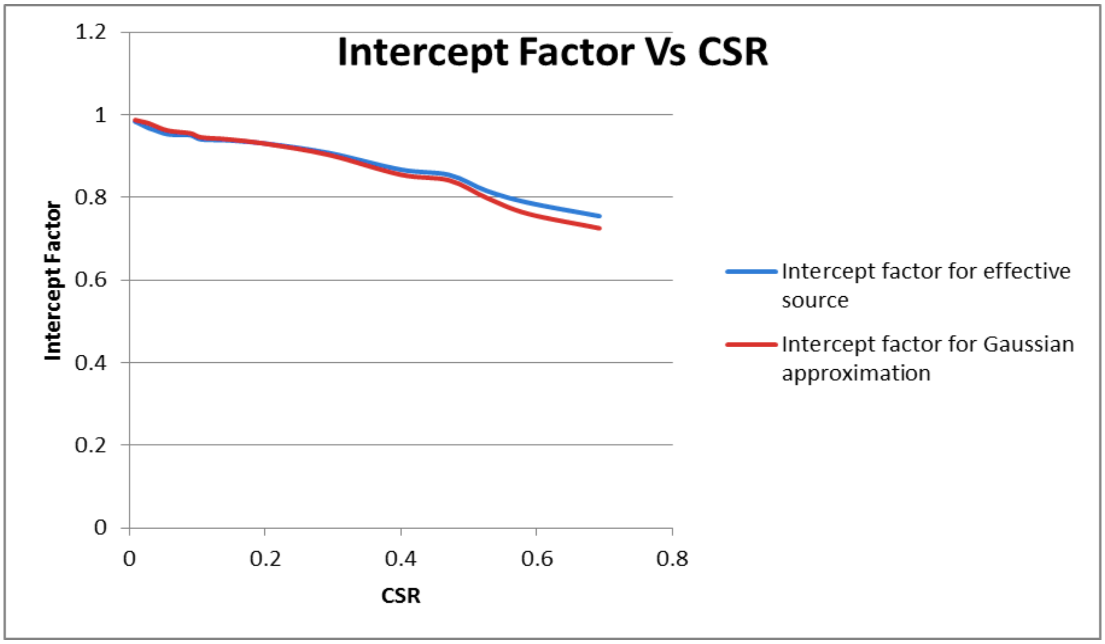

Figure E.1: Intercept Factor versus CSR

APPENDIX F

Cosine Response of the Detector

The cosine response of each MFRSR or RSI head is calibrated as:

1) under a 5000K standard lamp to establish response at a known irradiance,
2) in a spectrometer to establish normalized filter band pass functions, and
3) in a cosine test bench to establish cosine response.

The Cosine response may be characterized by rotating the head through 180° in one-degree increments from east to west and north to south. A typical set of responses is shown for Head 200 by (Armstrong, Schmelzer, Flynn, Hodges, & Michalsky, 2006) in Figure F.1. The red trace shows the east-west cosine response and the blue trace represents the north-south cosine response. The rotation fixture was modified in March 2006 to hold the test article in two additional azimuth orientations so that NW-SE and NE-SW sweeps can be performed conveniently and repeatedly. The NW-SE and NE-SW cosine responses are shown in Figure F.1 by the yellow and green traces respectively. It is important to note that there are significant interpolation errors (on the order of 0.5%) that can be avoided by doubling the number of azimuth positions used during the calibration process. It is observed that the cosine response deviates from the ideal after 65^o of zenith angle when it suddenly rises due to the radiation falling on the edge of the detector.

APPENDIX F: COSINE RESPONSE OF THE DETECTOR

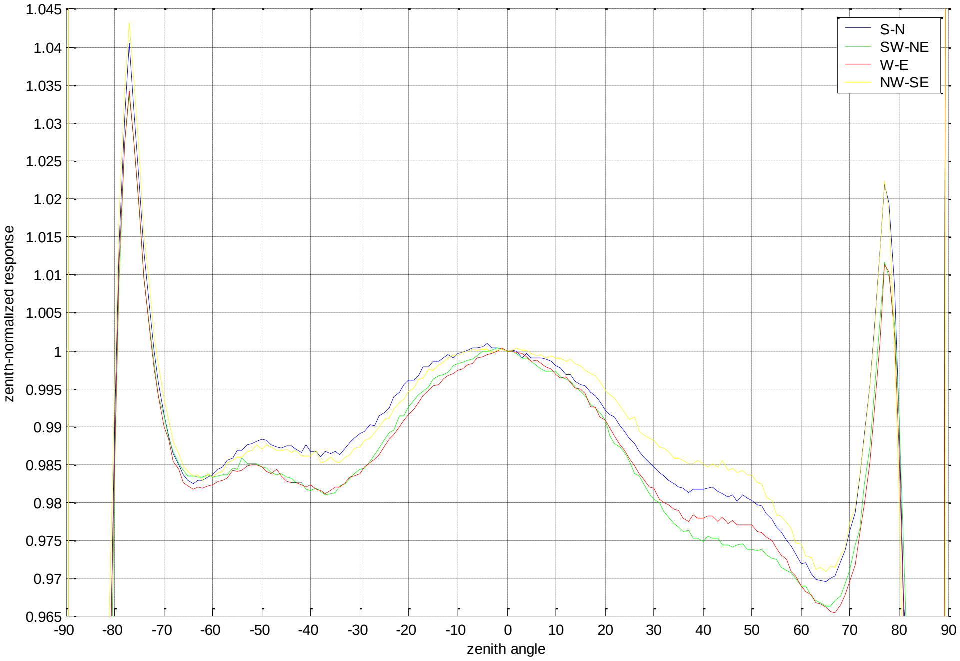

Figure F.1: Cosine Response (Armstrong, Schmelzer, Flynn, Hodges, & Michalsky, 2006)

The cosine responses of eight narrow band channels on UV-MFRSR and visual MFRSR instruments were measured and evaluated by (Grant & Gao, 2003). Figure F.2 shows the observed differences in cosine response for different wavelength detectors.

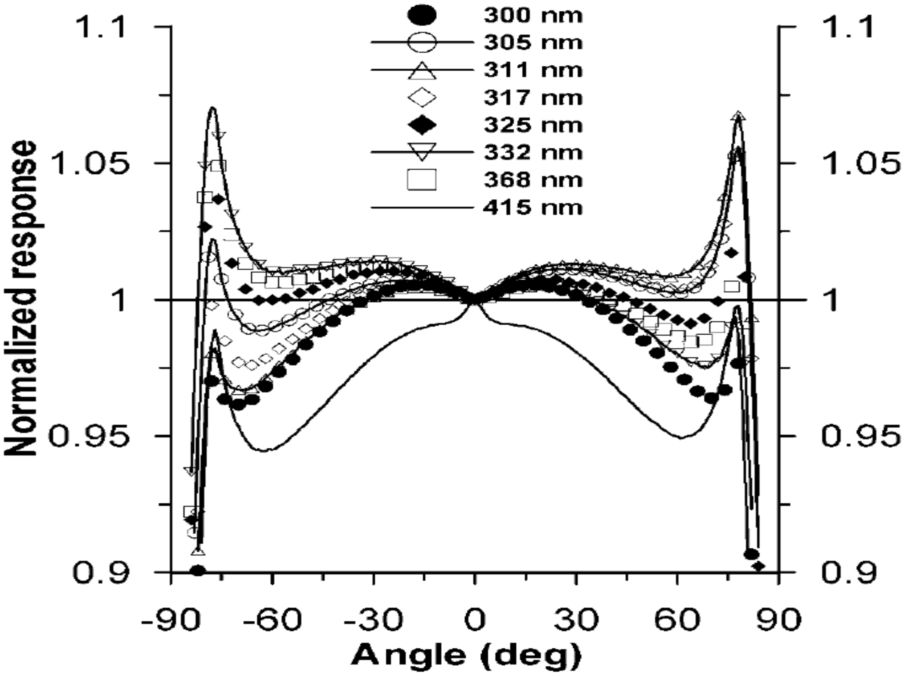

Figure F.2: Cosine response of different wavelength detectors (Grant & Gao, 2003)

Bibliography

Aeronet Aerosol Robotic Network. (2004). Retrieved March 2012, from NASA Space Flight Center: http://aeronet.gsfc.nasa.gov/cgi-bin/type_one_station_opera_v2_new?site=Mezaira&nachal=2&aero_water=0&level=1&if_day=0&year_or_month=0

Armstrong, P., Schmelzer, J., Flynn, C., Hodges, G., & Michalsky, J. (2006). MFRSR migration to CR1000 Logger and Other Improvements. *Internal Memo*. US: PNNL.

ASTM Standards. (2010). *Standard Test Method for Calibration of Pyrheliometers by Comparison to Reference Pyrheliometers*. Retrieved from ASTM International - Standards Worldwide Home: http://www.astm.org/Standards/E816.htm

Bendt, P., Rabl, A., Gaul, H., & Reed, K. A. (1979). *Optical Analysis and Optimization of Line Focus Solar Collectors.* Task No. 3432.30. Colorado: Solar Energy Research Institute.

Brooks, D. (2010). *Solar aureole photos and Asian dust*. Retrieved 12 12, 2011, from http://instesre.org: http://instesre.org/Solar/AureolePhotography/AsianDust_March2010.htm

Buie, D. C. (2004). *Optical considerations in solar concentrating systems.* PhD Thesis, University of Sydney, Sydney.

BIBLIOGRAPHY

Campbell Scientific. (2008). *CR1000 Measurement and Control System User's Manual.* Utah: Campbell Scientific,Inc . Retrieved from http://science.nature.nps.gov/im///units/sean/auxrep/WC/WC_cr1000_manual.pdf

Devore, J. G., Stair, A., Lepage, A., Rall, D., Atkinson, J., & Villanucci, D. (2009). Retrieving Properties of Thin Clouds from Solar Aureole Measurements. *Journal of Atmospheric and Oceanic Technology, 26*(12), 2531-2548.

Duffie, J. A., & Beckman, W. A. (2006, Third Edition). *Solar Engineering of Thermal Processes.* John Wiley & Sons.

Geyer, M. (2000). Euro Trough Progress and “NEXTrough” Opportunities for an Euro-American Trough Alliance. *Trough Meeting Workshop.* Madison.

Geyer, M., Lupfert, E., Osuna, R., Esteban, A., Schiel, W., Schweitzer, A., . . . Mandelberg, E. (2002). Euro Trough- Parabolic Trough Collector Developed for Cost Efficient Solar Power Generation. *11 th Int. Symposium on Concentrating Solar Power and Chemical Energy Technologies.* Zurich.

Grant, R. H., & Gao, W. (2003). Diffuse fraction of UV radiation under partly cloudy skies as defined by the Automated Surface Observation System (ASOS). *Journal of Geophysical Research, 108*(D2 4046). doi:10.1029/2002JD002201

Grether, D. F., Evans, D., Hunt, A., & Wahlig, M. (1979). *Measurements and Analysis of Circumsolar Radiation.* LBL10243. Lawrence Berkeley Laboratory.

Gueymard, C. A. (2001). Parameterized Transmittance Model for Direct Beam and Circumsolar Spectral Irradiance. *Solar Energy, 71*(5), 325-346. Retrieved from http://rredc.nrel.gov/solar/models/SMARTS/relatedrefs/SmartsAlgorithms_SE01.pdf

Hay, J., & Davies, J. (1980). Calculation of the Solar Radiation Incident on an Inclined Surface. *First Canadian Solar Radiation Data Workshop.* Toronto.

Hulstrom, R. (1989). *Solar Heat Technologies: Fundamentals and Applications.* MIT Press.

Jorge, H. G., Pillet, V. M., Vazquez, M., Palle, P., McGovern, F., & Raes, F. (1998). Measurements of the solar aureole at the Teide Observatory. *New Astronomy Reviews, 42*, 515-520.

Kalapatapu, R., Armstrong, P., & Chiesa, M. (2011). Rotating Shadowband for the measurement of Sunshapes. *Solar Paces.* Granada.

Kasten, F., & Young, A. (1989). Revised Optical Air Mass Tables and Approximation Formula. *Applied Optics, 28*, 4735.

Keidron, P., Schlemmer, J., & Klassen, M. (2006). *Rotating Shadowband Spectroradiometer (RSS) Handbook.* Atmospheric Radiation Measurement Climate Research Facility.

Kipp & Zonen. (2008). *CHP1-Passion for Precision*. Retrieved from Kipp & Zonen: http://www.kippzonen.com/?product/18172/CHP+1.aspx

LePage, A., Kras, S., & DeVore, J. (2008). *Description of SAM (Sun and Aureole Measurement) Sensor Data Collected in Support of CLASIC and CHAPS.* Burlington, MA: Visidyne, Inc.

Liu, B. Y., & Jordan, R. C. (1963). The Long- Term Average Performance of Flat- Plat Solar Energy Collectors. *Solar Energy, 7,* 53.

Major, G. (1992). Estimation of the Error Caused by the Circumsolar Radiation when Measuring Global Radiation as a sum of Dirrect and Diffuse Radiation. *Solar Energy, 48*(4), 249-252.

Michalsky, J. J., Augustine, J. A., & Kiedron, P. W. (2009). Improved broadband solar irradiance from the multi-filter rotating shadowband radiometer. *Solar Energy, 83*, 2144-2156.

Michalsky, J. J., Berndt, J. L., & Schuster, G. J. (1986). A Microprocessor- Based Rotating Shadowband Radiometer. *Solar Energy, 36*(5), 465-470.

Mims, F. M. (2003). Solar Aureoles Caused by Dust, Smoke and Haze. *Applied Optics, 42*(3), 492-496.

Neumann, A., & Witzke, A. (1999). The influence of sunshape on the DLR solar furnace beam. *Solar Energy, 66*(6), 447-457.

Neumann, A., von der Au, B., & Heller, P. (1998). Measurements of Circumsolar Radiation at the Plataforma Solar (Spain) and in Cologne (Germany). *Proc. of Int. Solar Energy Conf. Solar Engineering* (pp. 429-438). Albuquerque: ASME.

Neumann, A., Witzke, A., Scott, J. A., & Gregor, S. (2002). Representative Terrestrial Solar Brightness Profiles. *Journal of Solar Energy Engineering, 124*, 198-204.

Noring, J. E., Grether, D. F., & Hunt, A. J. (1991). *Circumsolar Radiation Data: The Lawrence Berkeley Laboratory reduced data base.* NREL Rep. TP-262-4429. National Renewable Energy Laboratory.

Perez, R., Seals, R., Ineichent, P., Stewart, R., & Menicucci, D. (1987). A New Simplified Version of the Perez Diffuse Irradiance Model for Tilted Surfaces. *Solar Energy, 39*(3), 221-231.

Ritter, J. M., & Kenneth, J. V. (1999). A New Instrument for Measurement of the Solar Aureole Radiance Distribution from Unstable Platforms. *Journal of Atmospheric and Oceanic Technology, 17*, 1040-1047.

Stine, W. B., & Harrigan, R. W. (1985). *Solar Energy Fundamentals and Design with computer Applications.* John Wiley & Sons.

Stoffel, T., Renne', D., Myers, D., Wilcox, S., Sengupta, M., George, R., & Turchi, C. (2010). *Concentrated Solar Power: Best Practices Handbook for the Collection and Use of Solar Resource Data.* NREL/TP-550-47465. Golden, Colorado: National Renewable Energy Laboratory.

Thomalla, E., Kopke, P., Muller, H., & Quenzel, H. (1982). Circumsolar Radiation Calculated for Various Atmospheric Conditions. *Solar Energy, 30*(6), 575-587.

Visidyne. (2011). *SAM-400 User's Manual_v03.* Burlington: Visidyne Inc.

Wilbert, S., Reinhardt, B., DeVore, J., Roger, M., Pitz-Paal, R., & Gueymard, C. (2011). Measurement of Solar Radiance Profiles With the Sun and Aureole Measurement System (SAM). *Solar Paces.* Granada.

Zerlaut, G. A., & Maybee, J. D. (1982). Spectroradiometer measurements in support of photovoltaic device testing. *Solar Cells, 7*, 97-106.